

AD-A279 126



WL-TM-94-3039

**Pressure Measurements on an
F/A-18 Twin Vertical Tail in
Buffeting Flow**

Volume 1 - Wind Tunnel Test Summary

Chris Pettit, Michael Banford, Dansen Brown, and Ed Pendleton

**Structural Dynamics Branch
Structures Division**

**August 1994
Final Report For Period April 1993 - August 1994**

94-14261



**DTIC
ELECTE
MAY 12 1994
S G D**

Approved For Public Release; Distribution is Unlimited

**Flight Dynamics Directorate
Wright Laboratory
Air Force Materiel Command
Wright Patterson Air Force Base, Ohio 45433-7562**

DTIC QUALITY ASSURED 1


94 5 11 015

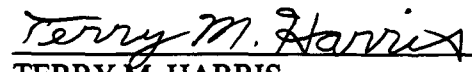
NOTICE


When Government drawings, specifications, or other data are used for any purpose other than in connection with a definitely Government-related procurement operation, the United States Government thereby incurs no responsibility nor any obligation whatsoever; and the fact that the government may have formulated, furnished, or in any way supplied the said drawings, specifications, or other data, is not to be regarded by implication or otherwise as in any manner licensing the holder or any other person or corporation, or conveying any rights or permission to manufacture use, or sell any patented invention that may be any way related thereto.

This report is releasable to the National Technical Information Service (NTIS). At NTIS, it will be available to the general public, including foreign nations.

This technical report has been reviewed and is approved for publication.


ED PENDLETON
Project Engineer
Aeroelasticity Section
Structural Dynamics Branch


TERRY M. HARRIS
Technical Manager
Aeroelasticity Section
Structural Dynamics Branch


JOSEPH W. MOSCHLER, Major, USAF
Chief, Structural Dynamics Branch
Structures Division

If your address has changed, if you wish to be removed from our mailing list, or if the addressee is no longer employed by your organization please notify WL/FIBG, 2210 Eighth St Ste 11, Wright-Patterson Air Force Base, OH 45433-7531 to help us maintain a current mailing list.

Copies of this report should not be returned unless return is required by security considerations, contractual obligations, or notice on a specific document.

REPORT DOCUMENTATION PAGE			Form Approved OMB No. 0704-0188	
Public reporting burden for this collection of information is estimated to average 1 hour per response, including the time for reviewing instructions, searching existing data sources, gathering and maintaining the data needed, and completing and reviewing the collection of information. Send comments regarding this burden estimate or any other aspect of this collection of information, including suggestions for reducing this burden, to Washington Headquarters Services, Directorate for Information Operations and Reports, 1215 Jefferson Davis Highway, Suite 1204, Arlington, VA 22202-4302, and to the Office of Management and Budget, Paperwork Reduction Project (0704-0188), Washington, DC 20503.				
1. AGENCY USE ONLY (Leave blank)	2. REPORT DATE August 31 1994	3. REPORT TYPE AND DATES COVERED Final Report April 1993 - August 1994		
4. TITLE AND SUBTITLE PRESSURE MEASUREMENTS ON AN F/A-18 TWIN VERTICAL TAIL IN BUFFETING FLOW VOL 1: WIND TUNNEL TEST SUMMARY		5. FUNDING NUMBERS PE: 62201F PR: 2401 TA: 04 WU: 46		
6. AUTHOR(S) Pettit, C., Banford, M., Brown, D., and Pendleton, E.				
7. PERFORMING ORGANIZATION NAME(S) AND ADDRESS(ES) Structural Dynamics Branch Structures Division Flight Dynamics Directorate Wright Laboratory Wright Patterson AFB, Ohio 45433-7552		8. PERFORMING ORGANIZATION REPORT NUMBER WL-TM-94-3039 Vol 1		
9. SPONSORING / MONITORING AGENCY NAME(S) AND ADDRESS(ES) Flight Dynamics Directorate Wright Laboratory Air Force Materiel Command Wright Patterson Air Force Base, OH 45433-7562		10. SPONSORING / MONITORING AGENCY REPORT NUMBER WL-TM-94-3039 Vol 1		
11. SUPPLEMENTARY NOTES				
12a. DISTRIBUTION / AVAILABILITY STATEMENT APPROVED FOR PUBLIC RELEASE; DISTRIBUTION IS UNLIMITED.		12b. DISTRIBUTION CODE		
13. ABSTRACT (Maximum 200 words) Buffeting pressure measurements were made on the vertical tail surface of a full scale F/A-18 aircraft model in the National Full Scale Aerodynamics Complex at NASA Ames Research Center. Test variables included aircraft angle-of-attack, aircraft sideslip angle, and dynamic pressure. Accelerometers were used to obtain vertical tail accelerations. Pressure transducers were mounted on the starboard vertical tail. Steady and unsteady pressures were obtained. Unsteady pressure data were reduced to PSD and CSD forms. Both steady and unsteady RMS pressure coefficients are also presented. Volume I contains the general description of the model, the test program, and highlights of the reduced data. Volume II contains steady and unsteady RMS data. Volume III contains unsteady PSD results. Volume IV contains unsteady CSD results.				
14. SUBJECT TERMS unsteady aerodynamics pressure measurements experimental data		buffeting flow wind tunnel tests pressure transducers		15. NUMBER OF PAGES 104
				16. PRICE CODE
17. SECURITY CLASSIFICATION OF REPORT Unclassified	18. SECURITY CLASSIFICATION OF THIS PAGE Unclassified	19. SECURITY CLASSIFICATION OF ABSTRACT Unclassified	20. LIMITATION OF ABSTRACT UL	

Foreword

This report was prepared by the Structural Dynamics Branch, Structures Division, Flight Dynamics Directorate, Wright Laboratory, Wright Patterson Air Force Base, Ohio. The wind tunnel test program described in this report was conducted during a joint NASA, Navy, and Air Force F/A-18 test program conducted at the NASA Ames Research Center. The wind tunnel data taken by Wright Laboratory engineers during the F/A-18 wind tunnel test was acquired in support of Project 2401, "Structural Mechanics", Task 240104, "Vibration Prediction and Control, Measurement, and Analysis" and Work Unit 24010446, F-18 Twin Vertical Tail Buffet. The project engineers for this effort were Mr. Ed Pendleton and Mr. Chris Pettit. Mr. Dansen Brown, a mathematician, provided engineering analysis support for reduction of the test data. Mr. Mike Banford was the lead technician responsible for instrumentation and data collection.

The authors wish to thank the NASA Ames F/A-18 Wind Tunnel Test Team for their cooperation during testing of the F/A-18, especially Mr. Gavin Botha, Ms. Wendy Lanser, Mr. Kevin James, Mr. Roger Stewart, and Mr. Roy Arakaki. The authors also wish to thank Dr. Holt Ashley of RANN Corporation, Dr. Marty Ferman formerly of McDonnell Douglas Corporation, and Dr. James Olsen for their technical advice and suggestions during the preparation of this report. The authors further thank Mr. Larry Dukate for his assistance in reducing test data, and Mr. Scott Harris and Mr. Dick Talmadge for their technical assistance during the instrumentation phase of the test program.

This manuscript was released in August 1994 for publication as a Technical Memorandum. This report covers technical work conducted from March 1993 through August 1994.

Accession For	
NTIS	CRA&I
DTIC	TAB
Unannounced	<input type="checkbox"/>
Justification _____	
By _____	
Distribution /	
Availability Codes	
Dist	Avail and/or Special
A-1	

Table of Contents

<u>Section</u>		<u>Page</u>
I	Introduction	1
II	Model Test Configuration	4
III	Test Program	21
IV	Data Reduction Techniques	24
V	Results and Discussion	26
VI	Conclusions	59
VII	References	60
	Appendix I	61
	Appendix II	96

List of Illustrations

Figure		Page
1	F/A-18 Aircraft Model in NFAC 80 by 120 ft. Wind Tunnel	2
2	F/A-18 Three View Layout	5
3	F/A-18 Component Details	6
4	F/A-18 Layout with Performance and Specifications	7
5	Schematic of National Full Scale Aerodynamic Complex	8
6	Minimum and maximum angle of attack for aircraft on struts	8
7	F/A-18 mounted on struts in 80 by 120 Wind Tunnel	10
8	F/A-18 in the Tunnel during Starboard Fin Instrumentation	10
9	Mode Shapes for Vertical Tail 1st Bending at 28.8 Angle of Attack	12
10	Mode Shapes for Vertical Tail 1st Torsion at 28.8 Angle of Attack	12
11	Mode Shapes for Vertical Tail 2nd Bending at 28.8 Angle of Attack	12
12	F/A-18 Outboard Starboard Tail with Pressure Transducer Installed	14
13	Inboard Tail instrumented with Transducers	15
14	Six by six Grid specified by early test plan	16
15	Actual 6 by 6 Grid Pressure Transducer Locations	16
16	Schematic of Data Acquisition System	18
17	Multiplexer installed in F/A-18 Avionics Bay	19
18	Data Acquisition Equipment in Control Room	19
19	Steady Pressure Differential acting on Starboard Tail, $\alpha = 32$ degrees	27
20	Steady Pressure Differential acting on Vertical Tail - Contour Plot, $\alpha = 32$ degrees	28
21	Fin Area Elements and corresponding Transducer Locations	31
22	Steady Normal Force and Root Bending Moment Coefficient versus Angle-of-Attack at Zero Sideslip	32
23	Steady Normal Force and Root Bending Moment Coefficients versus Sideslip	32
24A	RMS Pressure Differential Surface Plot for angle of attack of 32 degrees, Fence Off	35
24B	RMS Pressure Differential Surface Plot for angle of attack of 32 degrees, Fence On	36

25A	RMS Pressure Differential Contour Plot for angle of attack of 32 degrees, Fence Off	37
25B	RMS Pressure Differential Contour Plot for angle of attack of 32 degrees, Fence On	38
26A	Unsteady Pressure Differential Power Spectral Density for angle of attack of 32 degrees, Station 16-57	41
26B	Nondimensional Unsteady Pressure Differential Power Spectral Density for angle of attack of 32 degrees, Station 16-57	41
27A	Unsteady Pressure Differential Power Spectral Density for angle of attack of 32 degrees, Station 18-55	41
27B	Nondimensional Unsteady Pressure Differential Power Spectral Density for angle of attack of 32 degrees, Station 18-55	41
28A	Unsteady Pressure Differential Power Spectral Density for angle of attack of 20 degrees, Station 16-57	42
28B	Nondimensional Unsteady Pressure Differential Power Spectral Density for angle of attack of 20 degrees, Station 16-57	42
29A	Unsteady Pressure Differential Power Spectral Density for angle of attack of 20 degrees, Station 18-55	42
29B	Nondimensional Unsteady Pressure Differential Power Spectral Density for angle of attack of 20 degrees, Station 18-55	42
30A	RMS Normal Force and Bending Moment Coefficients versus Angle-of-Attack at Zero Sideslip	46
31	RMS Normal Force and Bending Moment Coefficients versus Sideslip	46
32	RMS Root Bending Moment Power Spectral Density, AoA= 20 degrees	48
33	RMS Root Bending Moment Power Spectral Density, AoA= 32 degrees	48
34	RMS Root Bending Moment Power Spectral Density, AoA= 40 degrees	48
35A	RMS Acceleration for Starboard Fin Accelerometer #1 as a function of angle of attack, zero sideslip	50
35B	RMS Acceleration for Starboard Fin Accelerometer #2 as a function of angle of attack, zero sideslip	50
35C	RMS Acceleration for Port Fin Accelerometer #1 as a function of angle of attack, zero sideslip	50
35D	RMS Acceleration for Port Fin Accelerometer #2 as a function of angle of attack, zero sideslip	50
36A	RMS Acceleration for Starboard Fin Accelerometer #1 as a function of sideslip angle, angle of attack 30 degrees	51
36B	RMS Acceleration for Starboard Fin Accelerometer #2 as a function of sideslip angle, angle of attack 30 degrees	51

36C	RMS Acceleration for Port Fin Accelerometer #1 as a function of sideslip angle, angle of attack 30 degrees	51
36D	RMS Acceleration for Port Fin Accelerometer #2 as a function of sideslip angle, angle of attack 30 degrees	51
37A	RMS Acceleration for Starboard Fin Accelerometer #1 as a function of sideslip angle, angle of attack 35 degrees	52
37B	RMS Acceleration for Starboard Fin Accelerometer #2 as a function of sideslip angle, angle of attack 35 degrees	52
37C	RMS Acceleration for Port Fin Accelerometer #1 as a function of sideslip angle, angle of attack 35 degrees	52
37D	RMS Acceleration for Port Fin Accelerometer #2 as a function of sideslip angle, angle of attack 35 degrees	52
38A	Acceleration Power Spectral Density for Starboard Fin Accelerometer #S2	55
38B	Acceleration Power Spectral Density for Starboard Fin Accelerometer #S1	55
38C	Acceleration Power Spectral Density for Port Fin Accelerometer #S2	55
38D	Acceleration Power Spectral Density for Port Fin Accelerometer #S1	55
39A	Acceleration Power Spectral Density for Starboard Fin Accelerometer #S2, angle of attack 20 degrees	56
39B	Acceleration Power Spectral Density for Starboard Fin Accelerometer #S1, angle of attack 20 degrees	56
39C	Acceleration Power Spectral Density for Port Fin Accelerometer #S2, angle of attack 20 degrees	56
39D	Acceleration Power Spectral Density for Port Fin Accelerometer #S1, angle of attack 20 degrees	56

List of Tables

Table		Page
1	Natural Frequencies of the F/A-18 Vertical Fins	11
2	F/A-18 Full-Scale Wind Tunnel Test Conditions	22
3	Kulite Microphone Sensitivities	25
4	Total Damping Ratio Estimates for Twin Vertical Fins	57

Section I

Introduction

Contemporary twin-tail fighter aircraft may encounter high frequency empennage vibrations caused by flow emanating from the forebody or wings during high angle-of-attack maneuvering. This turbulent flow occurs when the air flow on the forebody or upper wing surfaces becomes detached at high angles of attack. Air flow in the detached region becomes turbulent, giving rise to fluctuating pressures on the wing and downstream surfaces.

The induced unsteady pressures, commonly referred to as buffet, are broad-band random fluctuations having predominant frequencies associated with the primary aerodynamic characteristics of the aircraft. These primary airflow properties may include, but are not limited to, vortex flow from engine inlets, sharp corners, and highly swept lifting surfaces. Twin-tail fighter aircraft have proven to be especially susceptible to buffet at high angles-of-attack. The turbulent air flow excites the tail surfaces embedded in the flow and large oscillatory structural responses result at the resonant frequencies of the tail. After prolonged exposure to this flow environment, the tail structure can begin to fatigue and repairs must be initiated. The maintenance costs and aircraft down time associated with these repairs are often quite high. To reduce these costs, the tail structure and associated equipment must be designed to both minimize and tolerate these oscillatory responses.

One twin-tail fighter aircraft that often encounters tail buffet when conducting air combat maneuvers at high angles-of-attack is the F/A-18. In an effort to quantify the F/A-18 tail buffet loads and to provide data for use in the development of potential solutions to counter the twin tail buffet problem, wind tunnel tests were conducted to measure the aerodynamic pressures on the twin tails of an F/A-18. The F/A-18 aircraft, shown in Figure 1, was tested in the National Full Scale Aerodynamic Complex (NFAC) 80 by 120 Foot Wind Tunnel located at NASA Ames Research Center in Mountain View, California. Buffet pressures and the resulting structural vibrations of the vertical fins were obtained over a range of angle of attack and sideslip conditions.

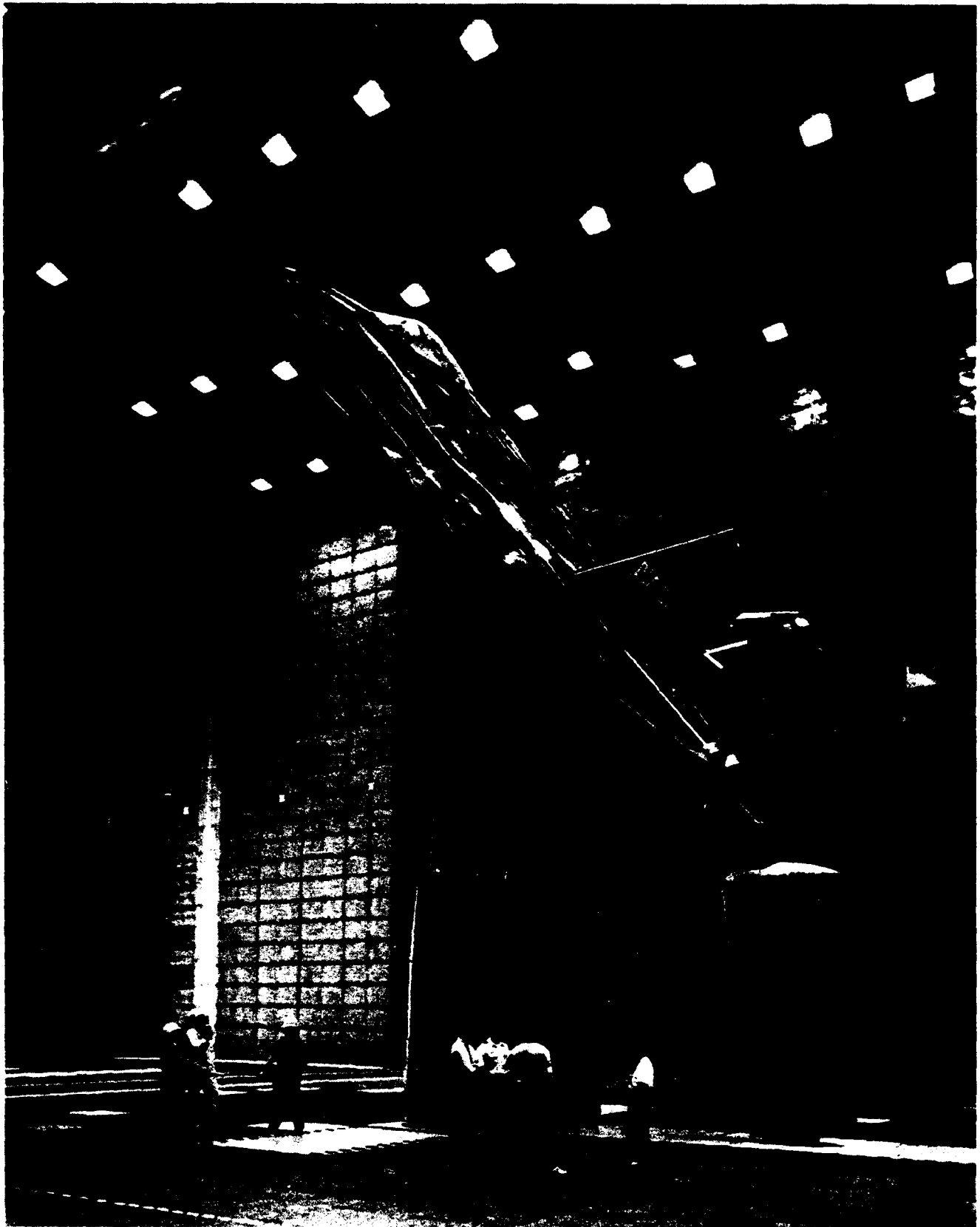


Figure 1. F/A-18 Aircraft Model in NFAC 80 by 120 ft. Wind Tunnel

Engineers and technicians from NASA Ames Research Center and Wright Laboratory instrumented the F/A-18 vertical tails with pressures transducers and accelerometers to measure the oscillatory pressures and tail responses due to the turbulent airflow. NASA engineers used 96 pressure transducers in an 8-by-6 grid on both sides of the left, or port, vertical tail. Wright Lab engineers instrumented the right, or starboard, vertical fin with 72 pressure transducers in a 6-by-6 grid. Aerodynamic pressures on each tail were recorded using separate data acquisition systems. Accelerometers were also located near the leading and trailing edges of each fin at the tips to measure the dynamic structural response created by the buffet.

This technical report presents the measured aerodynamic pressures and tip accelerations obtained from the F/A-18 starboard vertical tail during wind tunnel testing. Also included are the corresponding fin-tip accelerations from the port vertical tail. Results from both steady and unsteady pressure measurements, obtained over a range of buffet flow conditions, are presented. The steady pressures are presented in plots and integrated to give aerodynamic coefficients. The unsteady pressures were reduced to root-mean-square (RMS), power spectral density (PSD), and cross spectral density (CSD) forms.

Section II

Model Test Configuration

The full scale F/A-18 aircraft model was installed in the 80-by-120 Ft. Wind Tunnel which is part of the National Full-Scale Aerodynamic Complex (NFAC) at NASA Ames Research Center (Ref. 1). The aircraft, supplied by the U.S. Navy, was from the initial F/A-18 model A production block. The overall layout of the F/A-18, including some dimensions, is depicted in Figures 2, 3 and 4. The F/A-18 aircraft has a 56.0 ft overall length, a 37.42 ft wing span, a 400 ft² reference wing area, and an 11.52 ft wing mean aerodynamic chord. The engines, avionics, and main landing gear were removed for the wind tunnel test. The aircraft was configured with flow-through inlets and the missile rails were left in place on the wing tips.

The NFAC may be configured as either a closed circuit wind tunnel with a 40 by 80 foot test section or an open wind tunnel with an 80 by 120 foot test section. A tunnel schematic is shown in Figure 5. When operated as an open circuit, the NFAC generates a maximum freestream dynamic pressure of 33 psf with a maximum velocity of 100 knots. The corresponding maximum Reynolds number is 1.1×10^6 per foot under standard atmospheric conditions. The wind tunnel is driven by six 40 foot diameter, variable speed, variable pitch fans. Each fan is powered by a 22500 hp electric motor. At full speed, the wind tunnel draws 106 MW of power.

Figure 6 shows a schematic of the aircraft in the test section at minimum and maximum angles of attack. The aircraft was mounted slightly below the test section centerline to reduce wall effects between the tunnel ceiling and forebody at high angles of attack. Tunnel flow area blockage was less than 4.9% at 20 degrees and increased to less than 7.5% at an angle of attack of 50 degrees.

During the test, the control deflections were set to the standard control-law scheduled values for angles-of-attack greater than 26 degrees. The leading-edge flaps were fixed at an angle of 34 degrees down and the trailing-edge flaps were undeflected. The aircraft hydraulic systems, except for those supporting the horizontal stabilators, were nonfunctional. The horizontal stabilators were actuated to match the trimmed orientation of those on the High

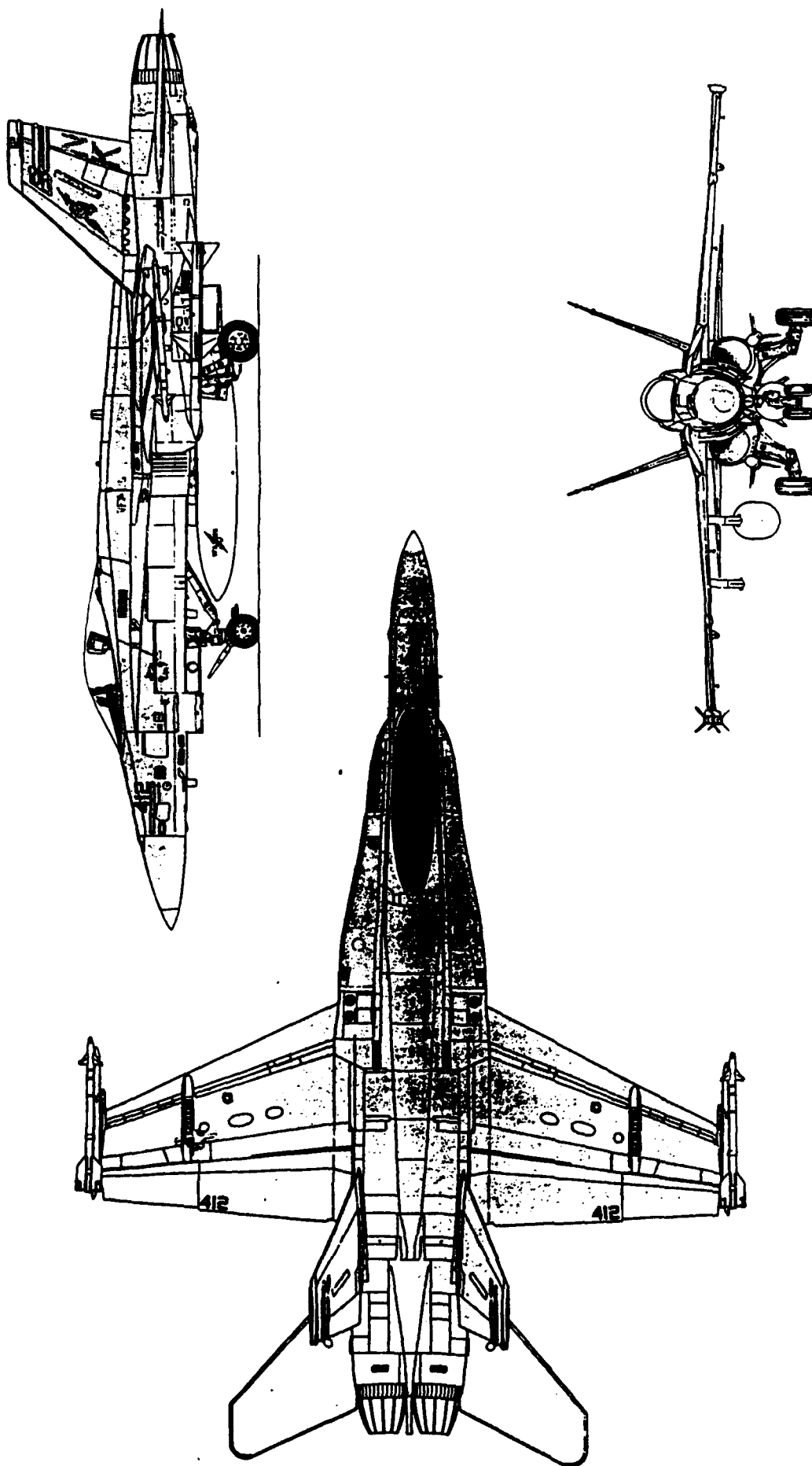
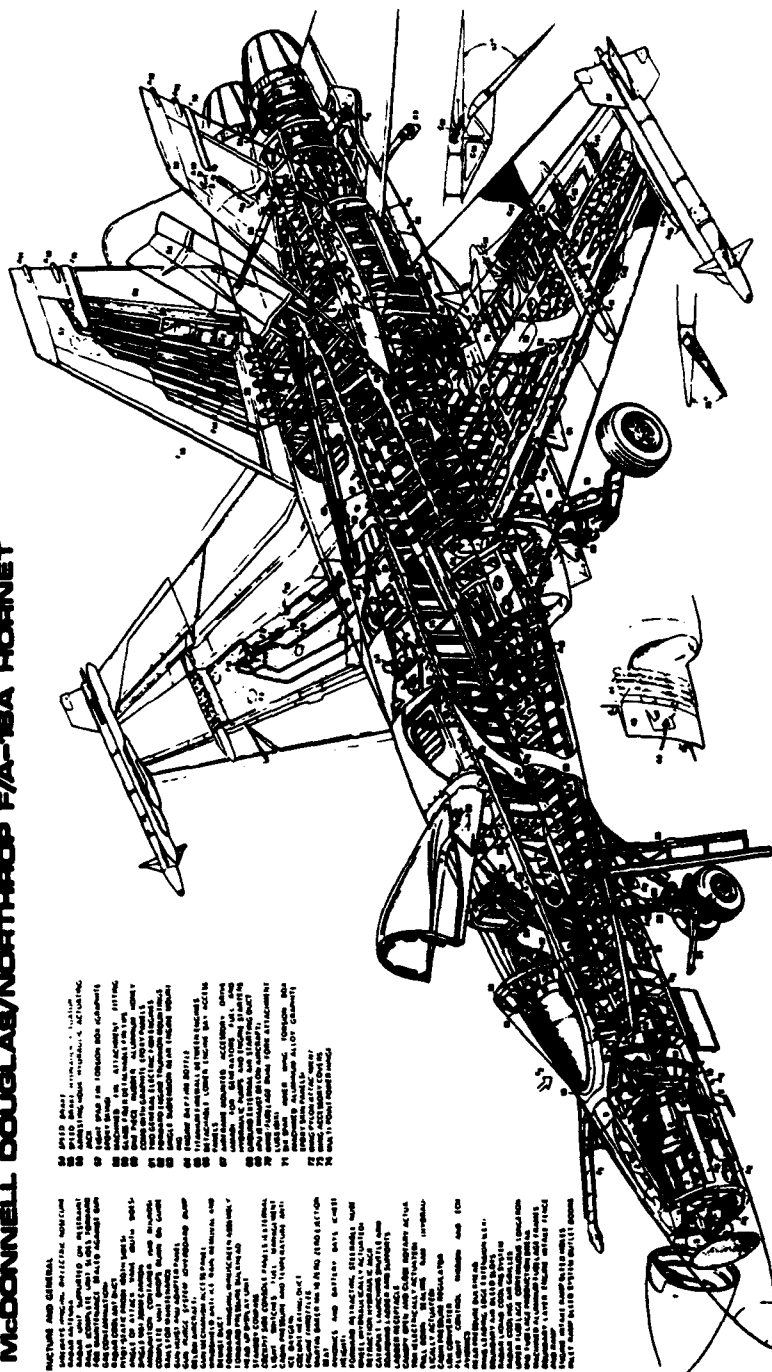


Figure 2. F/A-18 Three View Layout

McDONNELL DOUGLAS/NORTHROP F/A-18A HORNET



- 1. Structure and General
- 2. Fuselage
- 3. Wing
- 4. Tail
- 5. Landing Gear
- 6. Engine
- 7. Fuel System
- 8. Hydraulic System
- 9. Electrical System
- 10. Environmental Control System
- 11. Air Conditioning System
- 12. Heating System
- 13. Cooling System
- 14. Exhaust System
- 15. Noise Reduction System
- 16. Radar System
- 17. Infrared Search System
- 18. Targeting System
- 19. Weapons System
- 20. Avionics System
- 21. Cockpit System
- 22. Ejection Seat System
- 23. Parachute System
- 24. Survival Equipment
- 25. Identification Friend or Foe System
- 26. Countermeasures System
- 27. Communications System
- 28. Data Link System
- 29. Link System
- 30. Control System
- 31. Display System
- 32. Input System
- 33. Output System
- 34. Processing System
- 35. Storage System
- 36. Retrieval System
- 37. Distribution System
- 38. Conversion System
- 39. Control System
- 40. Display System
- 41. Input System
- 42. Output System
- 43. Processing System
- 44. Storage System
- 45. Retrieval System
- 46. Distribution System
- 47. Conversion System
- 48. Control System
- 49. Display System
- 50. Input System
- 51. Output System
- 52. Processing System
- 53. Storage System
- 54. Retrieval System
- 55. Distribution System
- 56. Conversion System
- 57. Control System
- 58. Display System
- 59. Input System
- 60. Output System
- 61. Processing System
- 62. Storage System
- 63. Retrieval System
- 64. Distribution System
- 65. Conversion System
- 66. Control System
- 67. Display System
- 68. Input System
- 69. Output System
- 70. Processing System
- 71. Storage System
- 72. Retrieval System
- 73. Distribution System
- 74. Conversion System
- 75. Control System
- 76. Display System
- 77. Input System
- 78. Output System
- 79. Processing System
- 80. Storage System
- 81. Retrieval System
- 82. Distribution System
- 83. Conversion System
- 84. Control System
- 85. Display System
- 86. Input System
- 87. Output System
- 88. Processing System
- 89. Storage System
- 90. Retrieval System
- 91. Distribution System
- 92. Conversion System
- 93. Control System
- 94. Display System
- 95. Input System
- 96. Output System
- 97. Processing System
- 98. Storage System
- 99. Retrieval System
- 100. Distribution System

- 101. Structure and General
- 102. Fuselage
- 103. Wing
- 104. Tail
- 105. Landing Gear
- 106. Engine
- 107. Fuel System
- 108. Hydraulic System
- 109. Electrical System
- 110. Environmental Control System
- 111. Air Conditioning System
- 112. Heating System
- 113. Cooling System
- 114. Exhaust System
- 115. Noise Reduction System
- 116. Radar System
- 117. Infrared Search System
- 118. Targeting System
- 119. Weapons System
- 120. Avionics System
- 121. Cockpit System
- 122. Ejection Seat System
- 123. Parachute System
- 124. Survival Equipment
- 125. Identification Friend or Foe System
- 126. Countermeasures System
- 127. Communications System
- 128. Data Link System
- 129. Link System
- 130. Control System
- 131. Display System
- 132. Input System
- 133. Output System
- 134. Processing System
- 135. Storage System
- 136. Retrieval System
- 137. Distribution System
- 138. Conversion System
- 139. Control System
- 140. Display System
- 141. Input System
- 142. Output System
- 143. Processing System
- 144. Storage System
- 145. Retrieval System
- 146. Distribution System
- 147. Conversion System
- 148. Control System
- 149. Display System
- 150. Input System
- 151. Output System
- 152. Processing System
- 153. Storage System
- 154. Retrieval System
- 155. Distribution System
- 156. Conversion System
- 157. Control System
- 158. Display System
- 159. Input System
- 160. Output System
- 161. Processing System
- 162. Storage System
- 163. Retrieval System
- 164. Distribution System
- 165. Conversion System
- 166. Control System
- 167. Display System
- 168. Input System
- 169. Output System
- 170. Processing System
- 171. Storage System
- 172. Retrieval System
- 173. Distribution System
- 174. Conversion System
- 175. Control System
- 176. Display System
- 177. Input System
- 178. Output System
- 179. Processing System
- 180. Storage System
- 181. Retrieval System
- 182. Distribution System
- 183. Conversion System
- 184. Control System
- 185. Display System
- 186. Input System
- 187. Output System
- 188. Processing System
- 189. Storage System
- 190. Retrieval System
- 191. Distribution System
- 192. Conversion System
- 193. Control System
- 194. Display System
- 195. Input System
- 196. Output System
- 197. Processing System
- 198. Storage System
- 199. Retrieval System
- 200. Distribution System

Figure 3. F/A-18 Component Details

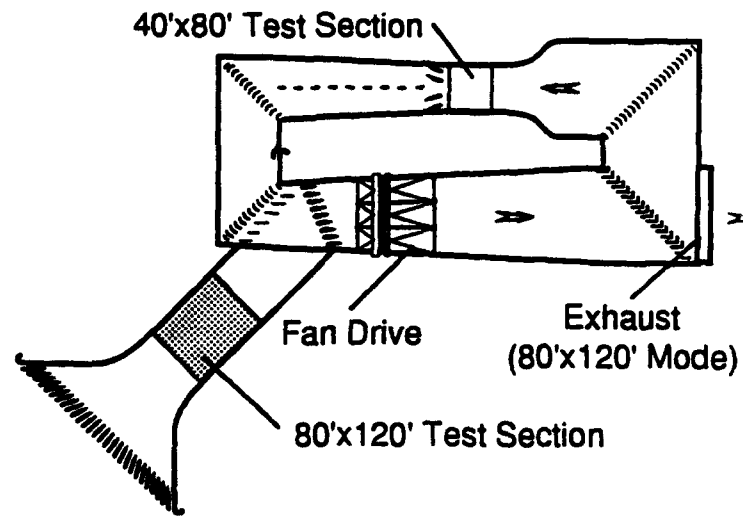


Figure 5. Schematic of National Full Scale Aerodynamic Complex

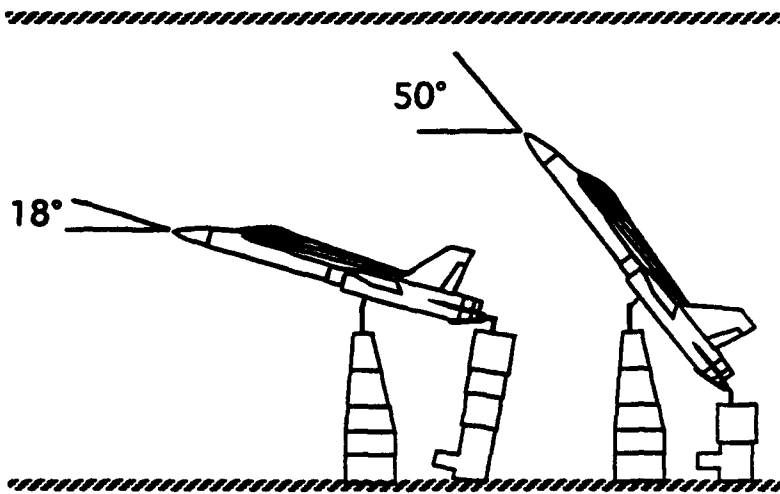


Figure 6. Minimum and maximum angles of attack for aircraft on struts

Angle-of-Attack Research Vehicle (HARV) for trimmed flight in steady, 1 "g" flight conditions at each angle-of-attack. The rudders were fixed in their undeflected position throughout the test using a special link constructed to replace the rudder actuator.

The original set of leading-edge-extension (LEX) fences, installed on all U.S. Navy F/A-18 aircraft to reduce tail buffet loads, was removed in favor of a pressure-instrumented pair which had previously flown on the HARV. The LEX fences installed for these tests were trapezoidal in shape with a 36.6 inch long base, a 27.9 inch long top, and were 8.375 inches in width. The aircraft model was also equipped with special forebody strakes that were installed for evaluation during wind tunnel testing. These strakes remained undeployed during the fin buffet testing portion of the wind tunnel test.

The F/A-18 test article was supported in the wind tunnel test section by three struts as shown in Figures 7 and 8. Two fixed height, main struts were located under the main landing gear. These struts were connected to a horizontal cross-bar that was attached to the aircraft by two blade and clevis assemblies, which replaced the main landing gear trunnions. The third strut, a large linear actuator that raised or lowered the tail linearly to control the angle of attack, was connected to the aircraft by a three beam cantilever structure attached to the engine mounts and the tailhook pivot point. The strut attachment point was located aft of the engine exhaust nozzles to maintain a positive mechanical advantage at higher angles-of-attack.

The three struts were mounted on a turntable in the floor of the wind tunnel. The turntable could be rotated to place the test article at various sideslip orientations. Each of the struts was covered by an aerodynamic fairing. As the turntable rotated to yaw the aircraft, the fairings would counter-rotate to stay aligned with the wind tunnel axis. The tail strut fairing was telescopic, and could be adjusted in length and tilt angle to cover the tail strut as the aircraft was pitched.

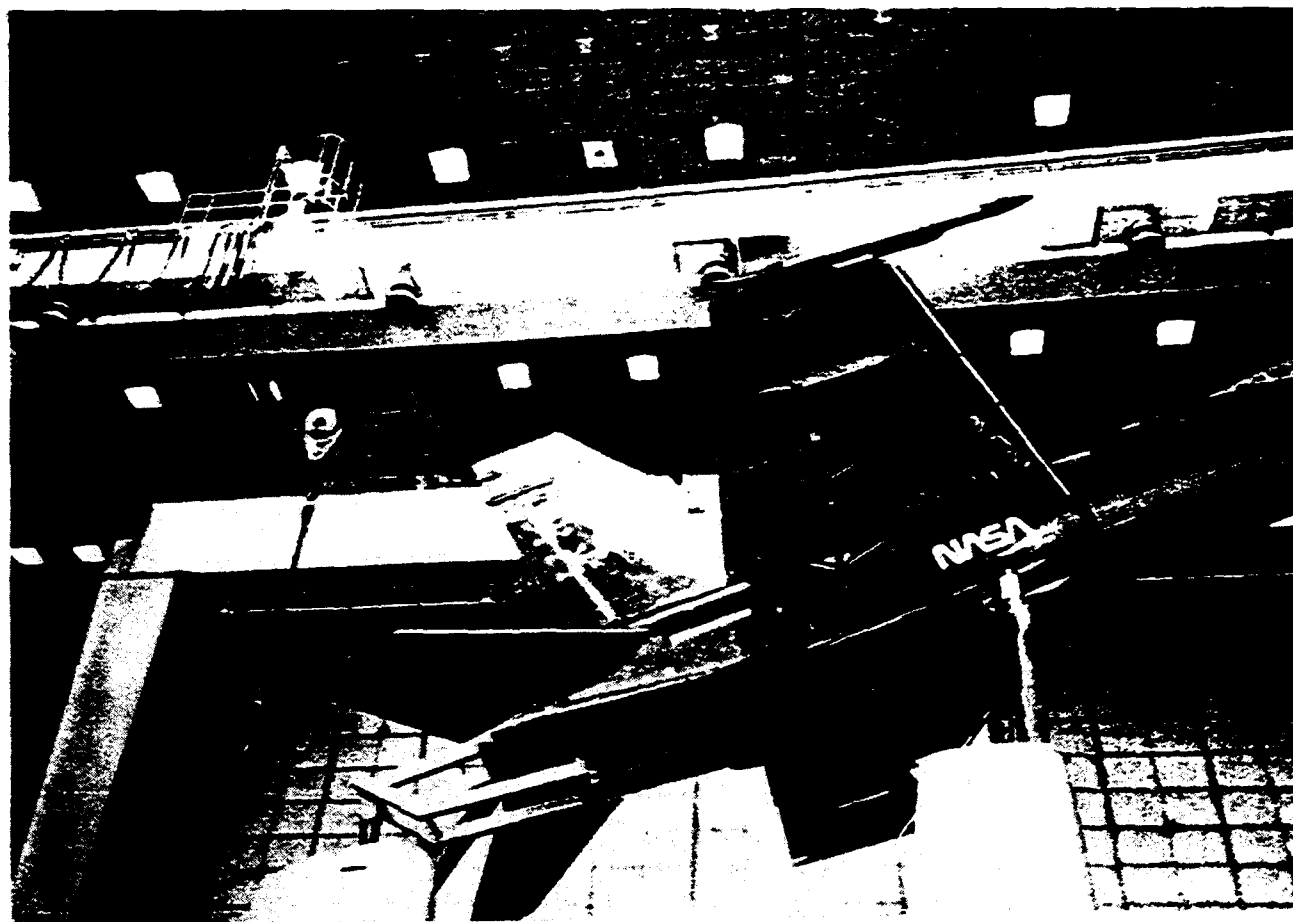


Figure 7. F/A-18 mounted on struts in 80 by 120 Tunnel



Figure 8. F/A-18 in the Tunnel during Starboard Fin instrumentation

Modal Characteristics

Modal characteristics for the full scale F/A-18 wind tunnel model were defined during a modal survey conducted while the aircraft was mounted in the wind tunnel. These ground vibration tests (Ref. 2) were conducted on the vertical fins to determine how the structure's natural modes and frequencies were affected with the aircraft mounted on the wind tunnel struts and with the engines removed. Table 1 gives the natural frequencies for the first three modes. These values were considered to be consistent with values for the fully configured production aircraft. Figures 9, 10, and 11 depict the symmetric and antisymmetric modes shapes associated with the first three modes.

The aircraft was vibration tested at three angles of attack, 16.0, 28.8, and 45.5 degrees. Over this range, the fundamental symmetric and antisymmetric bending mode frequencies each varied less than 0.4 Hz, the first symmetric and antisymmetric torsion mode frequencies each varied less than 1.7 Hz, and the second symmetric and antisymmetric bending mode frequencies each varied less than 1.7 Hz. In addition to natural frequencies, mode shapes, and modal masses and damping ratios also were obtained during the ground vibration tests (GVT) for each of the listed modes. These data are presented in Reference 2.

Table 1. Natural Frequencies of F/A-18 Vertical Fins

Twin Vertical Tail Structural Mode	Natural Frequency (Hz)
1st Bending	Symmetric - 15.4 Antisymmetric - 15.3
1st Torsion	Symmetric - 44.2 Antisymmetric - 45.4
2nd Bending	Symmetric - 61.3 Antisymmetric - 61.9

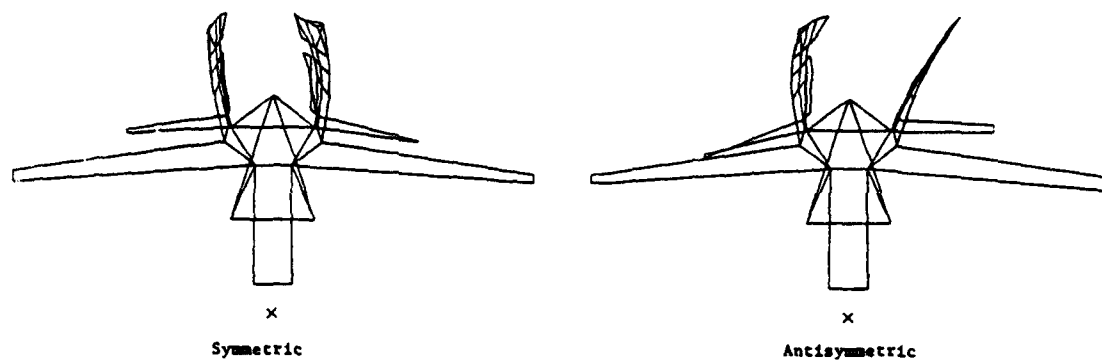


Figure 9. Mode Shapes for Vertical Tail 1st Bending at 28.8 Angle of Attack

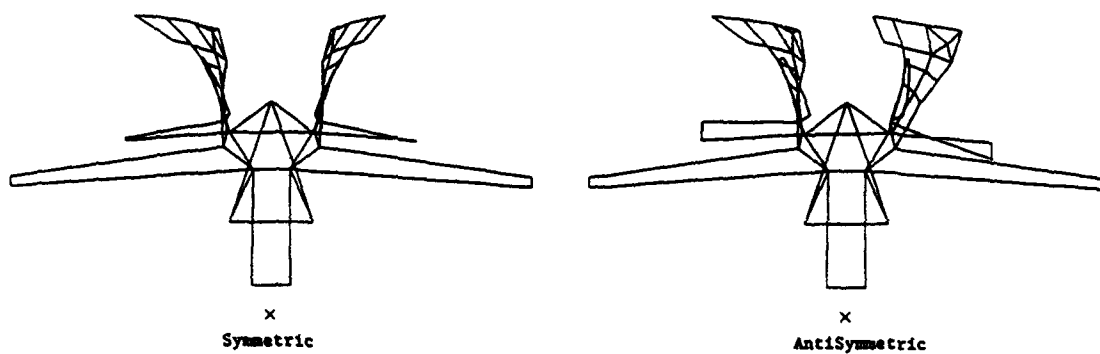


Figure 10 Mode Shapes for Vertical Tail 1st Torsion at 28.8 Angle of Attack

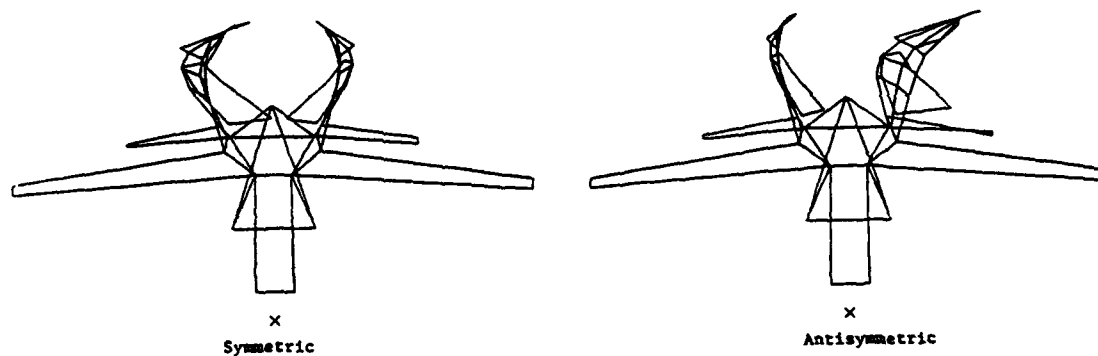


Figure 11. Mode Shapes for Vertical Tail 2nd Bending at 28.8 Angle of Attack

Instrumentation

Seventy-two (72) Kulite, flat pack style, strain gage-based pressure microphones (model # LQ-167-125-10SG) were installed in a 6 by 6 grid on either side of the starboard vertical tail of the F/A-18 prior to installation of the aircraft model in the tunnel. Manufacturer specifications show the output from these microphones to possess a typical hysteresis of 0.1% and repeatability of 0.25%. Figures 12 and 13 show the transducers mounted on the outboard and inboard sides of the fin, respectively. The transducers, each .05 inch thick, were fixed to the tail surfaces using a silicone-based, electrical grade RTV compound. Plastic, circular fairings, .035 inch thick with a four inch diameter, were cemented to the skin surface around each pressure transducer. These fairings were used in order to eliminate any local flow disturbances that might have been generated by the transducers themselves. The circular fairings are easily visible in Figures 12 and 13.

The thin wires from each transducer were secured flush to the tail skin surface. The wires were glued to the fin surface using a rubber-based, general adhesive and then, for further protection, taped with Scotch 375 clear tape. The wires were routed to access areas along the rudder hinge line to minimize the amount of exposed wire. High speed tape was used initially to secure the thin, unshielded wires, but had to be removed when the transducer signals exhibited unacceptable levels of noise while the aircraft was located in the model preparation area. On several occasions, some strips of the Scotch tape began to loosen during wind tunnel testing and had to be periodically replaced.

Figure 14 depicts a 6 by 6 set of spanwise and chordwise target transducer locations, as initially specified in the test plan. This test plan was inherited by the wind tunnel test team. This early figure shows the rudder hinge line located at the root at approximately 75%-chord, whereas the actual hinge line, shown in Figure 15, lies along the 80%-chord line. During installation of the pressure transducers on the aircraft, the chordwise and spanwise locations of the transducers were maintained the same as the targets in the grid layout in Figure 14. However, since the rudder hinge line falls along the 80% line, four of the transducer stations specified along the 80% chord line had to be shifted forward slightly so that the eight (8) corresponding transducers could be fixed to actual skin surface. The 6-by-6 grid of transducers was mounted on the outboard and inboard sides of the vertical tail as illustrated in Figure 15. The transducer

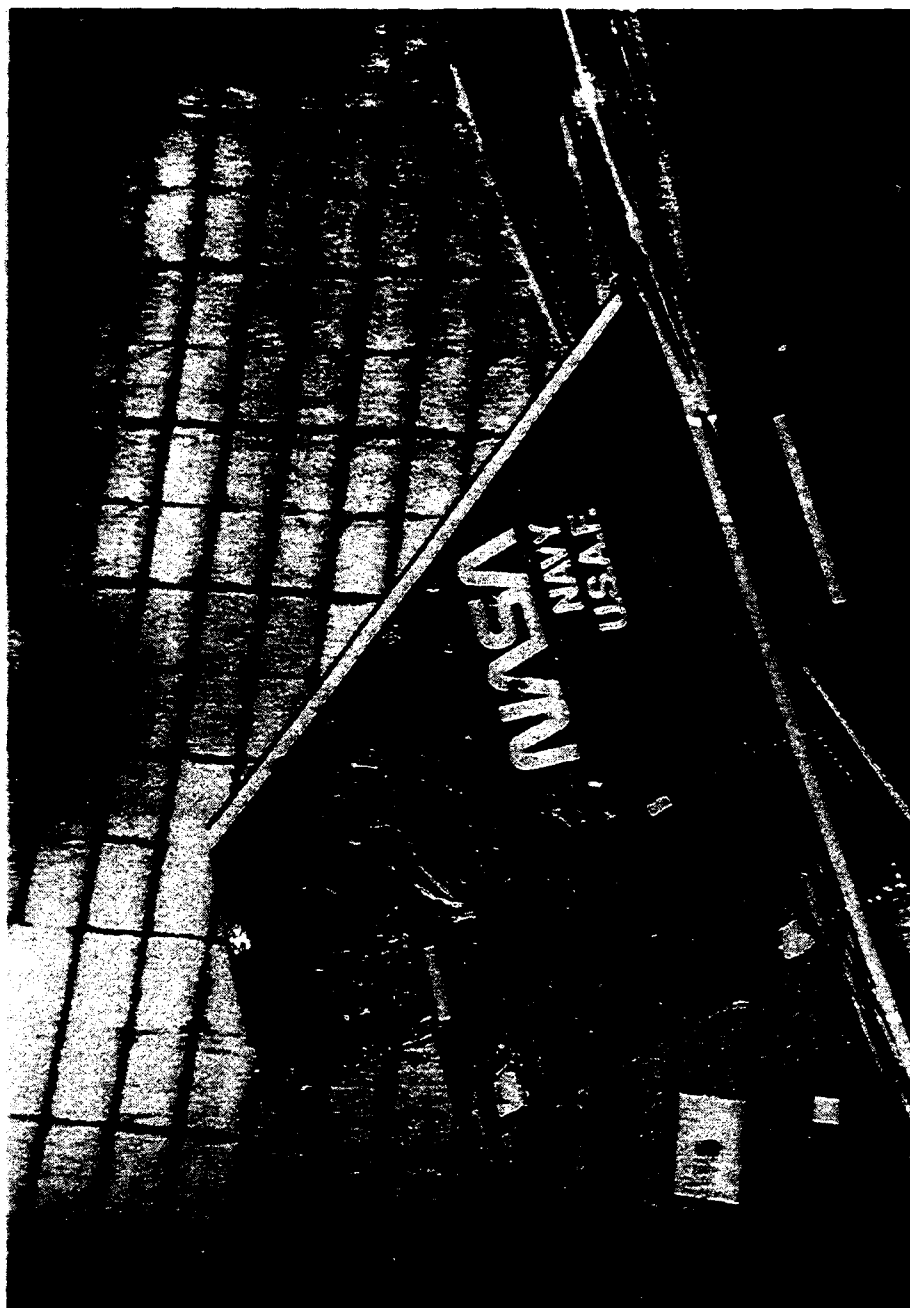


Figure 12. F/A-18 Outboard Starboard Tail with Pressure Transducers Installed



Figure 13. Inboard Tail instrumented with Transducers

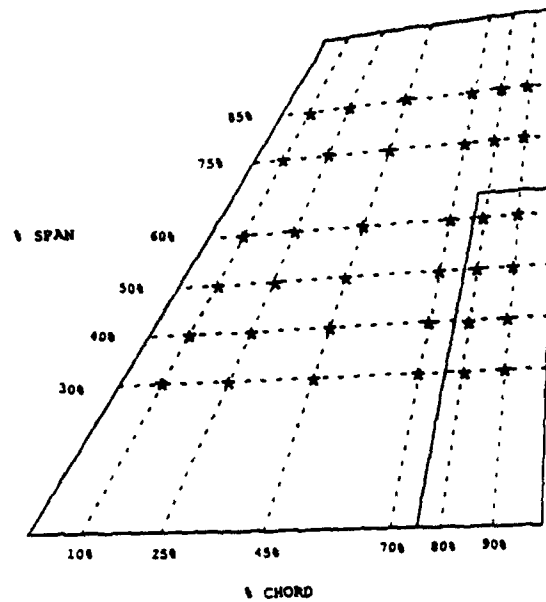


Figure 14. 6 by 6 Grid specified by early test plan

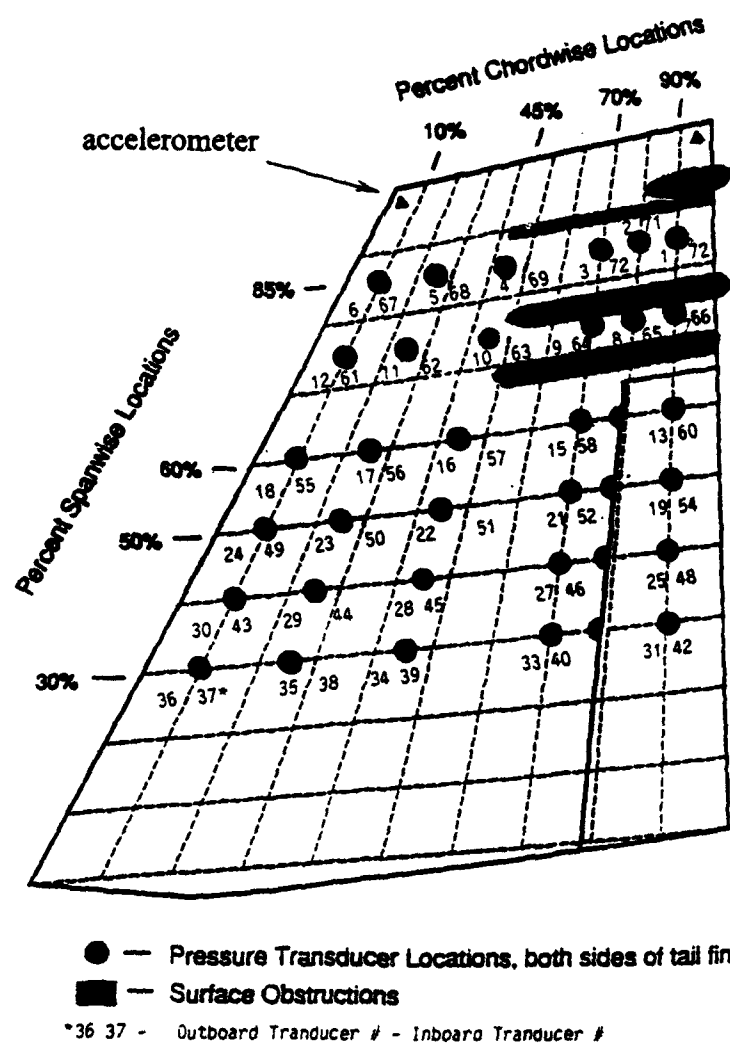


Figure 15. Actual 6 by 6 Grid Pressure Transducer Locations

locations in this figure are numbered from 1 through 72, where 1 through 36 correspond to the outboard side of the fin, and 37 through 72 to the inboard side.

Four Entran accelerometers (model # EGAX-250) with a ± 250 g range were mounted on the vertical fins of the test article to sense the buffeting response. Specifications from the manufacturer list an output nonlinearity of $\pm 1\%$ for these sensors. Two accelerometers were mounted on the inside tip of the starboard fin close to the leading and trailing edges, as shown in Figure 15. The signals generated by the leading and trailing edge transducer response were recorded on channels #76 and #75, respectively. The other two accelerometers were attached similarly to the port fin. The signals from the port fin leading and trailing edge transducers were recorded on channels #74 and #73, respectively. These locations were selected so that the transducers were positioned for optimum sensing of the bending and torsion dynamics of the fin. The accelerometers were attached to the fin surface using strain gage adhesive. The Entran model accelerometer was selected to maintain compatibility with the acceleration instrumentation used by NASA.

Pressure and acceleration data sensed by the transducers were acquired and recorded using the system illustrated schematically in Figure 16. The signals from each transducer were passed through a set of Aydin-Vector pulse code modulation (PCM) multiplexers (model # SCU-700-16) that digitized both the DC and AC signals generated by the buffet pressures into PCM output. Each Aydin-Vector multiplexer had sixteen channels and was equipped with differential input auto gain ranging amplifiers (AGRA). Each AGRA channel provided a dynamic gain range of 72 dB, a DC accuracy of $\pm .2\%$ for all gain settings, and a 6-pole butterworth low-pass response filter programmed to 500 Hz. The multiplexer PCM coded output was RNRZ-L format. At 500 Hz cutoff, the bit rate was programmed at 425 Kbits.

Five multiplexers were used to acquire the all 76 channels of data. The multiplexers were mounted to shelves in the avionics bays of the F/A-18, as illustrated in Figure 17. The transducers were connected to the multiplexers by forty (40) foot lengths of Microtek 4 conductor, 24 gage shielded cable that ran from the rudder hinge line through the fuselage aft end and passed through the aircrafts fuel cells to the avionics bay. This configuration allowed the cable length between each of the transducers and the digitization system to be minimized .

F-18 High-Alpha Test NASA/Ames, California

WL/ FLIGHT DYNAMICS DATA ACQUISITION SYSTEM

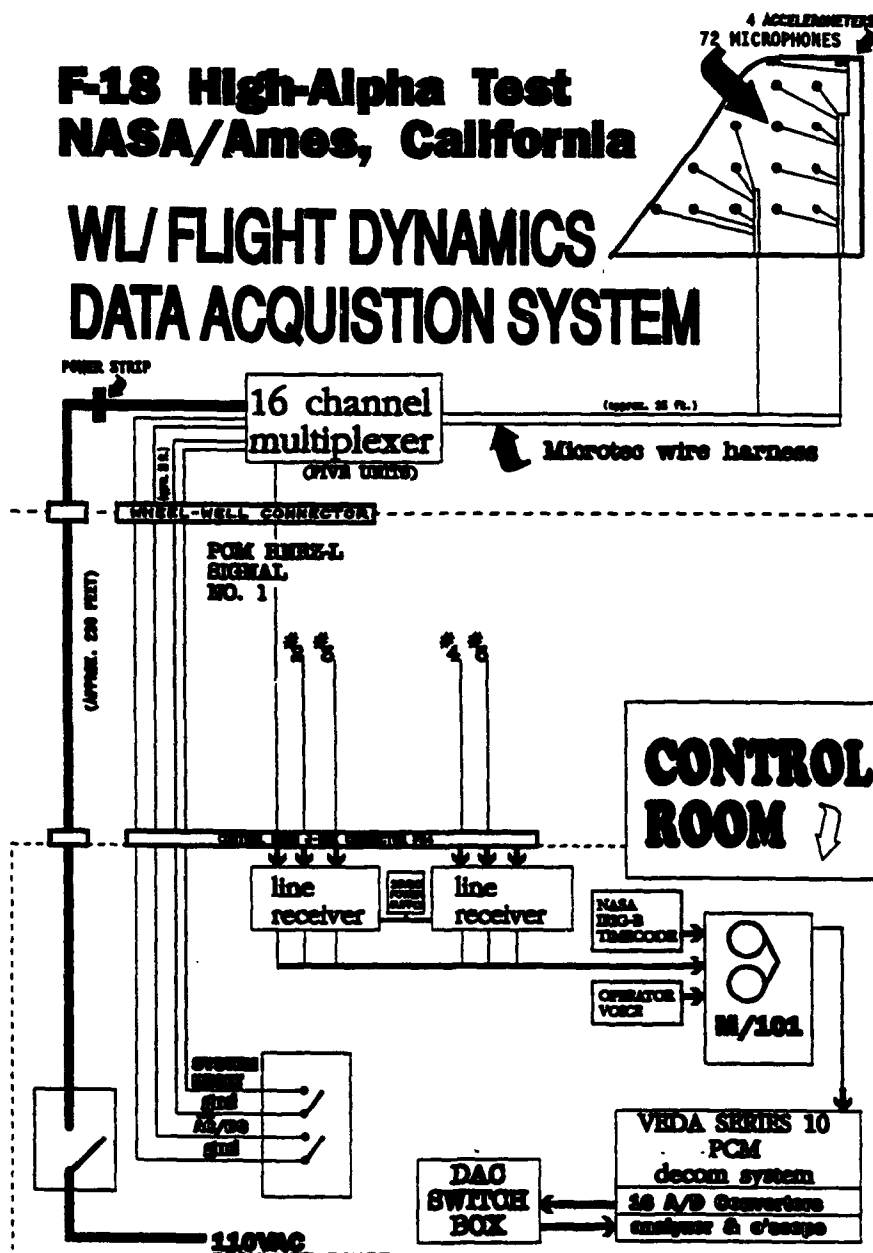


Figure 16. Schematic of Data Acquisition System

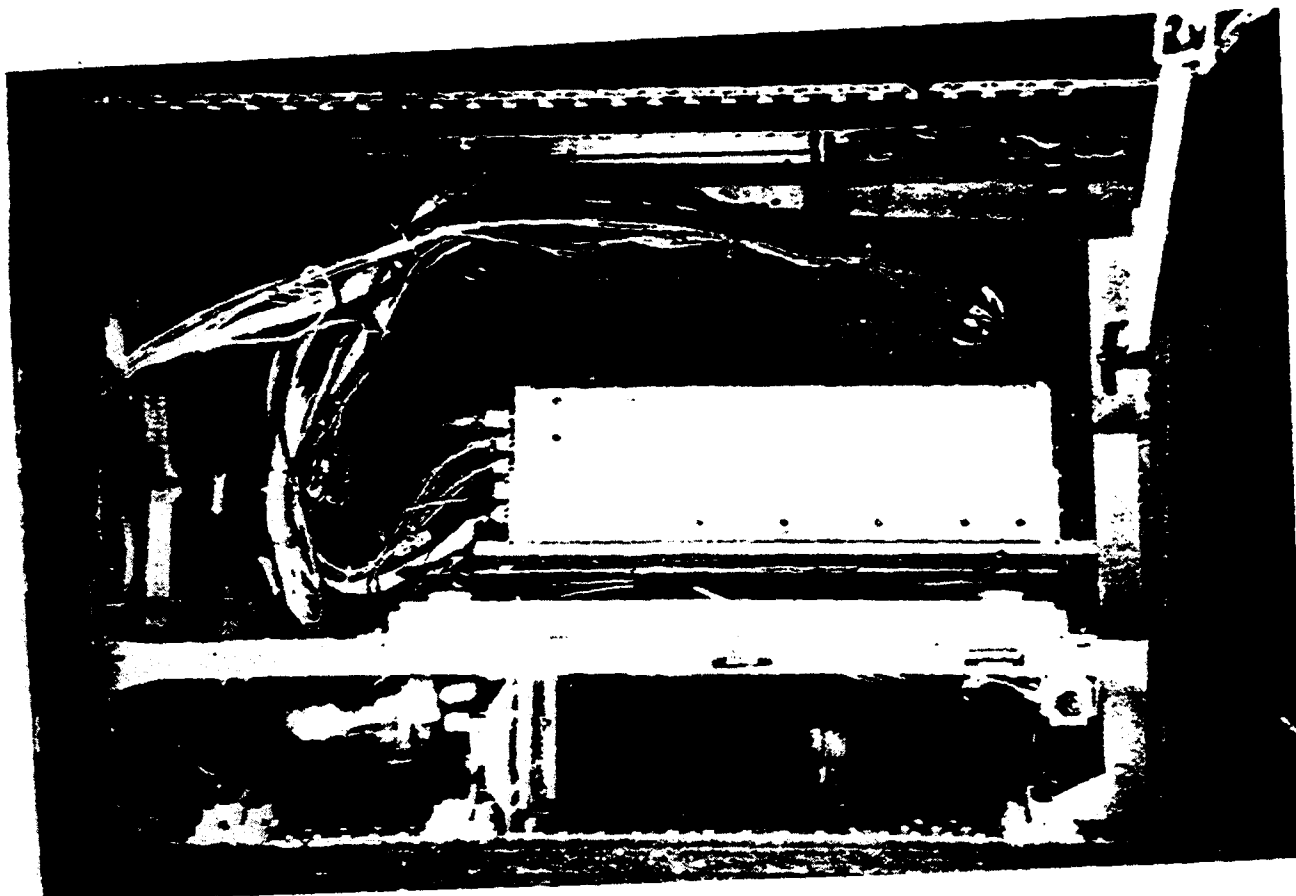


Figure 17. Multiplexer installed in F/A-18 Avionics Bay

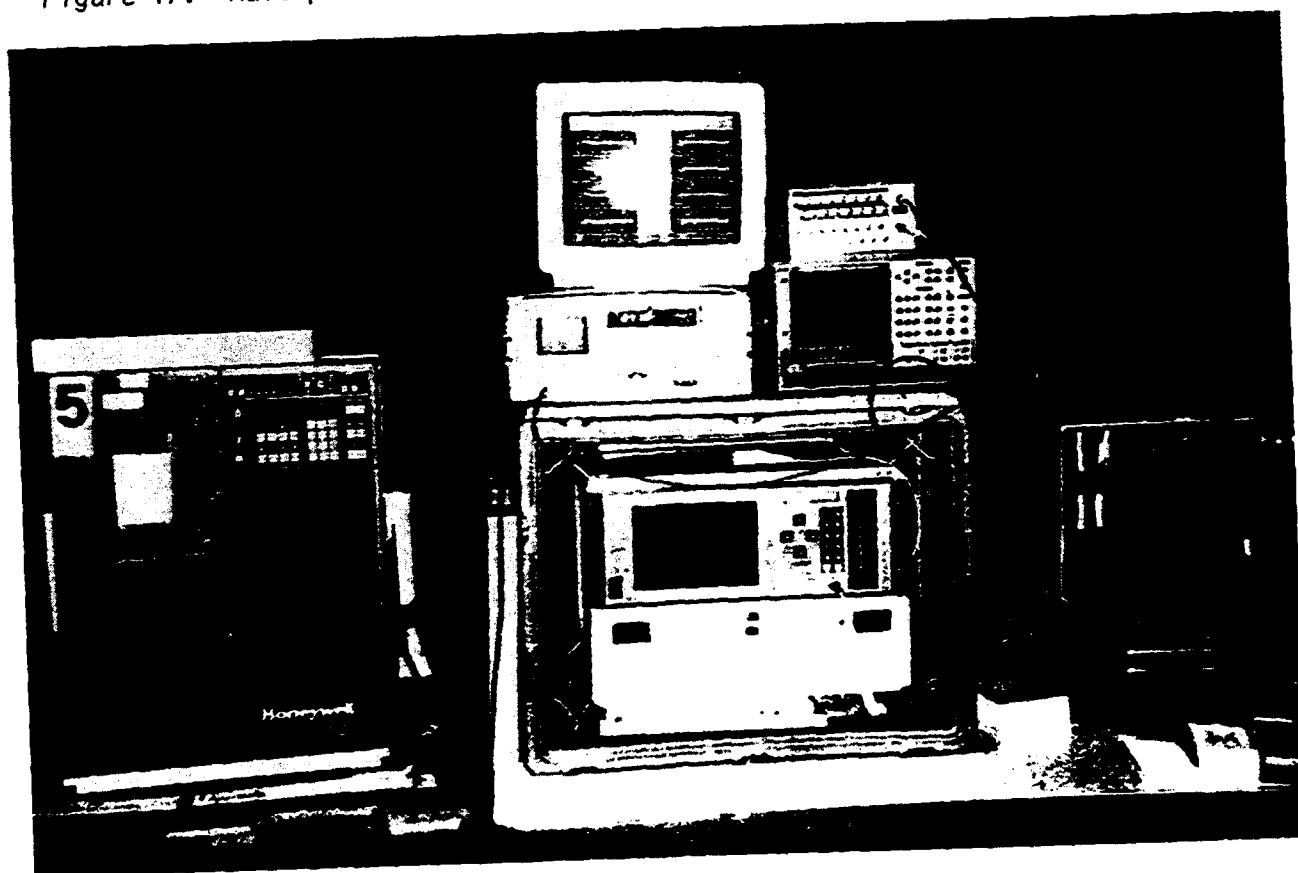


Figure 18. Data Acquisition Equipment in Control Room

The five PCM signals were sent from the multiplexers in the avionics bays along 15 feet of twin lead shielded cable to the F/A-18's starboard wheelwell, down another 100 feet of cable along the strut to the facility patch panel, and then through an additional 150 feet of cable into the control room. The PCM signals were routed through a line receiver that stabilized the signals. Then the PCM signals were recorded in the wind tunnel control room on 14 track magnetic tape by a Honeywell recorder (model # M/101). The recorded signal was monitored through a Veda ITAS Series 10 PCM Decomutator (Decom) unit. The control room equipment which comprised the data acquisition system is shown in Figure 18.

Section III

Test Program

The wind tunnel buffet tests were conducted during a ten day period in August 1993 at the NASA Ames NAFC 80 by 120 foot tunnel. Both steady and unsteady pressure measurements, as well as acceleration data, were obtained for sixty-four (64) test conditions. Four of the test conditions were at a dynamic pressure of 20 lb/ft², and sixty of the conditions were at the maximum tunnel dynamic pressure of 33 lb/ft². During the tests, pressure measurements were collected as the static angle-of-attack, α , was varied through a range from 20 to 40 degrees at zero sideslip. Measurements were also obtained as the static aircraft sideslip angle, β , was varied from -16 to 16 degrees at angles-of-attack of both 30 degrees and 35 degrees. Measurements were taken both with and without the LEX fence both deployed.

At each test condition, the steady pressure was recorded for 30 seconds with the multiplexers operating in the direct current (DC) mode. Unsteady pressure data were then recorded for 30 seconds with the multiplexers operating in the alternating current (AC) mode. The steady and unsteady signals were sampled and monitored by spectrum analyzer after passing through the PCM Decom unit. Seventy two channels of pressure data and four channels of acceleration data were recorded.

The sixty-four (64) test conditions for which pressures and accelerations were measured are summarized in Table 2. The parameters listed include the static angles-of-attack, α , and sideslip, β , for each run along with the use of the LEX fence. Positive sideslip is nose left from the pilot's perspective. Freestream velocity, Reynolds number (based on the wing's mean aerodynamic chord), and Mach number are also given for each test condition. The current freestream data listed in Table 1 are only approximate in that they represent the average values encountered over several test conditions.

Following the wind tunnel test, a post-test inspection of the instrumentation was conducted to evaluate the condition of each pressure transducer. The inspection revealed that the

Table 2. F/A-18 Full-Scale Wind Tunnel Test Conditions

Run #	LEX Fence	α (deg)	β (deg)	U_{∞} (ft/s)	q (psf)	Reynolds No. [*]	Mach No.	Sweep Values ^{**} (deg)
1	off	sweep	0	168	33	1.2×10^7	0.15	<u>20,24,26,28,30,32</u> , 36,40
2	off	35	sweep	168	33	1.2×10^7	0.15	16,10,6,4,2,0,-2,-4, <u>-6,-10,-16</u>
3	off	30	sweep	168	33	1.2×10^7	0.15	16,10,6,4,2,0,-2,-4, <u>-6,-10,-16</u>
4	off	sweep	0	102	20	0.73×10^7	0.09	26,28
5	on	sweep	0	168	33	1.2×10^7	0.15	<u>20,24,26,28,30,32</u> , 36,40
6	on	35	sweep	168	33	1.2×10^7	0.15	16,10,6,4,2,0,-2,-4, <u>-6,-10,-16</u>
7	on	30	sweep	168	33	1.2×10^7	0.15	16,10,6,4,2,0,-2,-4, <u>-6,-10,-16</u>
8	on	sweep	0	102	20	0.73×10^7	0.09	26,28
* Based on the mean aerodynamic chord of 11.54 ft.								
** Underlined sweep values correspond to important buffet test cases cited in text.								

wire from transducer #26 had severed. All remaining transducers appeared functional, but some were slightly fouled with residue from test fogging mixture.

An initial reduction of the raw signals from steady data revealed additional clues about transducer condition. Differences of steady pressure, computed using raw data from corresponding inside and outside pairs of transducers at each fin station, were plotted on a 6-by-6 grid. These plots confirmed that transducer #26 was inoperative during the entire wind tunnel test. These pressure plots also indicated that transducer #22 was functional for only a portion of the test and was inoperative for data records 66-79. Pressure differences across the fin determined using transducer pairs #20 and #53 and #29 and #44 appeared to be inconsistent with the steady data from the other stations' transducers. Further inspection of the raw signals from these transducer pairs indicated that the signals from transducers #20, #53 and #44 were inconsistent with the signals from the other transducers. Overall, the conclusion from evidence gathered during the post test inspections and steady data reduction is that transducers #26 was nonfunctional for all records, transducers #20, #44 and #53 were functioning improperly for all records and #22 was nonfunctional for data records 66-79.

Section IV

Data Reduction Techniques

The buffet pressure and acceleration data recorded at the wind tunnel test site were processed at the Structural Dynamics Branch Data Analysis Facility at Wright Patterson AFB, Ohio. The PCM signals, stored on 14 track data tapes, were replayed in order to digitize all seventy-six channels of data onto VAX disks. All sixty-three test conditions and one baseline wind-off condition were digitized.

The pressure signals were initially processed by subtracting the pressure values obtained during the baseline wind-off run. This process, which was required because the microphones could not be nulled in the tunnel, ensured that all pressures were being measured relative to the proper zero reference levels. All pressure signals were converted to actual pressures for each of the pressure sensors using the microphone sensitivity factors listed in Table 3.

The unsteady, or buffet, pressures were assumed to be zero-mean, stationary random process amenable to standard analysis techniques in the time and frequency domains. Pressure differential time histories were computed at each transducer-pair station for each test condition by subtracting the outer surface pressure reading from the inner surface pressure reading at each time step. Along with the fin-tip acceleration data, these data were converted to the frequency domain using Fast Fourier Transform techniques. Approximately 15 seconds of data from each test condition were divided into blocks, each containing 2048 samples. A Hanning window was applied to reduce bandwidth leakage, and an average of 22 transforms with 50% overlap was used to increase statistical confidence. The resulting frequency resolution was 0.8 Hz. Power spectral density (PSD) functions were computed from the Fourier transforms. Root-mean-square (RMS) buffet pressures and accelerations were then derived from the PSDs via numerical integration.

F-18 Tail Buffet Test

MUX # 1				MUX # 2			
	location	mv/eu	eu/ct		location	mv/eu	eu/ct
word 1	1	9.958	0.4903		17	9.921	0.4922
word 2	2	10.237	0.4770		18	10.03	0.4868
word 3	3	10.124	0.4823		19	10.186	0.4794
word 4	4	10.204	0.4785		20	10.069	0.4849
word 5	5	10.206	0.4784		21	10.085	0.4842
word 6	6	9.829	0.4968		22	11.504	0.4244
word 7	7	10.156	0.4808		23	10.075	0.4846
word 8	8	10.048	0.4859		24	9.929	0.4918
word 9	9	10.154	0.4809		25	10.305	0.4738
word 10	10	10.177	0.4798		26	10.084	0.4842
word 11	11	9.993	0.4886		27	10.058	0.4855
word 12	12	10.161	0.4805		28	9.985	0.4890
word 13	13	10.028	0.4869		29	10.19	0.4792
word 14	14	9.946	0.4909		30	10.055	0.4856
word 15	15	10.215	0.4780		31	9.998	0.4884
word 16	16	10.07	0.4849		32	10.063	0.4852

MUX # 3				MUX # 4			
	location	mv/eu	eu/ct		location	mv/eu	eu/ct
word 1	33	10.164	0.4804		47	10.154	0.4809
word 2	34	10.147	0.4812		48	10.011	0.4877
word 3	35	10.106	0.4832		49	10.178	0.4797
word 4	36	10.057	0.4855		50	9.845	0.4960
word 5	37	10.073	0.4847		51	9.938	0.4913
word 6	38	10.025	0.4871		52	9.985	0.4890
word 7	39	10.254	0.4762		53	10.027	0.4870
word 8	40	10.096	0.4836		54	10.168	0.4802
word 9	41	10.088	0.4840		55	9.905	0.4930
word 10	42	9.972	0.4897		56	9.983	0.4881
word 11	43	10.098	0.4835		57	9.924	0.4920
word 12	44	9.956	0.4904		58	9.995	0.4885
word 13	45	10.012	0.4877		59	10.038	0.4864
word 14	46	9.883	0.4941		60	10.025	0.4871
word 15	74	0.996	4.9024 *		74	0.996	4.9024 *
word 16	76	1.01	4.8345 *		76	1.01	4.8345 *

MUX # 5			
	location	mv/eu	eu/ct
word 1	61	10.144	0.4813
word 2	62	10.284	0.4748
word 3	63	10.217	0.4779
word 4	64	9.821	0.4972
word 5	65	10.246	0.4766
word 6	66	9.96	0.4902
word 7	67	9.9	0.4932
word 8	68	10.099	0.4835
word 9	69	9.987	0.4889
word 10	70	10.096	0.4836
word 11	71	12.015	0.4064
word 12	72	10.012	0.4877
word 13	73	1.01	4.8345 *
word 14	75	1.02	4.7871 *
word 15	74	0.996	4.9024 *
word 16	76	1.01	4.8345 *

eu/ct = (mv/ct)/(mv/eu) where mv/ct = 4.882812

eu = psi except for those indicated with * in g's

Table 3. Kulite Microphone Sensitivities

Section V

Results and Discussion

Steady Pressures

The steady pressure DC signals were converted to steady pressures, \bar{p} , for each of the pressure sensors using the microphone sensitivity factors. Baseline values for each pressure sensor were determined under atmospheric, or wind-off, conditions in the tunnel. These reference levels were then subtracted from all subsequent pressure readings to yield the gauge static pressures for each loading condition. Steady pressure differences at each transducer-pair station were computed by subtracting the mean of the outer surface transducer signal from the mean of the inner surface transducer signal.

The steady pressure coefficients were calculated using the relation

$$C_{\bar{p}} = (\bar{p} - p_{\infty})/q_{\infty}$$

where p_{∞} is the gauge freestream static pressure and $q_{\infty} = \frac{1}{2}\rho_{\infty}U_{\infty}^2$ is the freestream dynamic pressure. Differential pressure coefficients between each of the transducer pairs depicted in Figure 15 were determined using the following relation:

$$C_{\Delta\bar{p}} = \Delta\bar{p}/q_{\infty} \text{ where } \Delta\bar{p} = (\bar{p}_{\text{inside}} - \bar{p}_{\text{outside}}).$$

Thus, a positive pressure difference across the fin at a given transducer station corresponds to a higher pressure on the inside surface of the vertical tail than on the outside surface. The calculations were performed for both the "LEX-fence off" and "on" cases at $q = 33 \text{ psf}$ and 20 psf .

The $\alpha = 32^\circ$ test condition at zero sideslip is presented as a primary example case for examination in Volume I due to the severity of the buffet loads normally encountered at this angle-of-attack. All other data from remaining test conditions are presented in subsequent Volumes of this report.

Surface and contour plots of the steady pressure differential acting on the vertical tail at the $\alpha = 32^\circ$ at $\beta = 0^\circ$ LEX fence-off test condition are shown in Figures 19 and 20. Tables of

F-18 Tail Buffet Test

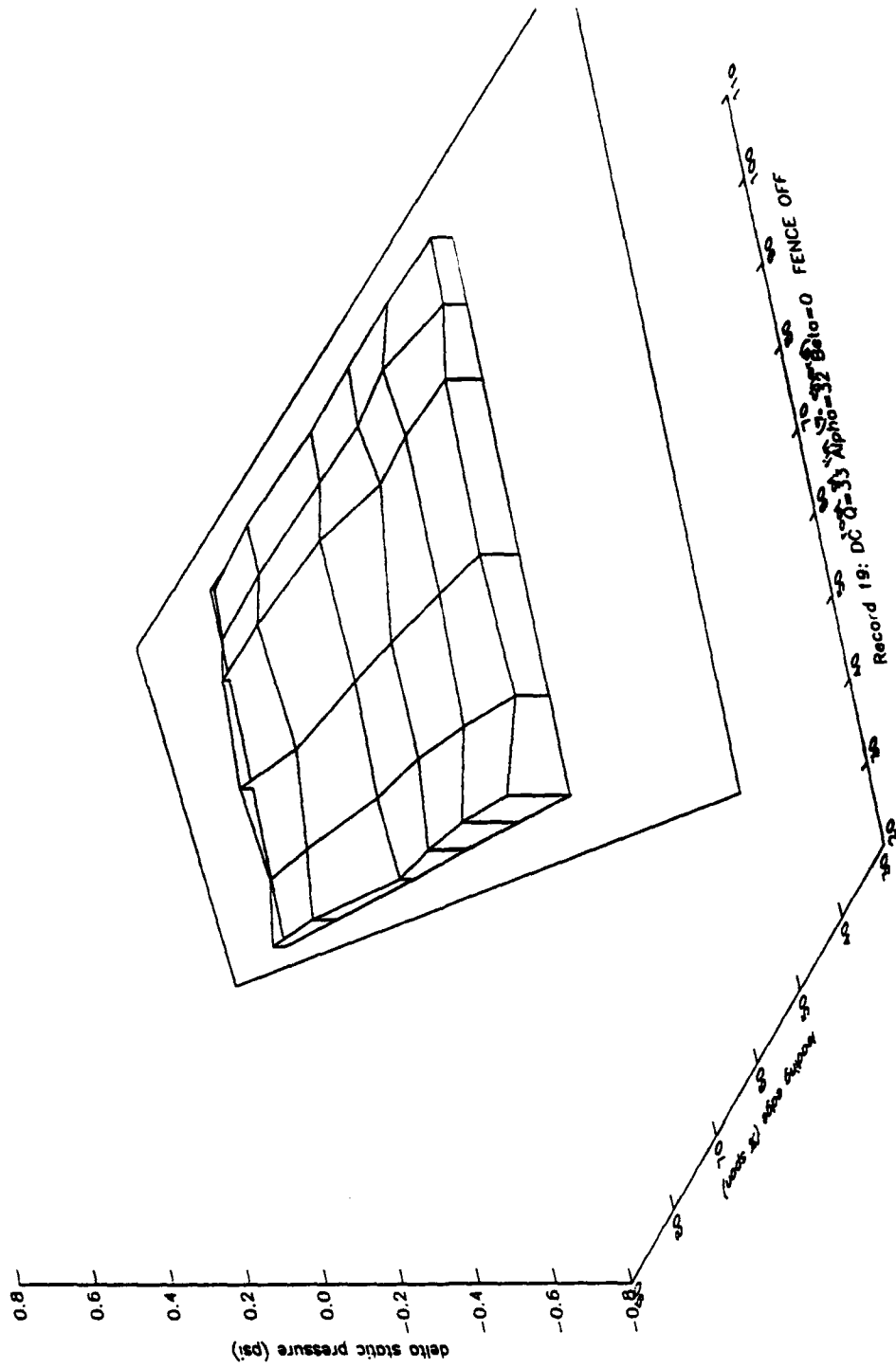


Figure 19. Steady Pressure Differential acting on Starboard Tail, $\alpha = 32$ degrees

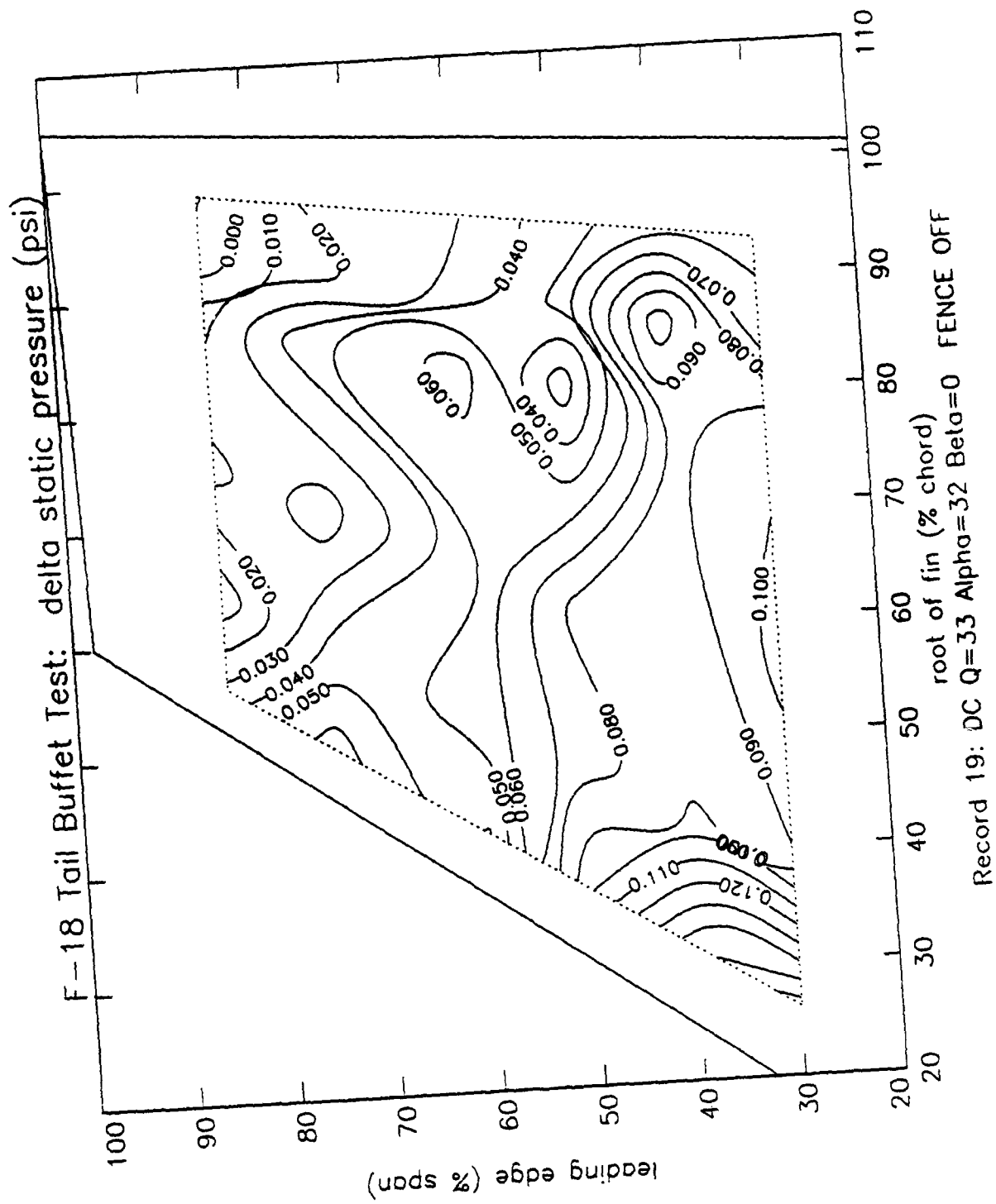


Figure 20. Steady Pressure Differential acting on Vertical Tail- Contour Plot, alpha = 32 degrees

corresponding steady pressure coefficients and differentials for this condition and the remaining sixty-two test conditions are presented in Volume II of this report. These pressure tables are followed by surface and contour plots of the steady pressure differential acting on the vertical tail for each test case.

The majority of steady pressure plots generated from this wind tunnel test exhibit gentle gradients, indicating fairly smooth distributions of the steady pressures on the fin. Interpolation lines on the surface plots were drawn by connecting local pressure readings in a linear fashion, and the level curves on the contour plots were determined using cubic splines.

The surface plot depiction in Figure 19 provides a quick review of the steady loading on the fin, while the contour plot format shown in Figure 20 supplies a detailed picture of the steady pressure distribution, especially where large gradients exist. Proper interpretation of contour plots requires added care since these plots may imply a higher degree of spatial resolution than actually is present in the steady pressure data.

The transducer failures listed in the previous section were accounted for in an approximate fashion during the reduction of the steady pressure data. Where possible, the pressure signals from the nonfunctional transducers were replaced by averaged values of the pressures from their four closest neighbors. An alternative scheme was used for faulty transducer pairs 20-53 and 26-47, which are adjacent to one another along the hinge line. The pressures at these stations were replaced by the values from their two closest neighbors along the corresponding chord lines.

Steady Aerodynamic Loads

The steady pressure differentials were integrated in a piece-wise continuous manner to obtain the steady normal force and root bending moment for each test condition. The planform of the fin was divided into thirty-six (36) area elements, one for each of the transducer pairs, as illustrated in Figure 21. The steady normal force coefficient for each test case was then determined according to:

$$C_{\bar{N}} = \frac{1}{q_{\infty} A_F} \sum_{j=1}^{36} \Delta \bar{p}_j A_j$$

where A_F is the total fin area, A_j is the area of the j -th element, and $\Delta \bar{p}_j$ is the steady pressure differential at the j -th transducer pair. The area elements were chosen based on the transducer grid pattern. The resulting nonuniform sizing of these elements unavoidably forced some of the pressures to be weighted more heavily than others in the above summation.

The steady root bending moment for each test case was calculated in a similar manner. The resultant force over each element was assumed to act at the element's centroid, so that the steady bending moment coefficient was approximated by:

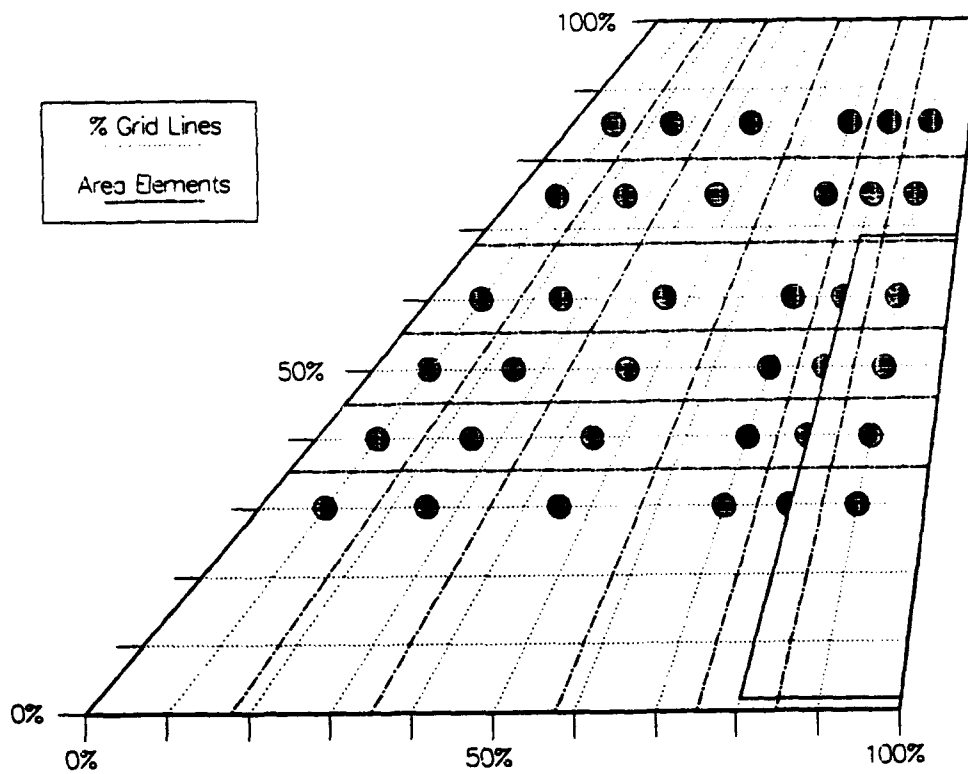
$$C_{\bar{M}_B} = \frac{1}{q_{\infty} A_F \bar{c}} \sum_{j=1}^{36} \Delta \bar{p}_j A_j \bar{y}_j$$

where $\bar{c} = 11.54 \text{ ft}$ is the mean aerodynamic chord and \bar{y}_j is perpendicular distance from the fin root to the centroid of the j -th element. The wing's mean aerodynamic chord was selected as the characteristic length to maintain a single characteristic length consistent with that used in processing the unsteady pressure results. This characteristic length is also compatible with those used in previous buffet research, such as Zimmerman and Ferman (1987) and Meyn and James (1993).

Plots of the steady normal force and bending moment coefficients for both the fence-off and -on conditions are shown in Figures 22 and 23. The plots in Figure 22 show the variation of $C_{\bar{N}}$ and $C_{\bar{M}_B}$ vs. α at zero sideslip, and the plots in Figure 23 show the variation of $C_{\bar{N}}$ and $C_{\bar{M}_B}$ vs. β at $\alpha = 30^\circ$ and $\alpha = 35^\circ$.

The graphs depicting the steady normal force on the fin versus angle-of-attack have several interesting characteristics. The plots show a consistent reduction of the steady normal force on the fin at angles-of-attack between 20 and 30 degrees when the LEX fence is deployed. A large dip in normal force on the fin appears in the LEX fence off data at 32° . The origin of this effect is not clear. Above 32 degrees angle-of-attack, the steady normal force coefficients tend to level off for both the LEX fence off and on cases.

Similar trends are exhibited by the steady bending moment plots in Figure 22, especially the large dip at 32 degrees for the fence-off case. However, the root bending moment coefficient



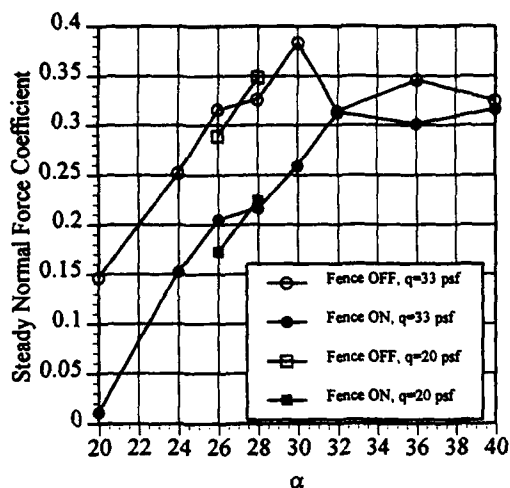
Dimensions in inches

Distances with respect to
leading edge, root location

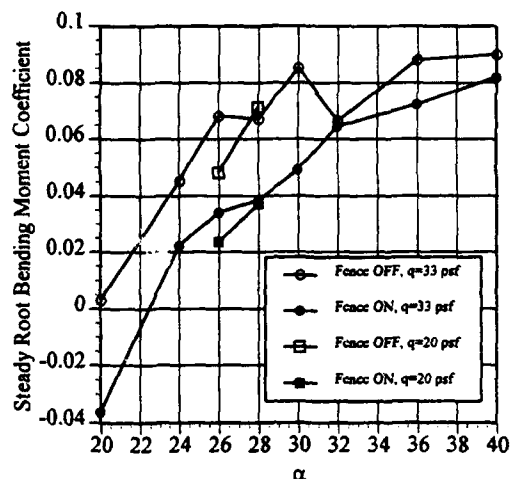
	ELEMENT COLUMN 1-Leading Edge			ELEMENT COLUMN 2			ELEMENT COLUMN 3		
	Area	X centroid	Y centroid	Area	X centroid	Y centroid	Area	X centroid	Y centroid
Element Row 1-Root	588.28	22.93	15.97	588.28	40.70	15.97	756.35	61.02	15.97
Element Row 2	142.64	40.86	37.94	142.64	55.89	37.94	183.40	73.06	37.94
Element Row 3	131.34	48.62	47.43	131.34	62.45	47.43	168.86	78.26	47.43
Element Row 4	148.27	57.30	58.07	148.27	69.80	58.07	190.64	84.06	58.07
Element Row 5	130.61	66.98	69.93	130.61	78.00	69.93	167.93	90.59	69.93
Element Row 6-Tip	172.24	79.36	85.06	172.23	88.48	85.06	221.45	98.90	85.06
Area Total per Column	1313.38			1313.38			1888.63		

	ELEMENT COLUMN 4			ELEMENT COLUMN 5			ELEMENT COLUMN 6-Trailing Edge		
	Area	X centroid	Y centroid	Area	X centroid	Y centroid	Area	X centroid	Y centroid
Element Row 1-Root	588.28	81.33	15.97	336.16	95.30	15.97	504.24	107.99	15.97
Element Row 2	142.64	90.22	37.94	81.51	102.03	37.94	122.26	112.76	37.94
Element Row 3	131.34	94.07	47.43	75.05	104.94	47.43	112.58	114.82	47.43
Element Row 4	148.27	98.38	58.07	84.73	108.20	58.07	127.09	117.13	58.07
Element Row 5	130.61	103.16	69.93	74.63	111.83	69.93	111.95	119.70	69.93
Element Row 6-Tip	172.23	109.32	85.06	96.42	116.48	85.06	147.63	122.99	85.06
Area Total per Column	1313.38			750.50			1125.75		

Figure 21. Fin Area Elements and corresponding Transducer Locations

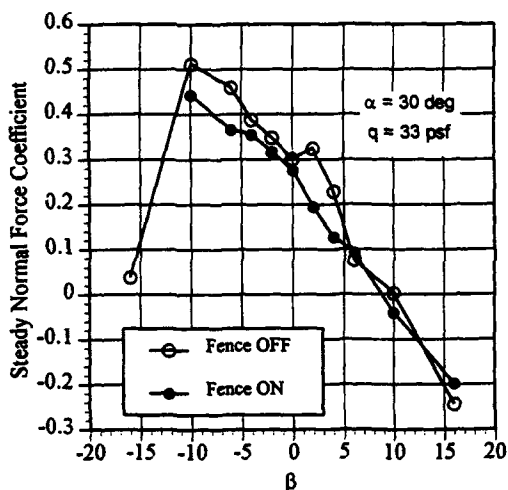


(A) Normal Force Coeff.

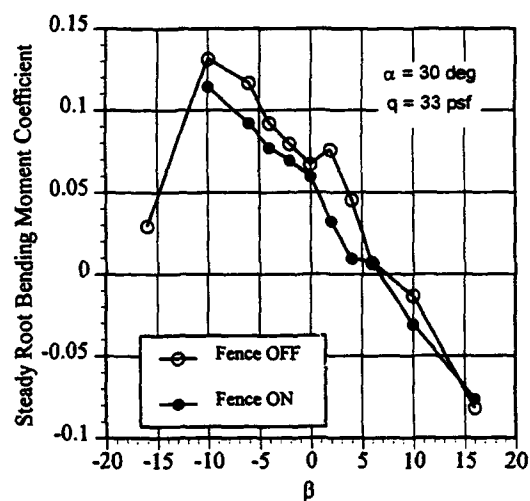


(B) Bending Moment Coeff.

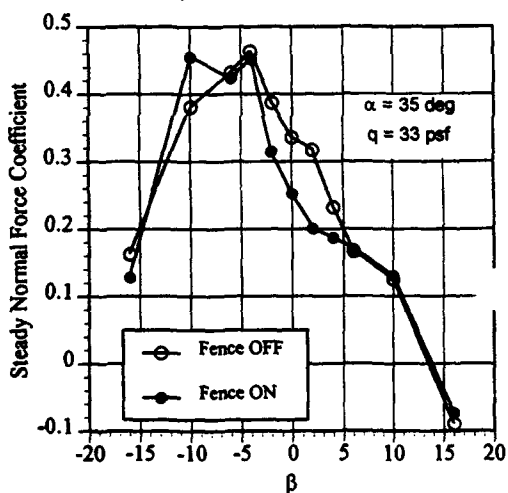
Figure 22. Steady Normal Force and Root Bending Moment Coefficients versus Angle-of-Attack at Zero Sideslip



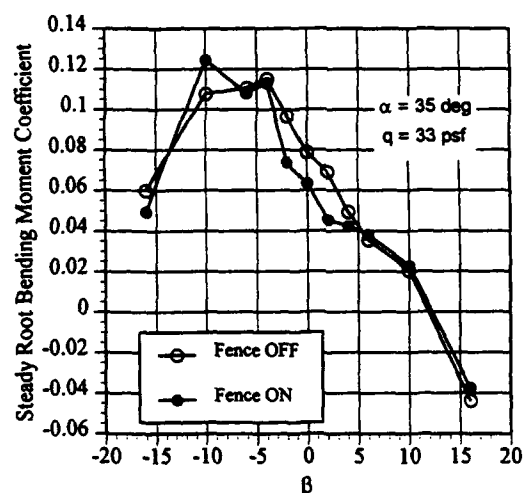
(A) Normal Force Coeff.



(B) Bending Moment Coeff.



(C) Normal Force Coeff.



(D) Bending Moment Coeff.

Figure 23. Steady Normal Force and Root Bending Moment Coefficients versus Sideslip

continues to increase slightly above this angle-of-attack for both conditions. This is most likely caused by the variation of the peak steady pressure locations on the fin as the angle-of-attack is increased, since the vortex shed from the starboard LEX may be expected to pass closer to the fin's tip as angle-of-attack is increased. This conclusion is supported by data from Lee et al. (1993), who measured the steady total pressure contours behind the vertical fins of a rigid 6% scale F/A-18 model. Their contour plots of the steady pressure field behind the vertical tails show that the extrema tend to be located closer to the fin tips as the steady angle-of-attack is increased.

The variations of normal force and root bending moment with sideslip in Figure 23 also show decreases in steady loading with deployment of the LEX fence, but the effects are not so strong as those caused by variation in angle-of-attack. A notable feature of both the steady normal force and bending moment plots for the fence-off conditions is the local maximum exhibited by the $\alpha = 30^\circ$ curves at $\beta = +2^\circ$. The origin of this effect is unknown, and the $\alpha = 35^\circ$ results in Figure 23 do not exhibit a similar peak. Another feature of the data is the significant non-zero loading on the fin at $\beta = 0^\circ$, which is due most likely to the local angle-of-attack distribution on the fin generated by the upstream flow separation from the LEX and the wing. The LEX fence appears to have little effect on the fin loading for $\beta \geq 6^\circ$, especially at $\alpha = 35^\circ$. This implies that for large positive values of sideslip, the vortex shed from the starboard LEX does not interact significantly with the starboard vertical fin.

Finally, note that no data are presented for the $\beta = -16^\circ$ test point at $\alpha = 30^\circ$ with the LEX fence on. No data was taken in the wind tunnel for this test point.

Unsteady Pressures—Root-Mean-Square Fluctuations

Root-mean-square (RMS) differential buffet pressures were computed for each pair of pressure transducer signals at all test conditions. The buffet pressure coefficient of the zero-mean, unsteady pressure measured by a given transducer, $p(t)$, is defined by

$$C_p(t) = (p(t) - p_\infty)/q_\infty$$

in the same manner as the steady pressure coefficient. Unsteady differential pressure coefficients were determined from the equation

$$C_{\Delta p}(t) = \Delta p(t)/q_{\infty} \text{ where } \Delta p(t) = p_{inside}(t) - p_{outside}(t).$$

The resulting RMS differential pressure coefficient from a given transducer pair is then denoted by $C_{\Delta p'}$, where

$$(\Delta p)' = \lim_{T \rightarrow \infty} \frac{1}{T} \int_0^T [\Delta p(t)]^2 dt = p'_{inside} + p'_{outside} - 2R_{p_{inside}p_{outside}}(\tau = 0)$$

is the RMS pressure differential and $R_{p_{inside}p_{outside}}(\tau)$ is the cross-correlation of the inside and outside pressures at a given location on the fin. This definition of the RMS differential pressure is provided only to highlight the terms that compose $C_{\Delta p'}$. Computational considerations dictate that RMS quantities be calculated from the power spectral densities to be discussed later.

$C_{\Delta p'}$ provides a measure of the average fluctuation in the unsteady net force per unit area at a given transducer-pair station. The RMS differential pressure coefficient, as defined in the above equation, should not be confused with the difference of the RMS pressure coefficients, $(C'_{p_{inside}} - C'_{p_{outside}})$. The definition of the RMS differential pressure coefficient, $C_{\Delta p'}$, was validated by Zimmerman and Ferman (1987), who showed that the RMS buffet pressure at a given location on a fin is a linear function of the dynamic pressure.

Figures 24A and 24B are surface plots of the RMS differential pressure coefficient for the $\alpha = 32^\circ, \beta = 0^\circ$ test case with the LEX fence off and on, respectively. Figures 25A and 25B are contour plots showing the same data. These plots were constructed using the methods described in the previous section. The reduction in buffet levels due to use of the LEX fence may be seen by comparing Figures 24A with 24B, or 25A with 25B. These plots show that the largest reductions in the unsteady pressures imposed upon the fin occurred near the leading edge and in the outboard region at this angle-of-attack. A general reduction in the level of buffet on the fin was also realized through use of the fence.

Similar surface and contour unsteady RMS plots for all test cases are located in Volume II of this report, along with tables tabulating the numerical values for each of the thirty-six (36) stations on the fin. Many of these RMS differential pressure coefficient distributions are quite

F-18 Tail Buffet Test

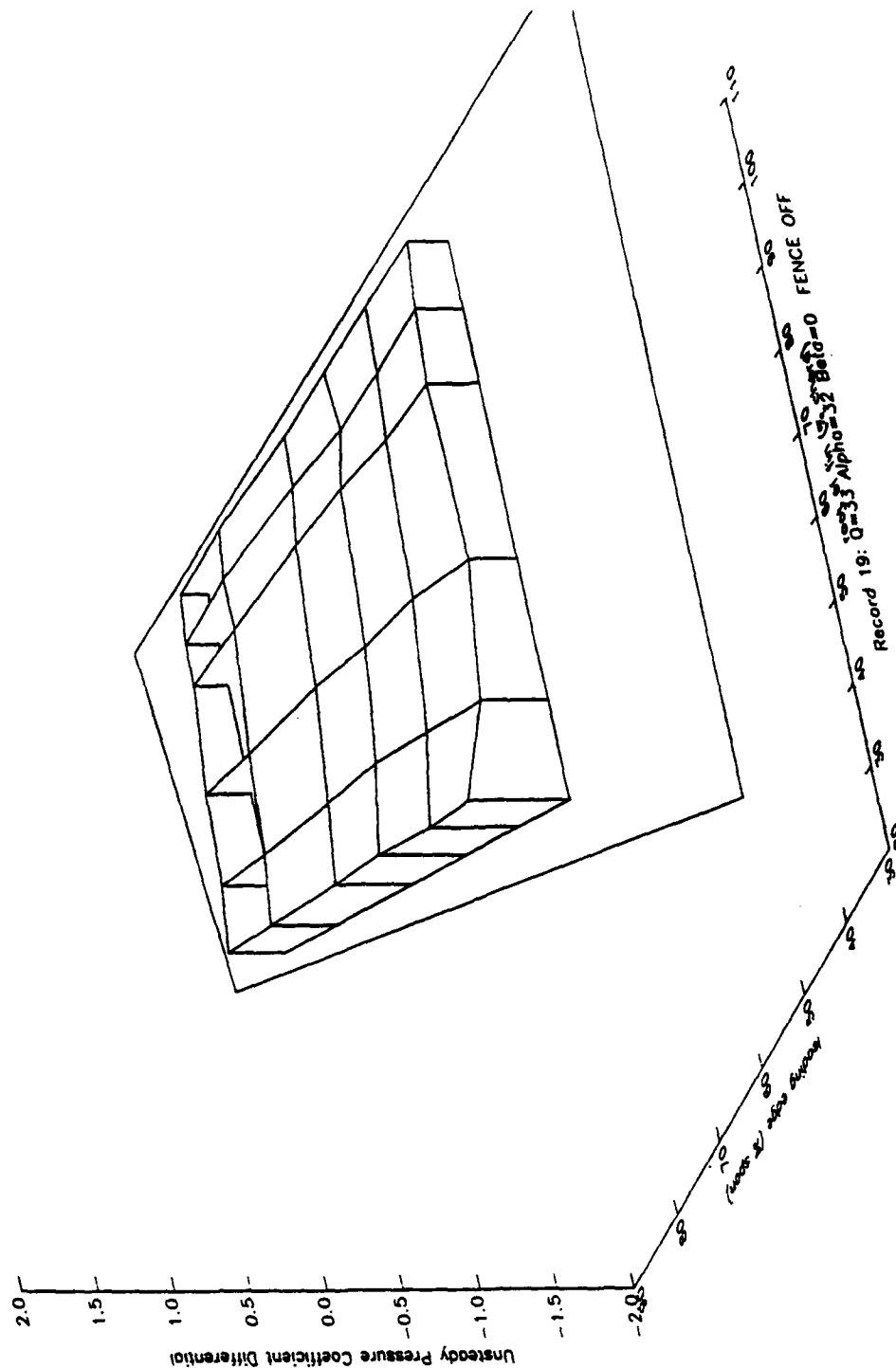


Figure 24A. RMS Pressure Differential Plot for angle of attack of 32 degrees, Fence Off

F-18 Tail Buffet Test

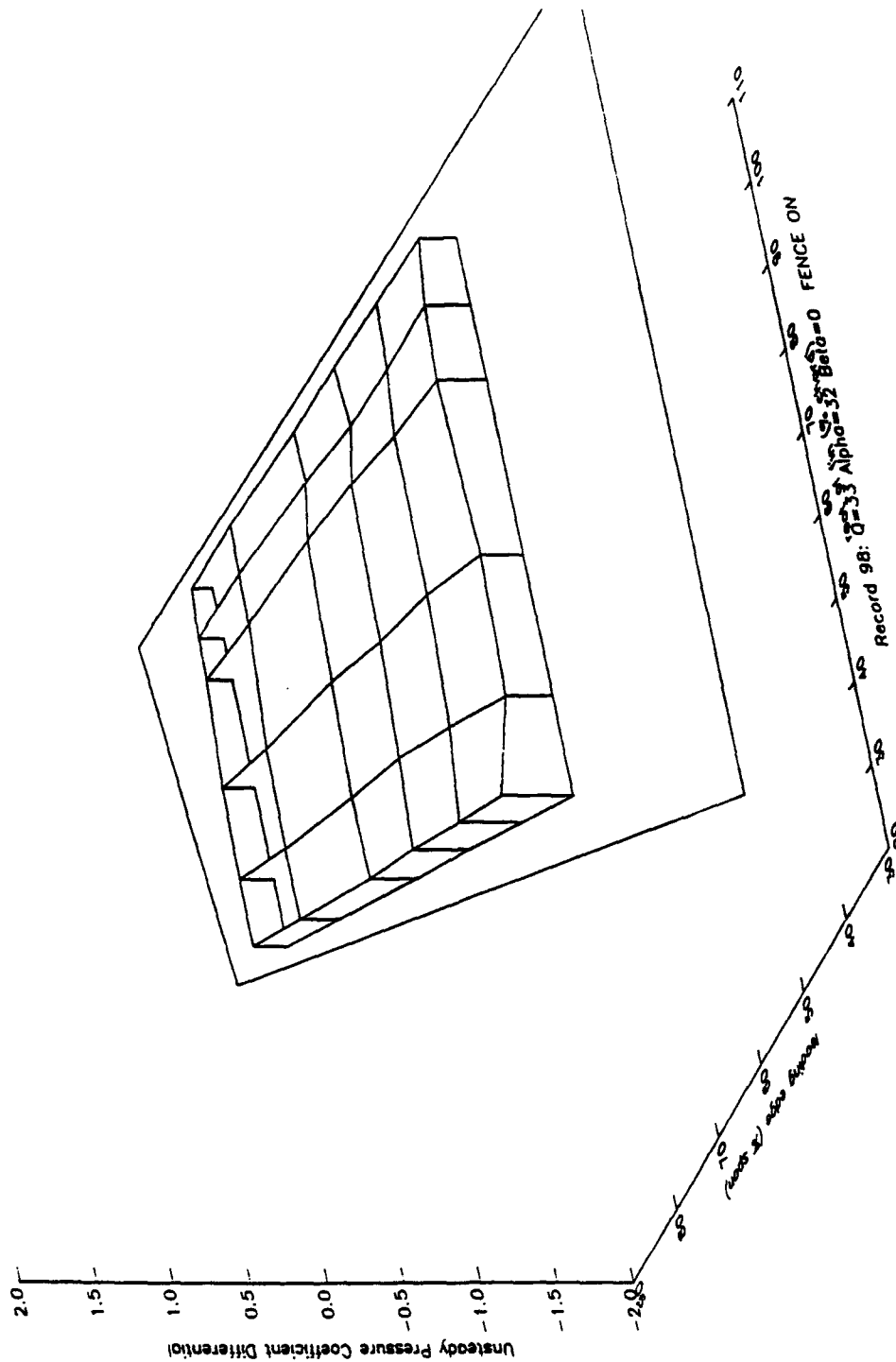


Figure 24B. RMS Pressure Differential Plot for angle of attack of 32 degrees, Fence On

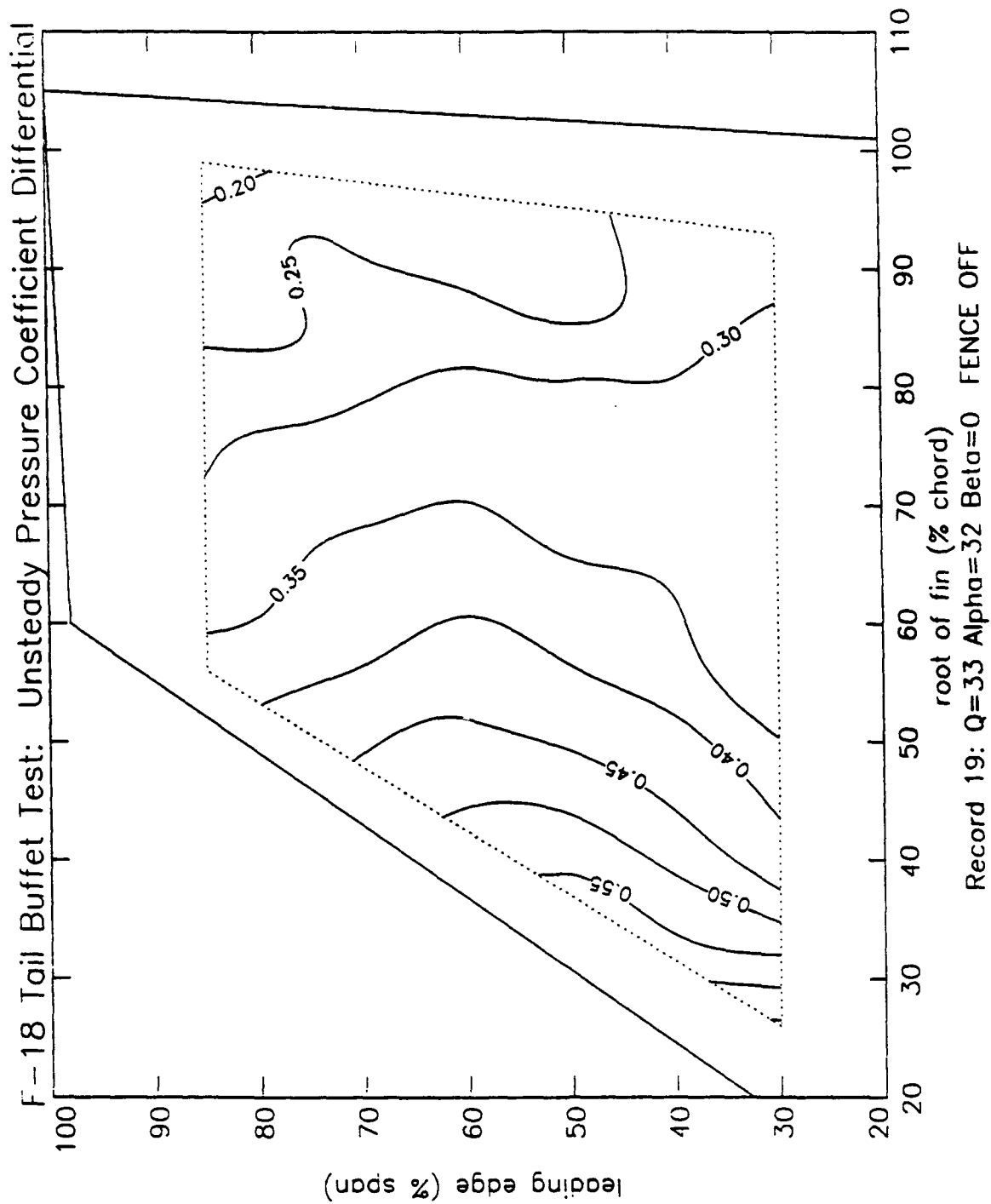


Figure 25A. RMS Pressure Differential Contour Plot for angle of attack of 32 degrees, Fence Off

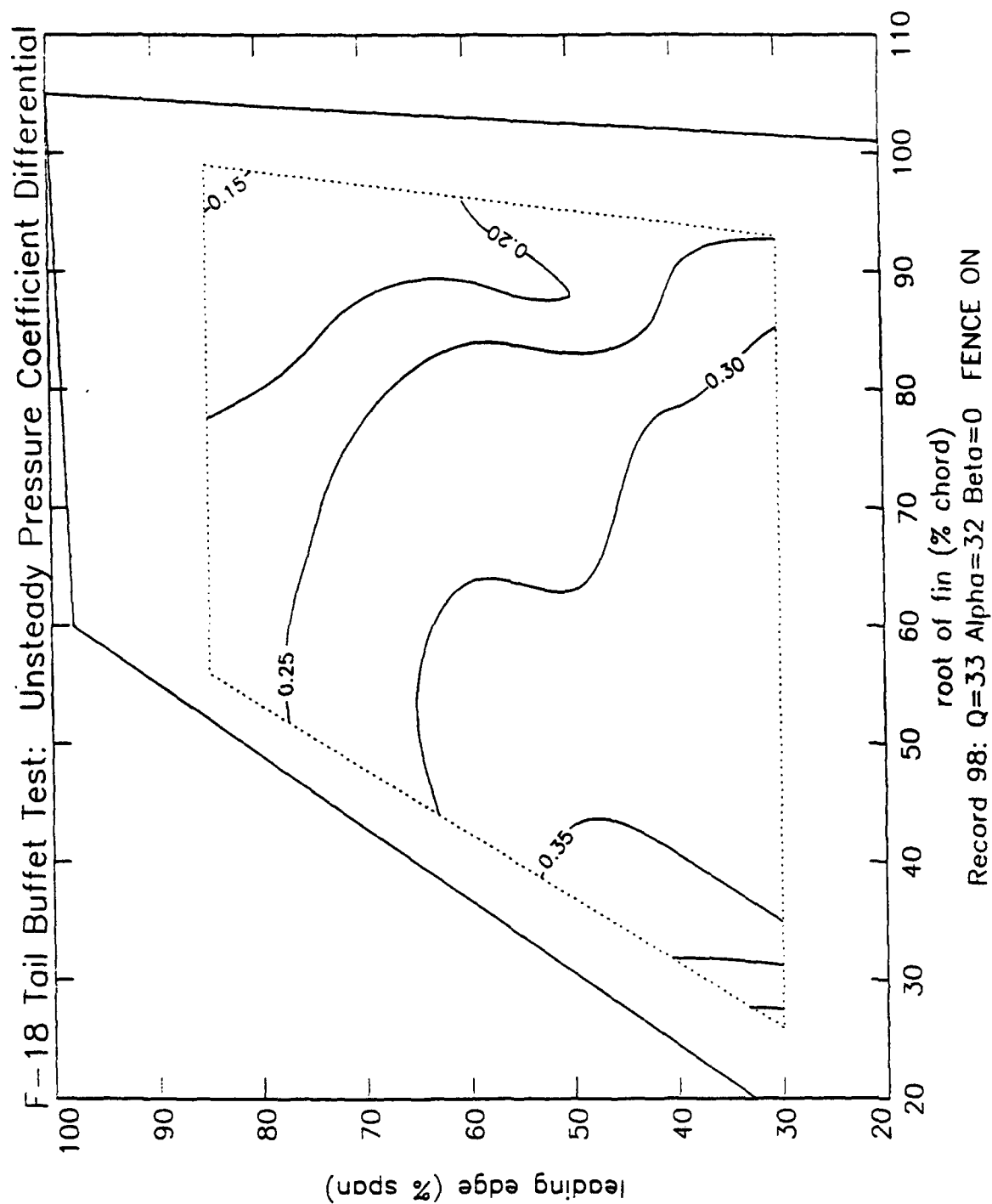


Figure 25B. RMS Pressure Differential Contour Plot for angle of attack of 32 degrees, Fence On

smooth with mild gradients, but the fence-on results at $\alpha = 20^\circ, \beta = 0^\circ$ and the test conditions with extremely negative sideslip do not conform to this trend. The former case is particularly interesting since the peak in the RMS buffet pressure near the tip of the fin is highly localized. No concrete evidence is available from the current test to verify or account for this result. Buffet data for $\alpha < 20^\circ$ would be required to define the character of the RMS pressure distribution in this angle-of-attack range.

Unsteady Pressures—Power Spectral Densities

Power spectral densities (PSDs) of the thirty-six (36) unsteady pressure differentials for each of the test cases were computed from the digitized signals as described in Section IV. The PSDs in this report are presented in both dimensional and nondimensional forms. The nondimensional form of the pressure PSDs is suggested by Mabey (1987). This nondimensional form of the buffet excitation spectra is expressed in terms of the freestream dynamic pressure:

$$\left(\frac{p'}{q_\infty}\right)^2 = \int_{n=0}^{\infty} F(n)dn = \int_{\ln n=-\infty}^{\ln n=+\infty} nF(n)d(\ln n)$$

where p' is the root-mean-square of the random pressure fluctuations measured by a given transducer, $n = f\bar{c}/U_\infty$ is the reduced frequency at which the pressure fluctuates, and $F(n)$ is the nondimensional PSD of the measured pressure fluctuations. When a dimensional pressure power spectral density, $P(f)$, is given, then $F(n)$ is determined from

$$F(n) = (P(f)/q_\infty^2) \cdot (U_\infty/\bar{c}).$$

Plots involving this nondimensional spectrum are presented with respect to nondimensional frequency. The above form shows $F(n)$ to be the PSD of the unsteady pressure coefficient divided by the characteristic time scale, \bar{c}/U_∞ .

The definition of the nondimensional buffet spectra may be interpreted in terms of dimensional analysis. Specifically, when the dimensional PSD is presented with dimensions psi^2/Hz , division by the square of the dynamic pressure removes the psi^2 units. Similarly, multiplication by (U_∞/\bar{c}) cancels the Hz unit and nondimensionalizes the PSD. An equivalent

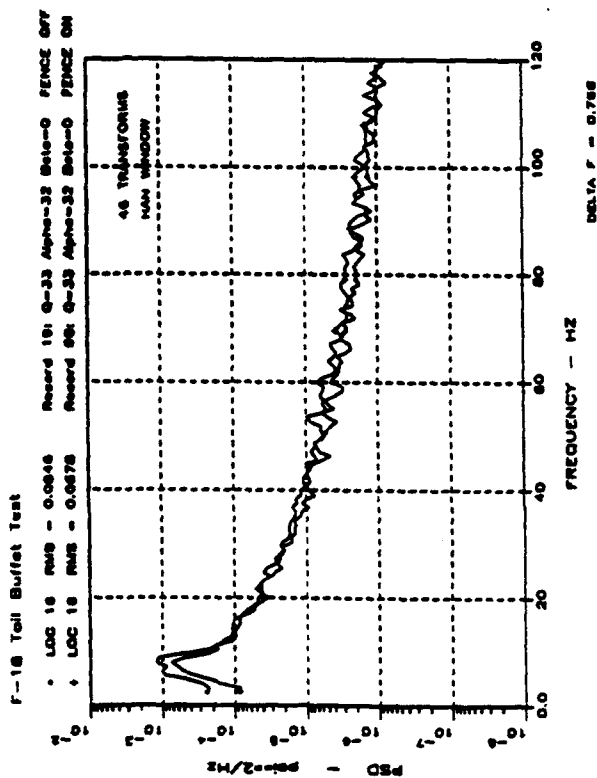
form of the nondimensional spectrum is used by Zimmerman and Ferman (1987), but their notation differs slightly. Mabey (1987) recommends plotting the buffet pressure spectra as $\sqrt{nF(n)}$ vs. n , and plots in this report follow this convention.

Pressure differential PSDs are presented for the $\alpha = 32^\circ$, $\beta = 0^\circ$ test case for both the LEX fence-off and -on conditions in Figures 26 and 27. Figures 26A and 26B show the dimensional and normalized PSDs, respectively, for the 60% span, 45% chord fin station consisting of transducers 16 and 57. Figures 27A and 27B show similar power spectra for station 18-55 at 60% span, 10% chord. Pressure differential PSDs for all transducer-pair stations and test conditions are presented in Volume III of this test report.

In Figures 26 and 27, the fence-off and -on traces are similar over the plotted spectrum; however, the fence-on curves in Figures 26A and 27A contain slightly less energy, especially in the lower frequencies. This result demonstrates the reduction due to the LEX fence in the buffet imposed on the vertical fin. Lower angles-of-attack, such as 20° , resulted in more significant reductions of the buffet excitation by the LEX fence. Figures 28 and 29 highlight this result by showing these PSDs for the same transducers as Figures 26 and 27. The LEX fence clearly is more effective at reducing fin buffet in the lower end of the angle-of-attack regime explored during these tests.

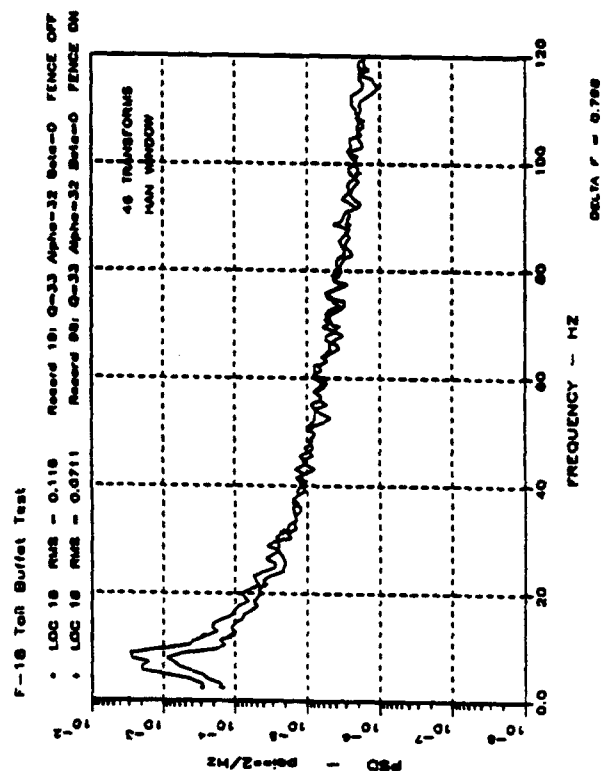
Comparison of the pressure PSDs from the two test cases portrayed in Figures 26 through 29 reveals some important trends. At $\alpha = 20^\circ$, the peaks are more broad-band than in the $\alpha = 32^\circ$ results. At higher angles-of-attack, the sharp drop in buffet energy levels away from the spectral peaks illustrates the importance of the leading-edge extension as a characteristic length scale in F/A-18 tail buffet. The importance of the LEX length scale is further evident in the distinct shift in the peak buffet power levels toward the lower end of the spectrum at higher angles-of-attack. This trend is common in high angle-of-attack tail buffet studies and has been noted on models of various scales by several researchers, including Zimmerman and Ferman (1987), Bean and Wood (1993), Washburn, et al. (1993), and Meyn and James (1993).

Figures 26 and 27 also demonstrate that for depicted transducer stations, the LEX fence had little effect on the frequency of peak excitation. The data presented in Volume III for the other transducer stations indicate that this observation applies over the entire fin surface at



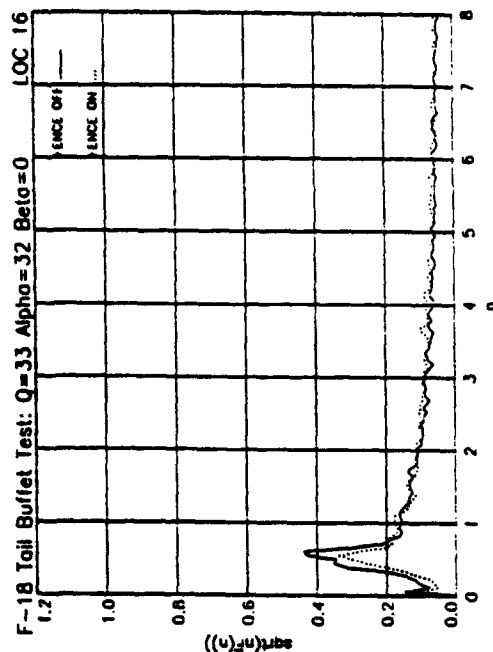
(A) Dimensional

Figure 26. Unsteady Pressure Differential Power Spectral Density for angle of attack of 32 degrees
Station 16-57

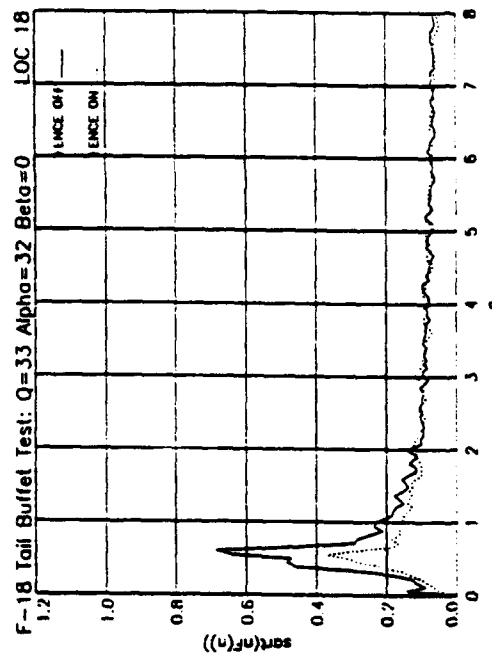


(A) Dimensional

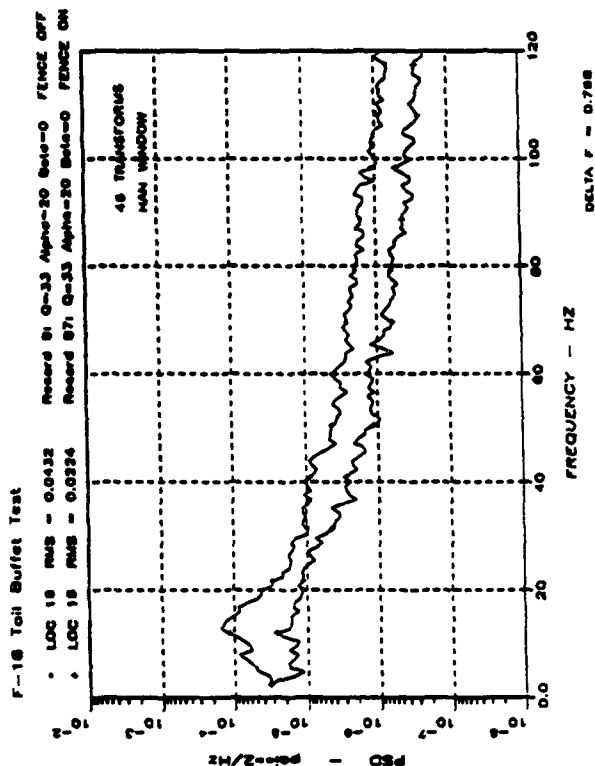
Figure 27. Unsteady Pressure Differential Power Spectral Density for angle of attack of 32 degrees
Station 18-55



(B) Nondimensional

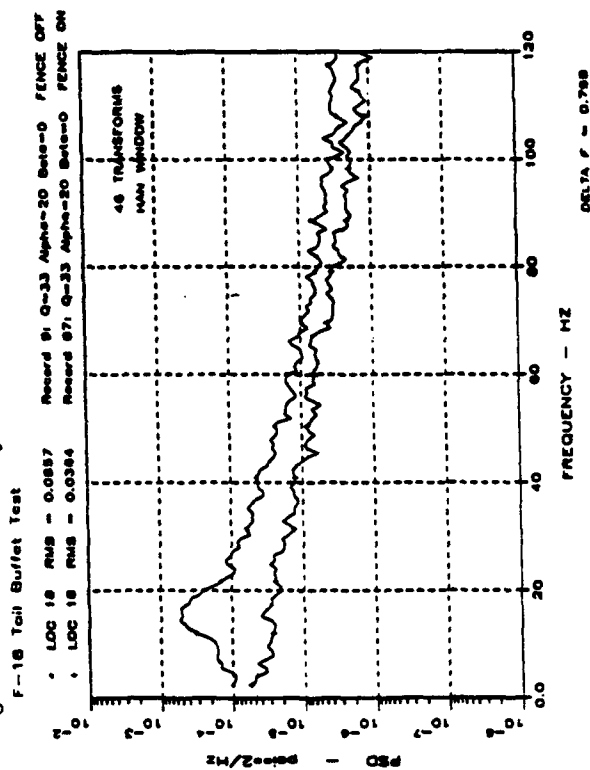


(B) Nondimensional



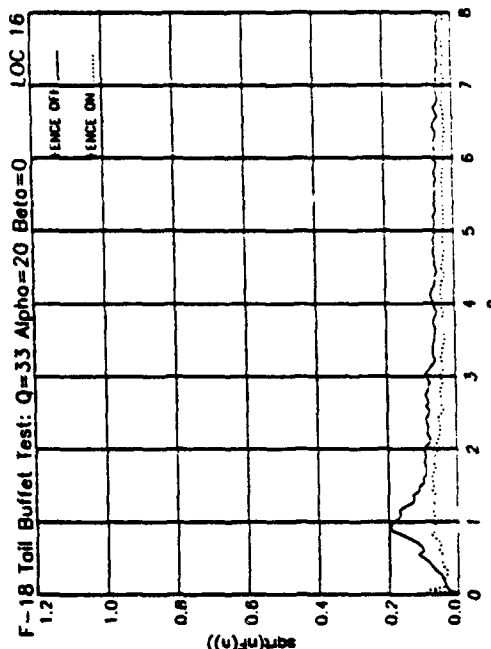
(A) Dimensional

Figure 28. Unsteady Pressure Differential Power Spectral Density for angle of attack of degrees, Station 16-57

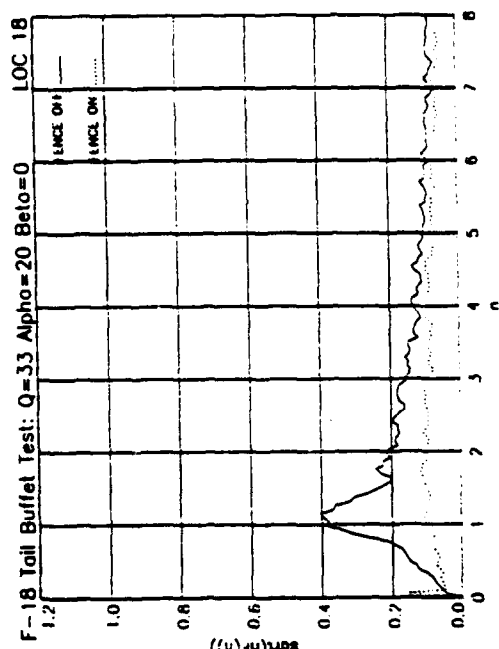


(A) Dimensional

Figure 29. Unsteady Pressure Differential Power Spectral Density for angle of attack of degrees, Station 18-55



(B) Nondimensional



(B) Nondimensional

$\alpha = 32^\circ$. Figures 28 and 29 show that a similar conclusion for the $\alpha = 20^\circ$ results would be rather tenuous since the peaks are not well defined. The peak frequency at the higher angles-of-attack is most likely controlled by the characteristic dimensions of the LEX itself, whereas other length scales, such as the LEX fence, may become important at the lower angles-of-attack.

Mabey (1987) defines *buffet* as the aerodynamic excitation provided by a separated flow, such excitation being independent of any structural motion. Mabey (1993) further suggests that a buffet pressure PSD should not contain "motion-induced pressures," which are those pressure fluctuations that may be attributed to the motion of the structure. These motion-dependent pressures may appear in two forms: pressure fluctuations that directly correlate with the motion of the vertical fin and increase aerodynamic damping, and alterations to the aerodynamic excitation from upstream flow separation. The latter of these two effects is particularly difficult to characterize. When present, these motion-induced pressures may be detected as localized peaks near the natural frequencies of the starboard vertical fin listed in Table 1*. A visual survey of the pressure PSDs in Volume III of this report indicated that the influence of structural motion on the recorded pressures was small.

The key point in the above definition of buffet is the distinction between the aerodynamic pressures which initiate the fin excitation and the motion-induced pressures resulting from the fin response. However, cross-correlation of the fin motion and a given pressure signal cannot, in general, provide a satisfactory means for separating the motion-dependent pressures from the aerodynamic excitation. Jones (1973) has discussed this issue at great length, and has described possible approaches for accomplishing this separation. Coe and Cunningham (1987) have applied empirical corrections to integrated aerodynamic force spectra to remove the effects of structural motion. Other researchers, including Zimmerman and Ferman (1987), Lee et al. (1990), and Meyn and James (1993), have not attempted to remove the motion-dependent pressures.

A universal method could not be identified or located to remove motion-induced pressures from the measured signals in a efficient, systematic fashion. Therefore, no attempt was made to extract motion-induced pressures from the results of this test.

* This observation assumes implicitly that the buffet pressures and the fin motion are not correlated.

Unsteady Pressures—Cross Spectral Densities

Cross spectral densities (CSDs) are required to accurately quantify the statistics of the buffet excitation imposed on the vertical fins at high angles-of-attack by the turbulent, vortical flow in which they are immersed. The computation and presentation of every CSD involving the seventy-two (72) pressure transducers would be prohibitive due to the enormous volume of data involved in the required calculations. This is partially overcome in the current report by examining the CSDs from selected transducer combinations and test cases that illustrate important aspects of the tail buffet phenomenon.

Volume IV of this report contains complete sets of differential pressure coefficient CSDs for the $\alpha = 32^\circ$ and $\alpha = 20^\circ$ test conditions at zero sideslip. These CSD plots depict the coherence and phase angle relationships between the buffet differential pressures acting at any two of the thirty-six transducer pair stations on the fin's surface, and are represented symbolically by $CSD(\Delta p_m, \Delta p_n)$. Volume IV also presents CSDs of the inside and outside buffet pressures at selected fin stations, $CSD[(p_{inside}, p_{outside})_j]$. These CSDs are presented for the $\alpha = 32^\circ$ and $\alpha = 20^\circ$ test conditions at zero sideslip. The transducer stations selected for presentation consist of those along the 25% chord and 75% span lines shown in Figure 15.

All CSDs generated from the F/A-18 buffet test data are presented in this report in terms of the corresponding coherence functions and phase angles. Unlike the power spectral densities discussed in the previous section, the coherence and phase are, by definition, dimensionless. Bendat and Piersol (1986) thoroughly discuss all aspects of spectral density functions and their use in describing random processes.

Unsteady Aerodynamic Loads—Root-Mean-Square Fluctuations

Computation of the unsteady normal force and bending moment on the starboard vertical fin at each angle-of-attack and sideslip angle was performed using the same area elements described earlier in this section. The time history of the unsteady normal force coefficient for

each test condition was determined by summing the force contributions from each area element at each time step using the relation

$$C_N(t) = \frac{1}{q_\infty A_F} \sum_{j=1}^{36} \Delta p_j(t) A_j.$$

Similarly, the unsteady root bending moment coefficient was calculated according to

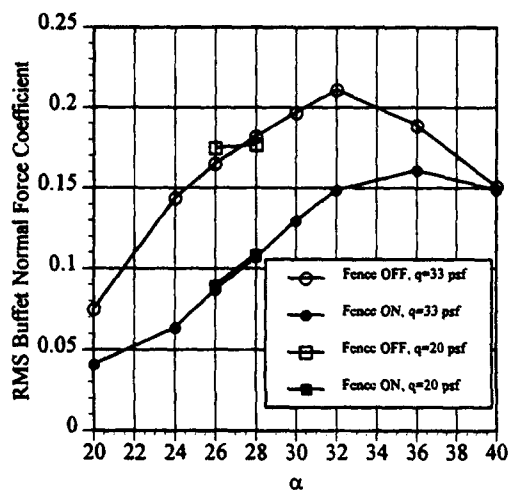
$$C_{M_B}(t) = \frac{1}{q_\infty A_F \bar{c}} \sum_{j=1}^{36} \Delta p_j(t) A_j \bar{y}_j.$$

Root-mean-square values of the buffet normal force and root bending moment coefficients for each angle-of-attack are denoted by $C_{N'}$ and $C_{M'_B}$, respectively. The RMS values of the unsteady loads cannot be computed properly by simply summing the RMS pressure differentials over the fin surface, as such a calculation would assume that the fluctuating pressures were completely uncorrelated between the various area elements.

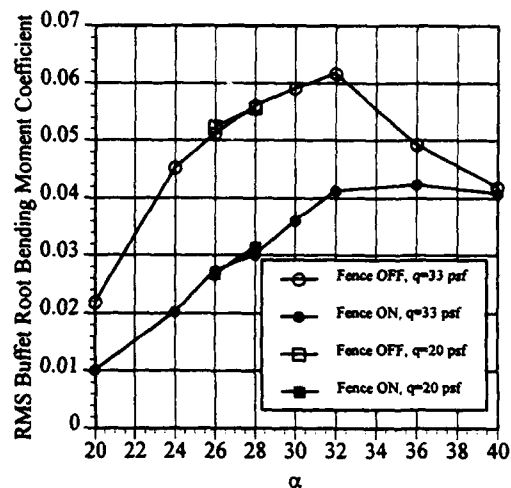
Figures 30A and 30B, which include LEX fence effects, depict the variation of the RMS normal force and root bending moment coefficients, respectively, versus angle-of-attack at zero sideslip for $q_\infty = 33 \text{ psf}$. The LEX fence produced a considerable decrease in the RMS load fluctuations up to 36 degrees angle-of-attack, with the two curves in each figure finally converging at $\alpha = 40^\circ$. $C_{N'}$ and $C_{M'_B}$ were reduced by a factor of one-half or better from $\alpha = 20^\circ$ to 26° when the LEX fence was deployed.

Dynamic pressure scale effects are also depicted in Figures 30A and 30B, where $q_\infty = 20 \text{ psf}$ results at 26 and 28 degrees angle-of-attack are overlayed on the primary data from the $q_\infty = 33 \text{ psf}$ test conditions. The RMS load coefficients agree quite well at these angles-of-attack, which implies that the pressures used to calculate the time histories of the normal force and root bending moment are accurately scaled by the dynamic pressure in the freestream.

Figures 31A through 31D show the relationship of RMS normal force and bending moment to sideslip. Specifically, Figures 31A and 31B illustrate the variation of $C_{N'}$ and $C_{M'_B}$ with sideslip at $\alpha = 30^\circ$, and Figures 31C and 31D do the same for $\alpha = 35^\circ$. The LEX fence

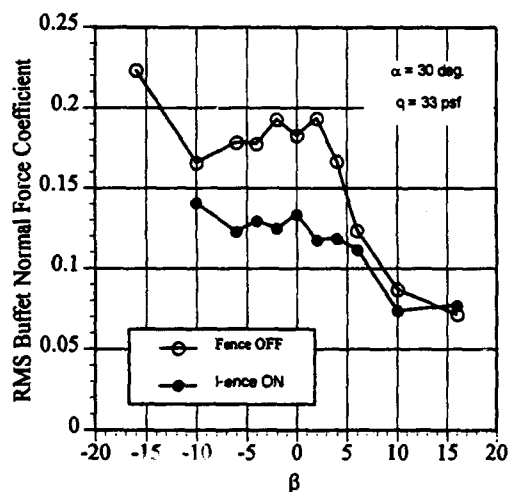


(A) RMS Normal Force Coeff.

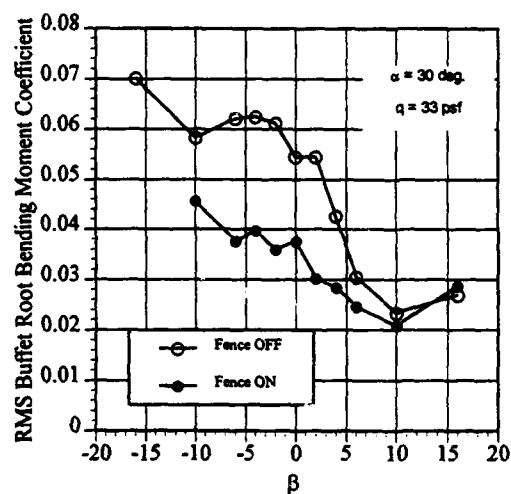


(B) RMS Bending Moment Coeff.

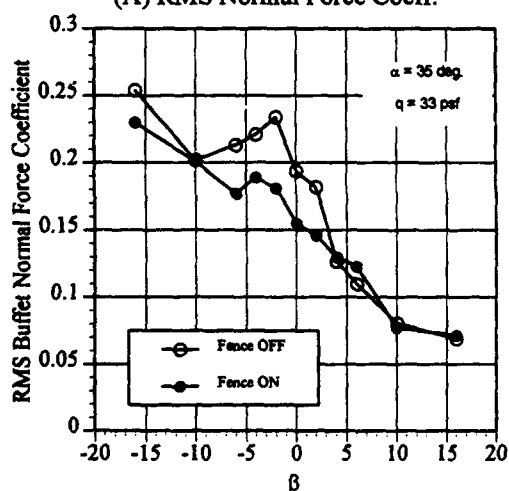
Figure 30. Root-Mean-Square Normal Force and Root Bending Moment Coefficients versus Angle-of-Attack at Zero Sideslip.



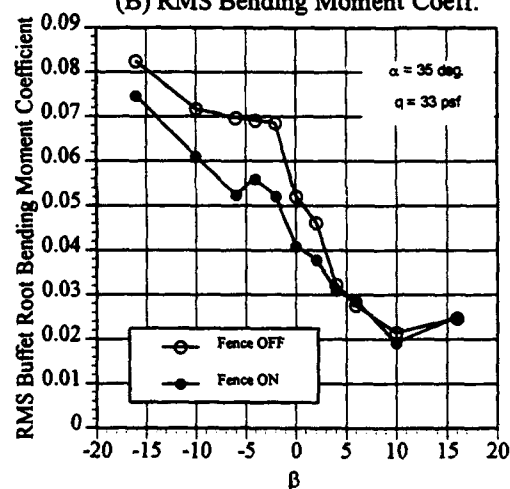
(A) RMS Normal Force Coeff.



(B) RMS Bending Moment Coeff.



(C) RMS Normal Force Coeff.



(D) RMS Bending Moment Coeff.

Figure 31. Root-Mean-Square Normal Force and Root Bending Moment Coefficients versus Sideslip.

continued to reduce the buffet loads in both positive and negative sideslip conditions, although some efficacy was lost at $\alpha = 35^\circ$.

Unsteady Aerodynamic Loads—Power Spectral Densities

Power spectral densities of the unsteady normal force and root bending moment coefficients were determined using the time histories discussed in the previous section. The PSDs of $C_N(t)$ and $C_{M_B}(t)$ are denoted symbolically by $C_{N''}$ and $C_{M_B''}$, respectively. Plots of the normal force and bending moment coefficient PSDs versus nondimensional frequency from each test condition, including LEX fence effects, are provided in Appendix I of this volume. Since the normal force and bending moment coefficients are dimensionless by definition, calculation of their PSDs would usually yield quantities with dimensions of Hz^{-1} . Hence, the normal force and bending moment coefficient PSDs were made completely dimensionless through multiplying them by U_∞/\bar{c} , which is the inverse of the characteristic time scale discussed with regard to the PSDs of the differential pressures. The PSD of the bending moment coefficient is then expressed symbolically by the equation,

$$C_{M_B''} = \left\{ PSD \left[\frac{M_B}{q_\infty A_F \bar{c}} \right] \right\} \cdot \left[\frac{U_\infty}{\bar{c}} \right]$$

The bending moment PSDs in this report conform with this format. The normal force coefficient PSD were calculated similarly, with $C_{M_B''}$ and (M_B/\bar{c}) replaced by $C_{N''}$ and N , respectively.

Figures 32 through 34 contain samples of the root bending moment PSDs at angles-of-attack of 20, 32, and 40 degrees. These figures show the LEX fence to be an effective means of reducing the buffet loads on the vertical tail up to approximately $\alpha = 32^\circ$. Higher angles-of-attack were found to drastically reduce the efficacy of the LEX fence. At $\alpha = 40^\circ$ in Figure 34, little difference exists between the LEX fence-off and -on curves. Also evident in Figures 32 through 34 is the distinct decrease in the frequency of the peak bending moment excitation as the angle-of-attack increased. This trend is a direct result of the corresponding frequency shift discussed earlier in this Section for the buffet pressures.

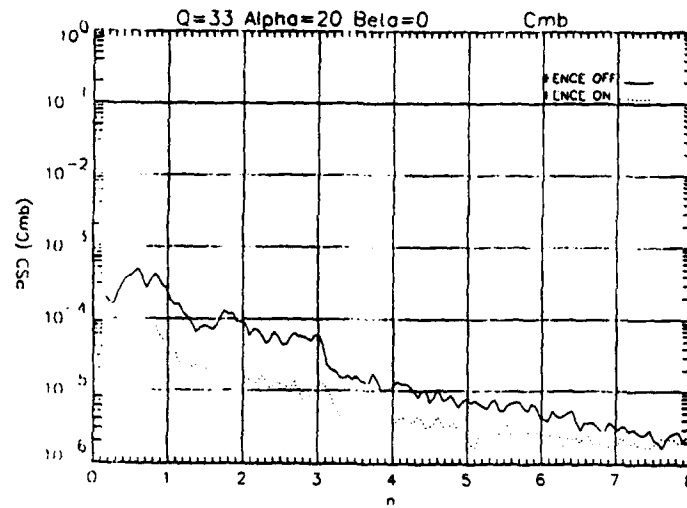


Figure 32. RMS Root Bending Moment Power Spectral Density, AoA = 20 degrees

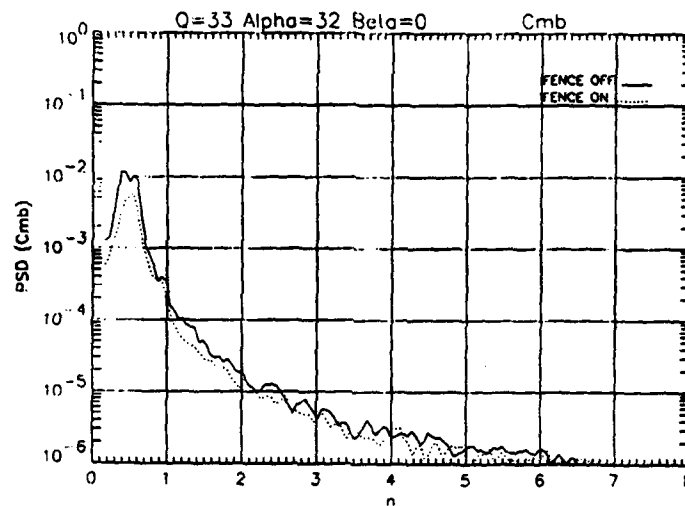


Figure 33. RMS Root Bending Moment Power Spectral Density, AoA = 32 degrees

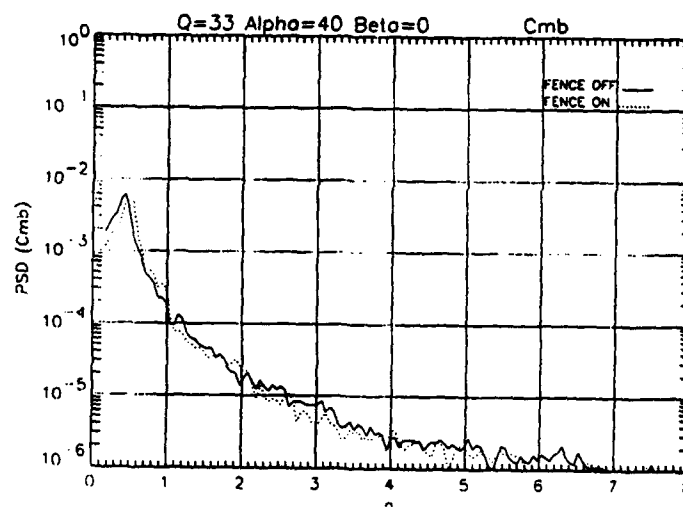


Figure 34. RMS Root Bending Moment Power Spectral Density, AoA = 40 degrees

The primary effect of sideslip variation from $\beta = -4^\circ$ to $+4^\circ$ was a general decrease in the levels of buffet excitation. A slight decrease in the frequency of peak excitation was also noted over this range of sideslip angles. Sideslip variation was also found to reduce the performance of the LEX fence at both 30 and 35 degrees angle-of-attack, but the resulting effects were not so strong as those due to angle-of-attack changes.

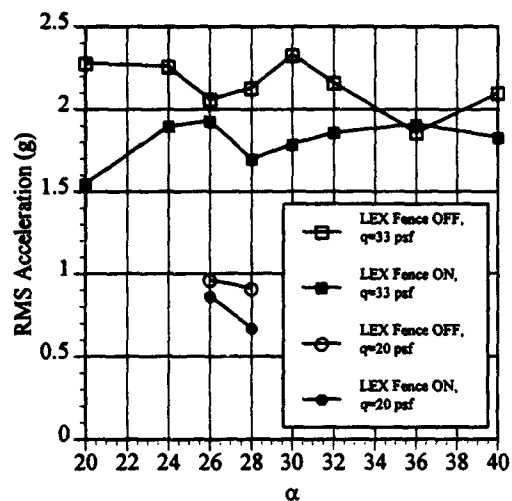
Fin-Tip Accelerations—Root-Mean-Square Values

Two accelerometers, one near the leading edge and one near the trailing edge, were installed near the tip of each vertical fin to sense the buffeting. Each accelerometer measured the local acceleration due to buffet, $\ddot{z}(t)$, at its location. The resulting signals were normalized by the standard acceleration due to gravity at the earth's surface, $g = 9.81 \text{ m/s}^2 = 386 \text{ in/s}^2$, to obtain the fin-tip accelerations for a given test condition, $\ddot{z}(t)$, expressed as "g's." Root-mean-square (RMS) values of these accelerations are denoted by \ddot{z}' . The starboard leading and trailing edge accelerometers are referred to as "S1" and "S2." Similarly, the port leading and trailing edge accelerometers are denoted by "P1" and "P2."

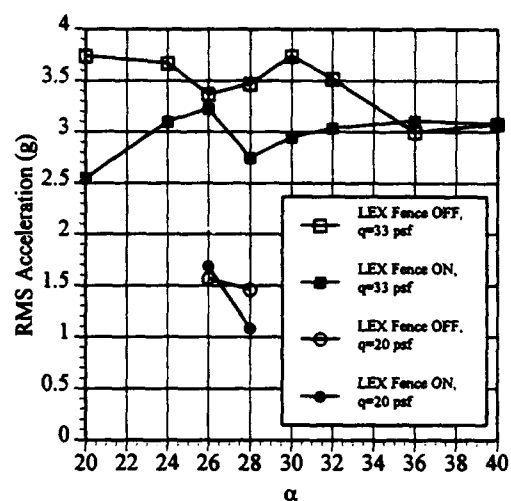
Figures 35A through 35D show the RMS normalized accelerations vs. angle-of-attack at zero sideslip from the starboard and port fins. The RMS normalized accelerations for the sideslip sweeps at $\alpha = 30^\circ$ and $\alpha = 35^\circ$ are presented in Figures 36A through 36D and Figures 37A through 37D, respectively. Figures 35A, 35B, 36A, 36B, 37A, and 37B correspond to the starboard fin leading-edge and trailing-edge accelerometers. Similarly, Figures 35C, 35D, 36C, 36D, 37C, and 37D depict results from the port fin leading-edge and trailing-edge accelerometers.

Fin-Tip Accelerations—Power Spectral Densities

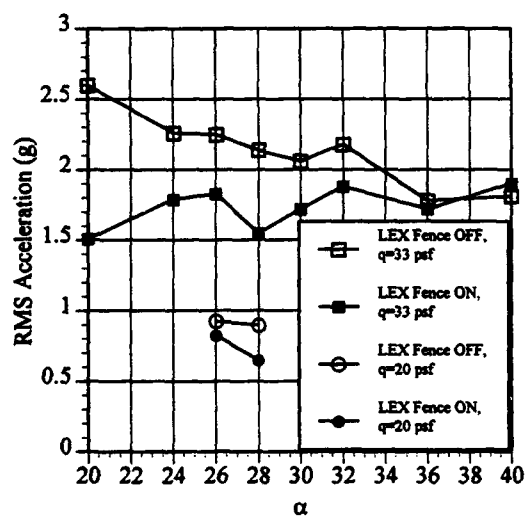
Power spectral densities of the four (4) accelerometer signals were computed for each test condition. The acceleration PSDs were calculated in nondimensional form, $Z(n)$, by first



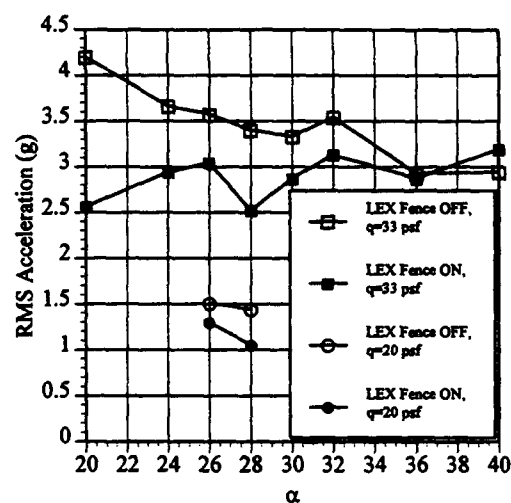
(A) Accelerometer P2



(B) Accelerometer P1

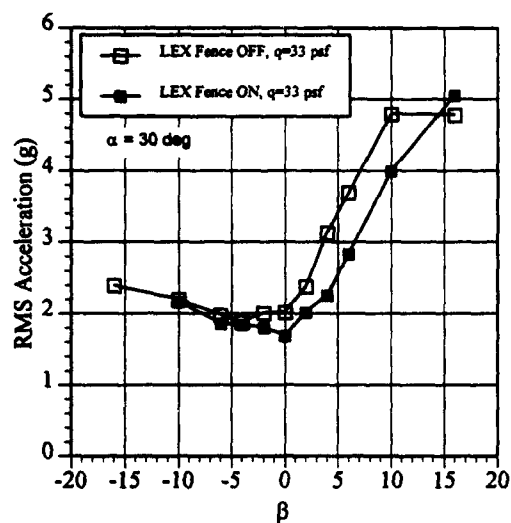


(C) Accelerometer S2

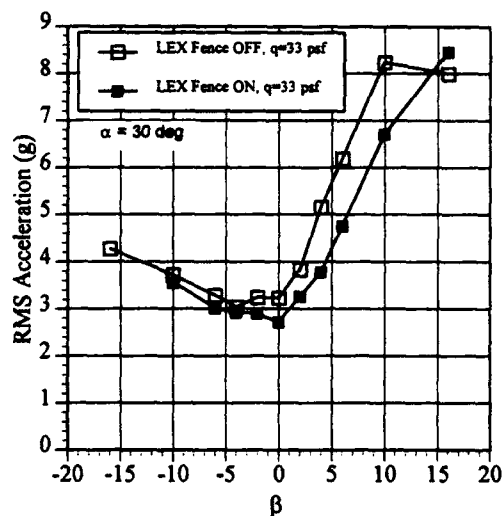


(D) Accelerometer S1

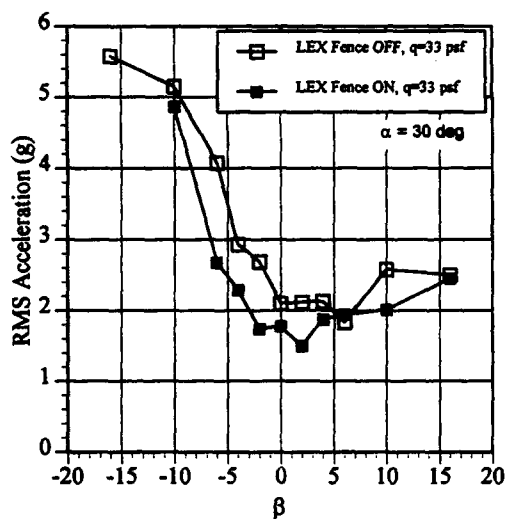
Figure 35. Root-Mean-Square Fin-Tip Accelerations versus Angle-of-Attack at Zero Sideslip



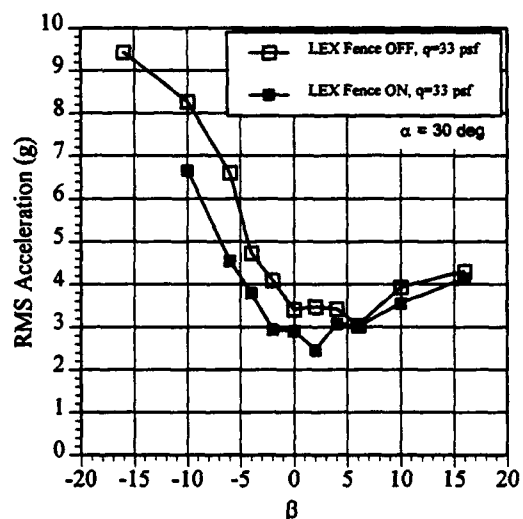
(A) Accelerometer P2



(B) Accelerometer P1

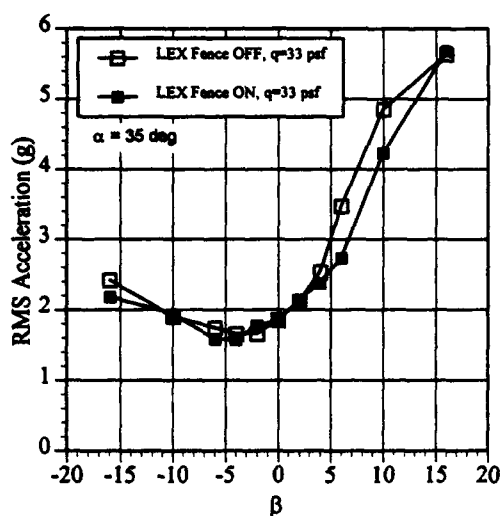


(C) Accelerometer S2

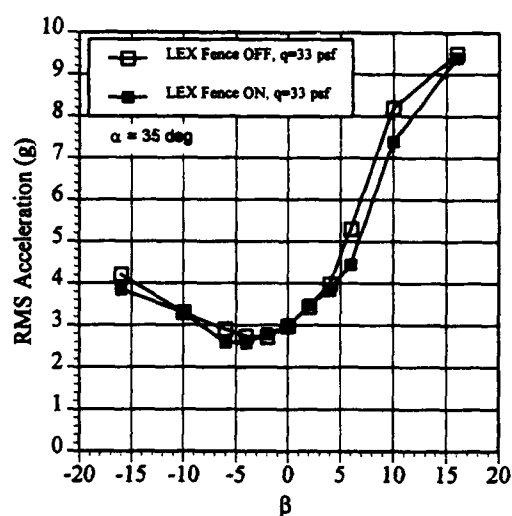


(D) Accelerometer S1

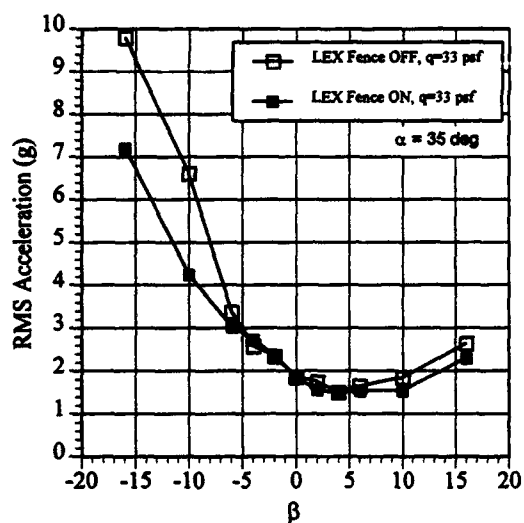
Figure 36. Root-Mean-Square Fin-Tip Accelerations versus Sideslip at 30 Degrees Angle-of-Attack



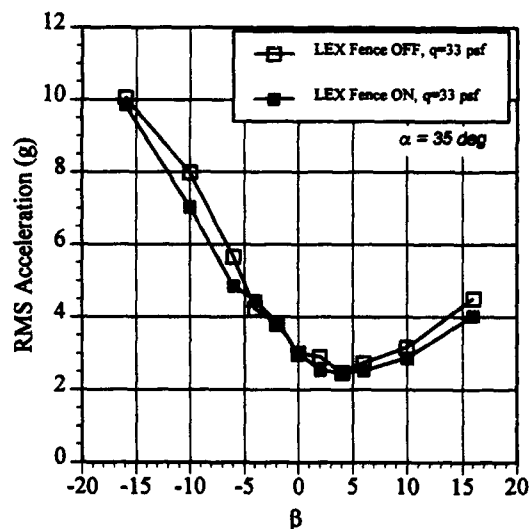
(A) Accelerometer P2



(B) Accelerometer P1



(C) Accelerometer S2



(D) Accelerometer S1

Figure 37. Root-Mean-Square Fin-Tip Accelerations versus Sideslip at 35 Degrees Angle-of-Attack

computing the dimensional PSD from each accelerometer as described in Section IV. Then the resulting spectra were scaled to yield $Z(n)$:

$$Z(n) = PSD(\ddot{z}) \cdot \left(\frac{U_\infty}{\bar{c}} \right),$$

where $\ddot{z}(t)$ is the dimensional acceleration and U_∞/\bar{c} is the inverse of the characteristic time scale described earlier in this section. This characteristic time scale was chosen simply to retain consistency with the pressure, normal force, and root bending moment PSDs calculated earlier. Its use does not imply that the response is properly scaled by a time constant, \bar{c}/U_∞ , that depends only aerodynamic parameters. A complete set of dimensional and nondimensional acceleration PSDs for the entire test matrix is included in Volume III of this report.

Figures 38A through 38D show the nondimensional response power spectra from each of the accelerometers for the severe buffet, $\alpha = 32^\circ, \beta = 0^\circ$ test condition discussed in previous sections. Each plot contains results from both the LEX fence-off and -on test conditions. Sharp peaks at 15 Hz and 45 Hz, corresponding to the first bending and torsion modes, are especially evident in Figure 38. *The sharpness of these peaks in the acceleration PSDs implies that the total damping in these modes was fairly small. The lack of a prominent peak near 61 Hz also indicates that the second bending mode did not play a prominent role in the buffet response at $q_\infty = 33 \text{ psf}$.*

Comparison of the acceleration PSDs in Figure 38 with the differential pressure coefficient PSDs in Figures 26 and 27 illustrates the character of the input/output relationship between the pressure and structural response. The vertical fins and the surrounding aircraft structure are seen to act collectively as a selective filter that allows response to certain portions of the imposed buffet spectra while suppressing response in other frequency bands.

The relative similarity between the PSDs from similarly located accelerometers on the two fins, as depicted in Figures 38A and 38C, suggests that the response and, hence, the excitation, was essentially symmetric as would be expected at zero sideslip. This is also reflected in the near equality of the RMS levels discussed in the previous section. However, some notable differences are readily observed in the spectra. The peak at 45 Hz is more narrow in the starboard fin spectra than in the port fin results, and the port-fin response in the range from 50 Hz

to 80 Hz is more broad-band than the starboard fin response. These results are due more likely to the slight structural differences between the two fins than to any asymmetries in the impinging flow.

Figures 39A through 39D show the nondimensional acceleration power spectra for the $\alpha = 20^\circ, \beta = 0^\circ$ test condition. As with the pressure PSDs, the ability of the LEX fence to reduce dynamic loads on the vertical fin is demonstrated in these plots. Reductions in the structural response are present throughout the plotted frequency spectrum for each accelerometer, indicating that the LEX fence was much more effective at $\alpha = 20^\circ$ than at $\alpha = 32^\circ$.

Another aspect of the response spectra illustrating the relative importance of the LEX fence in this flow regime is the effect that the LEX fence had on the response peak of the 1st torsion mode. Both S1 and S2 accelerometers' power spectra show a slight shift in the peak near 45 Hz when the fence was deployed. This increment in the torsional response frequency is not evident in the acceleration PSDs from the port fin. The minor structural differences between the two fins are probably responsible for this result, but aerodynamic damping or stiffness are other possible factors.

The differential pressure PSDs shown earlier exhibit a distinct shift in the peak power frequency of the aerodynamic excitation toward the lower end of the spectrum at higher angles-of-attack. This trend is also evident in the acceleration PSDs. At $\alpha = 20^\circ$, approximately the same amount of power is present in the response of the first two modes, whereas the first bending mode peak is significantly higher than the first torsion mode peak in the $\alpha = 32^\circ$ PSDs. Thus, the first bending and torsion modes participated equally in the buffet response at the low end of the angle-of-attack regime for this test. At higher angles-of-attack, the first bending mode dominated. The response PSDs in Volume III indicate that this dominance of the first bending mode continued until $\alpha = 40^\circ$, the highest angle-of-attack explored in the current tests.

Damping values, estimated using the "half-power point" method, were determined to establish the level of total damping present in both the starboard and port vertical fins' first bending modes for the $\alpha = 20^\circ$ and $\alpha = 32^\circ$, zero sideslip test conditions. Ratios of total damping, shown in Table 4, were obtained for the 1st bending mode using the S1 and P1 accelerometers' power spectral densities from the fence-off test conditions. One trend evident in

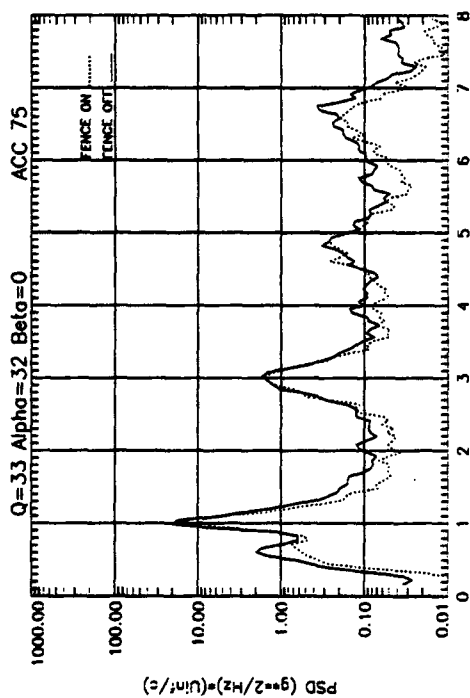


Figure 38A. Acceleration Power Spectral Density for Starboard Fin Accelerometer #2

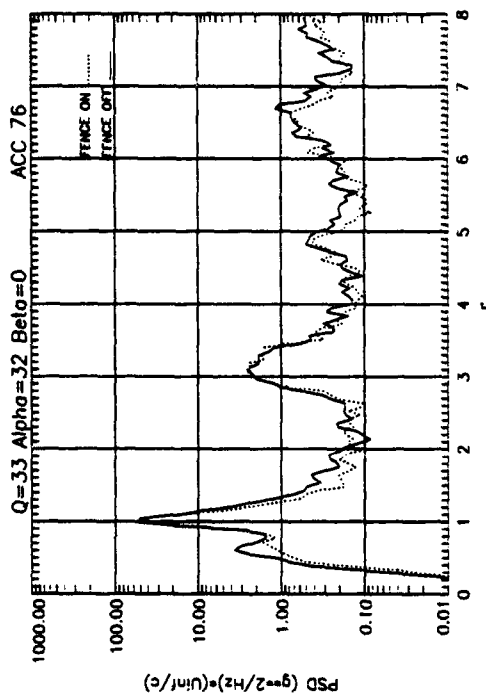


Figure 38B. Acceleration Power Spectral Density for Starboard Fin Accelerometer #1

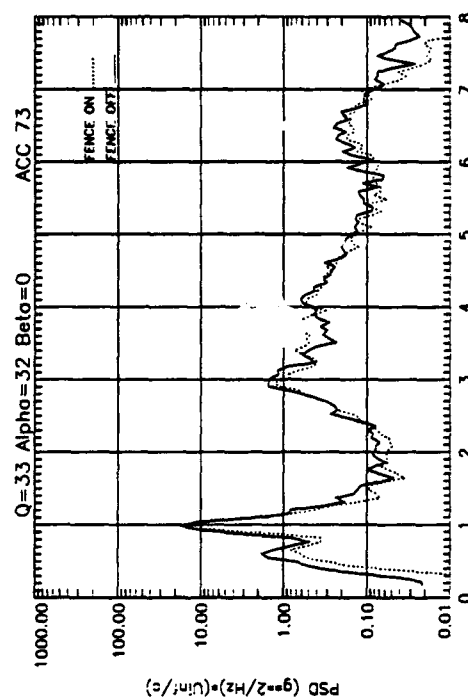


Figure 38C. Acceleration Power Spectral Density for Port Fin Accelerometer #2

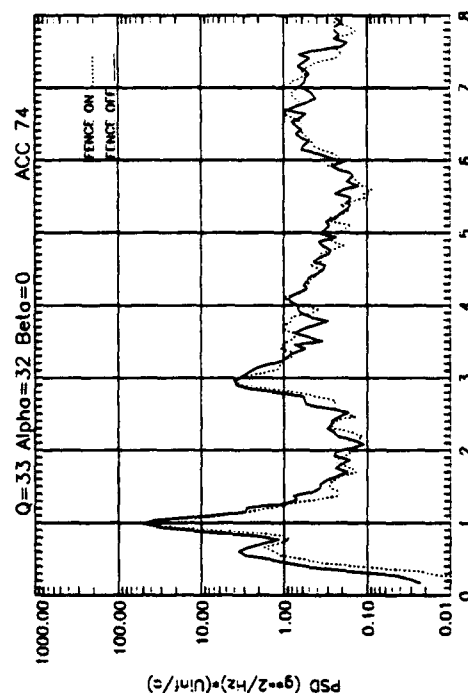


Figure 38D. Acceleration Power Spectral Density for Port Fin Accelerometer #1

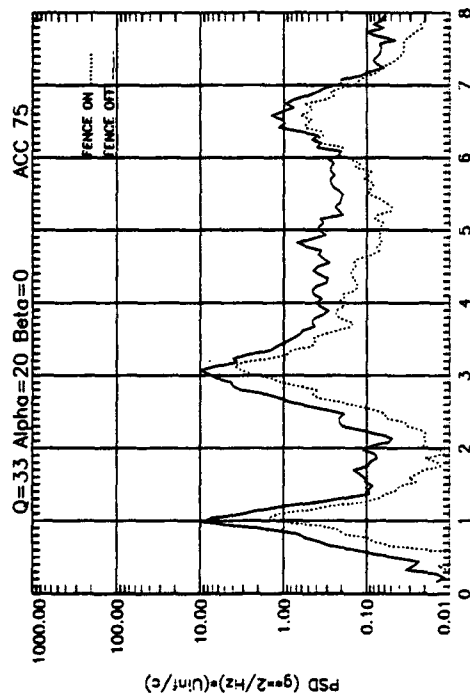


Figure 39A. Acceleration Power Spectral Density for Starboard Fin Accelerometer #2

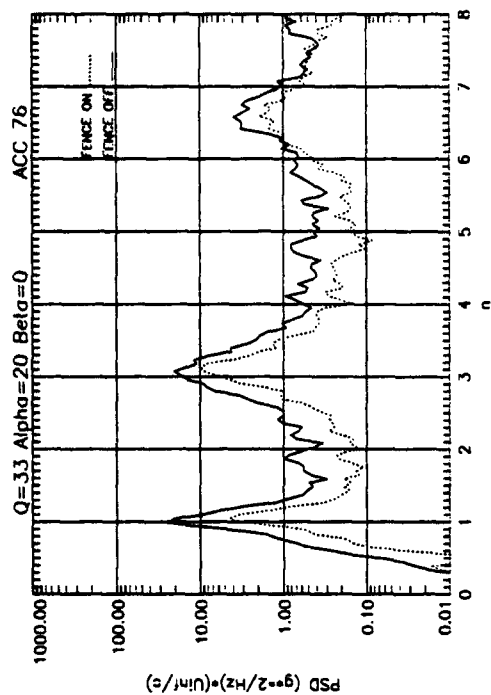


Figure 39B. Acceleration Power Spectral Density for Starboard Fin Accelerometer #1

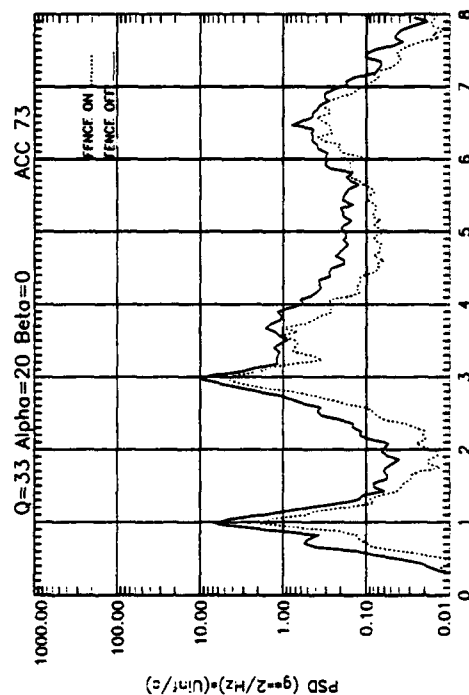


Figure 39C. Acceleration Power Spectral Density for Starboard Fin Accelerometer #2

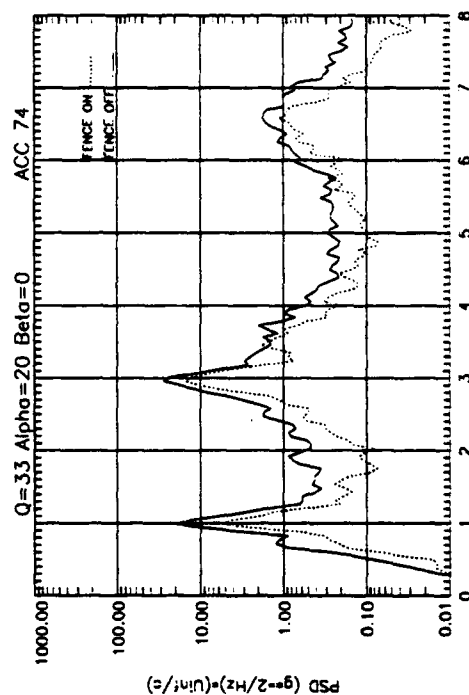


Figure 39D. Acceleration Power Spectral Density for Starboard Fin Accelerometer #1

Table 4 is that the total damping levels in the first mode varied only slightly with changes in angle-of-attack.

Table 4. Estimates of Total Damping Ratios for the Vertical Fins' 1st Bending Mode

Test Point	Accelerometer	1st Bending Mode Total Damping
$\alpha = 32^\circ, \beta = 0^\circ$	S1	0.066
	P1	0.070
$\alpha = 20^\circ, \beta = 0^\circ$	S1	0.069
	P1	0.069

Measured structural damping levels for the first bending mode, taken from the previous ground vibration tests, were between 1.5% and 4% of critical damping, depending on the angle-of-attack and whether the mode was symmetric or antisymmetric in character. Comparing these structural damping values with the total damping estimates in Table 4 indicates that aerodynamic damping was a significant factor in the buffeting dynamics of the vertical fins in the first bending mode.

The total damping values are considered estimates since the 0.8 Hz frequency resolution used in the acceleration PSDs introduced unavoidable shifts in the frequency values on which the half-power point depends. Precise comparisons between total damping and structural damping values are difficult since the damping results from the GVT data correspond to angles-of-attack other than the two wind-tunnel test conditions presented. However, the three angle-of-attack conditions where the aircraft fins were tested during the GVT, $\alpha = 16^\circ, 28.8^\circ$, and 45.5° , span a range greater than those tested in the wind tunnel, so qualitative conclusions drawn by comparing ranges of damping values are considered valid.

Total damping values for the 1st torsion mode were not determined from the wind-tunnel results because the corresponding peaks in the acceleration PSDs increased in bandwidth and decreased in response level for angles-of-attack greater than 24° . The combination of these response properties contradicts the assumption of small damping in the mode, and precludes accurate use of the half-power point method.

The rather low response in the first torsion mode does not correlate well with the extreme buffeting observed in flight at $q_\infty = 300$ to 400 psf. The disparity between the in-flight and

wind-tunnel response power spectra shows that the maximum dynamic pressure, 33 *psf*, available in the wind tunnel was too low to properly simulate the in-flight buffet power spectral content under extreme buffet conditions. Appendix II briefly discusses this issue.

Fin-Tip Accelerations—Cross Spectral Densities

Cross-spectral densities (CSDs), generated from the fin-tip acceleration responses to the buffet excitation, provide information on the statistical nature of the structural response to the imposed buffet excitation. The fin-tip acceleration CSDs were computed for the $\alpha = 32^\circ, \beta = 0^\circ$ and $\alpha = 20^\circ, \beta = 0^\circ$ test conditions with the LEX fence both off and on. Examination of these test conditions highlights the low and high ends of the buffet regime explored in these tests. Volume IV contains a complete set of acceleration CSDs from the two test conditions just cited. As with the pressure cross spectral densities, the acceleration CSDs are expressed in terms of coherence and phase functions.

Section VI

Conclusion

Detailed full-scale wind tunnel tests were conducted to quantify the buffet excitation and response of the F/A-18 vertical fins at high angles-of-attack under various sideslip conditions. Tests were performed both with and without the LEX fence to further define the character of the tail buffet phenomenon. The buffet pressures and dynamic response of the vertical fins were summarized using power and cross-spectral density functions, as well as root-mean-square values. Further understanding was achieved by integrating the pressure distributions from each test condition to approximate the unsteady normal forces and root bending moments acting on the vertical fin.

Under symmetric test conditions, the LEX fence reduced unsteady loads on the vertical fins up to $\alpha = 40^\circ$; however, its performance was decreased above $\alpha = 32^\circ$. Sideslip sweeps at $\alpha = 30^\circ$ and 35° caused smaller reduction in the efficacy of the LEX fence. The minor effects on the LEX fence's performance due to sideslip were related to the reduced ability of the LEX fence to reduce buffet loads at high angles-of-attack.

Increases in the aircraft's steady angle-of-attack focused the buffet excitation into an increasingly narrow frequency band. The frequency at which the peak buffet loads were recorded decreased at higher angles-of-attack. Changes in the sideslip orientation of the aircraft from negative to positive values resulted in decreases in the buffet excitation levels throughout the plotted frequency spectrum, but had only minimal effects on the shape of the spectral distribution and frequency of peak excitation.

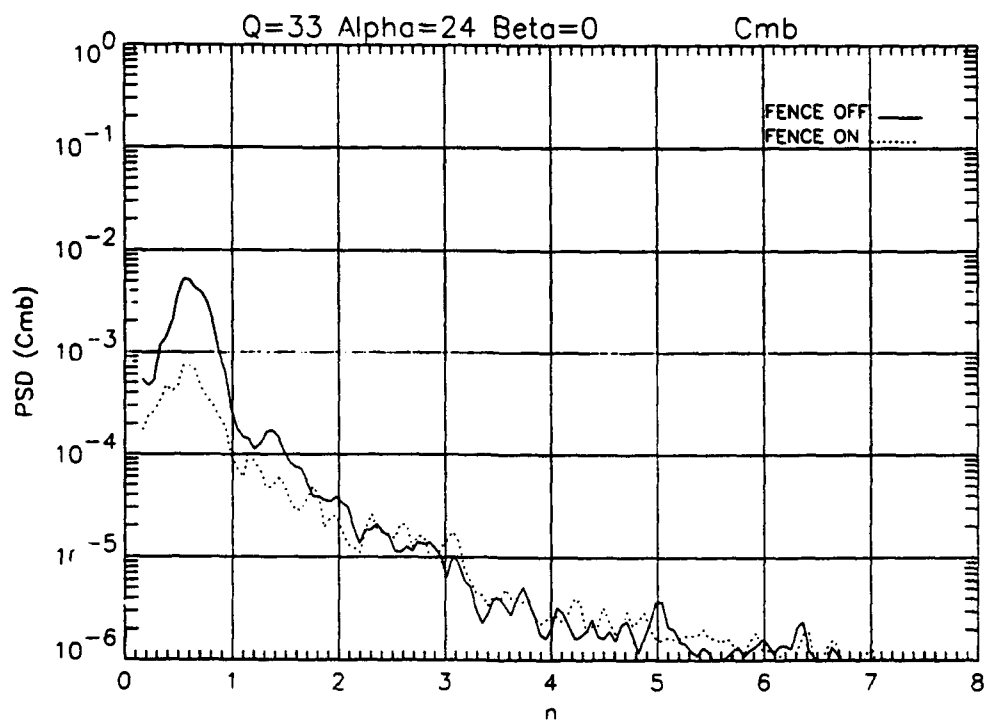
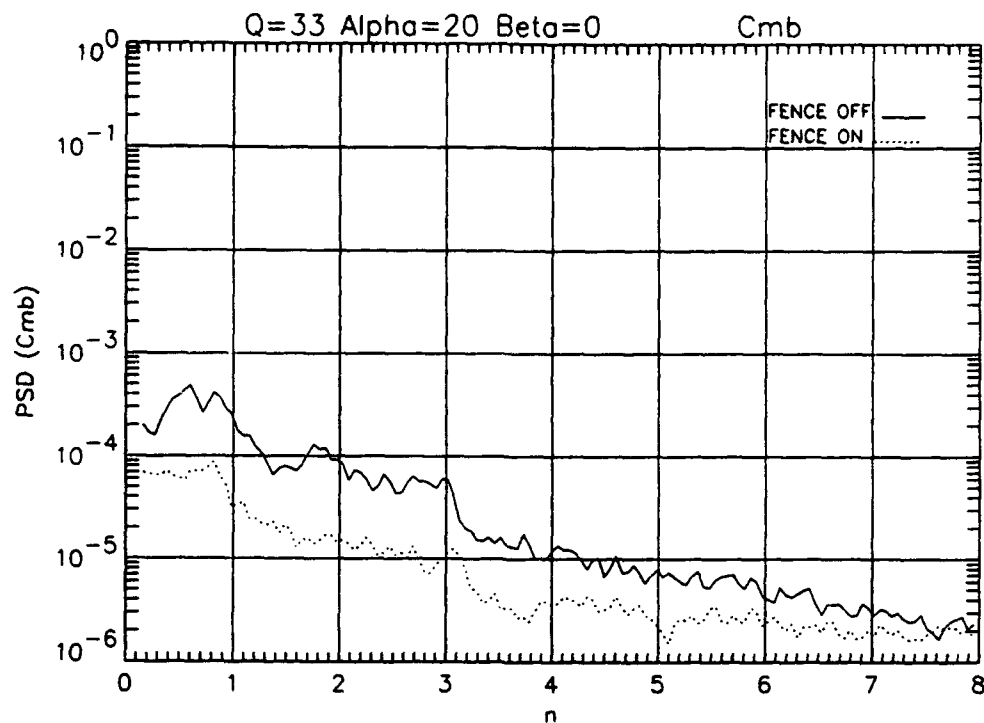
Power spectral densities of the fin-tip accelerations exhibited many properties similar to those of the pressure and load spectra. The LEX fence greatly reduced the peak response levels for angles-of-attack from 20 to 32 degrees, but almost no reduction was achieved at 40° . A shift in the peak response levels toward the lower end of the spectrum occurred at higher angles-of-attack. Thus, the first bending mode dominated the response for $\alpha \geq 24^\circ$. Aerodynamic damping was shown to be an important factor governing response in the first bending mode.

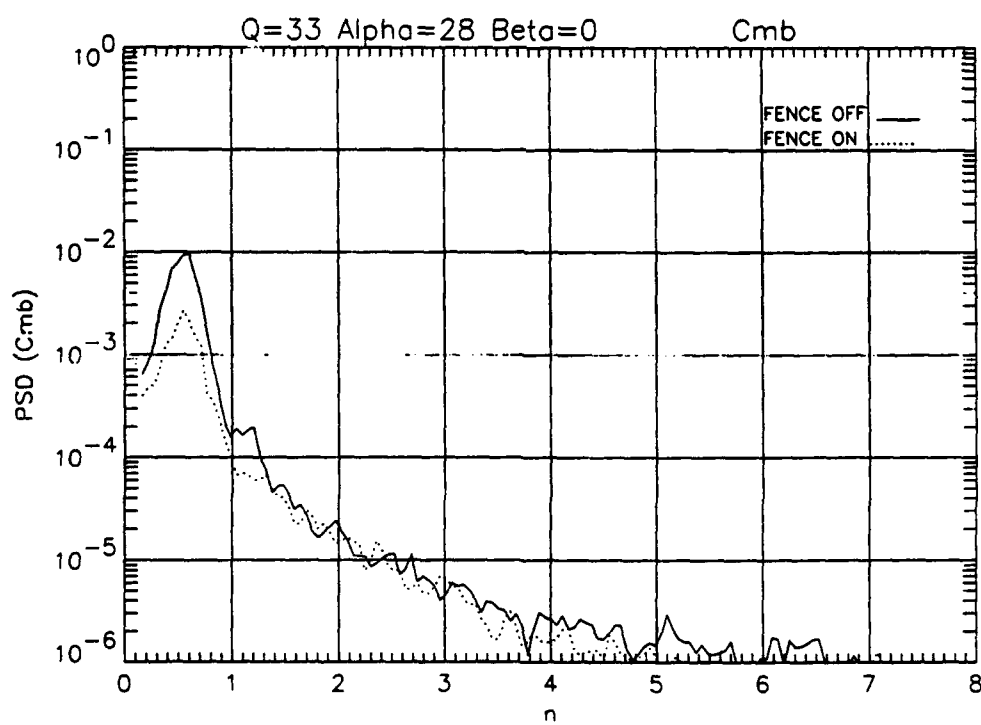
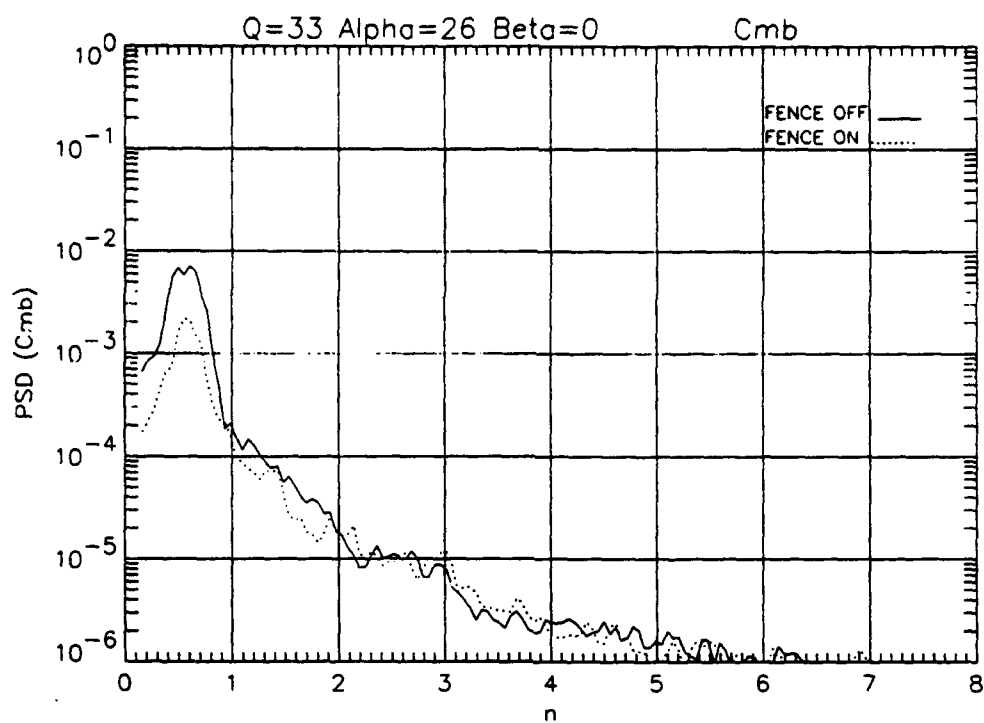
Section VII

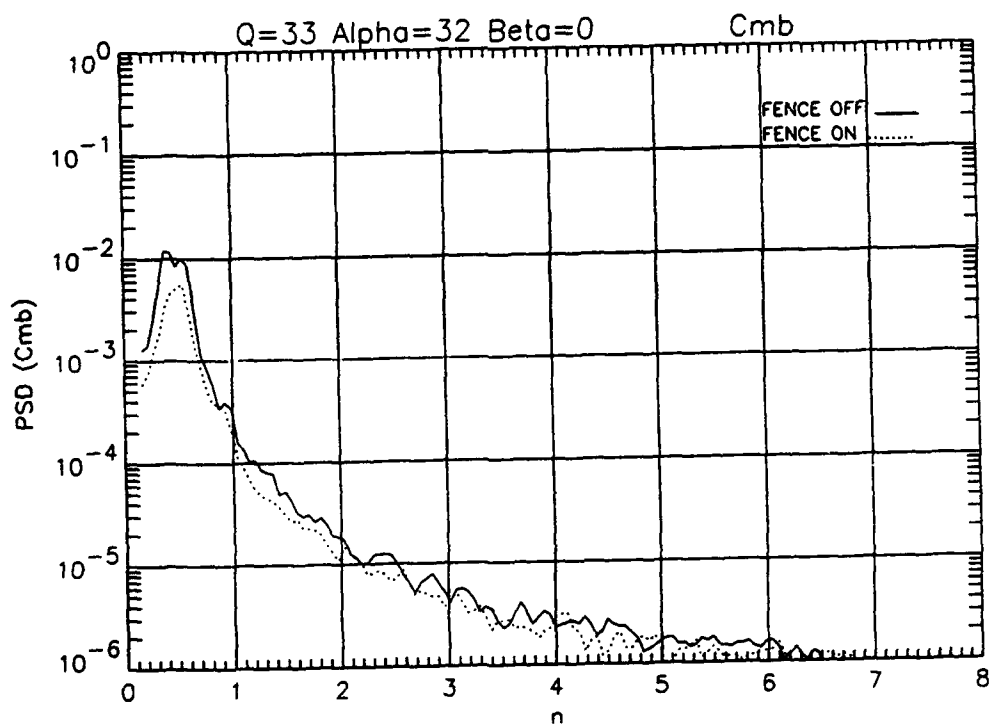
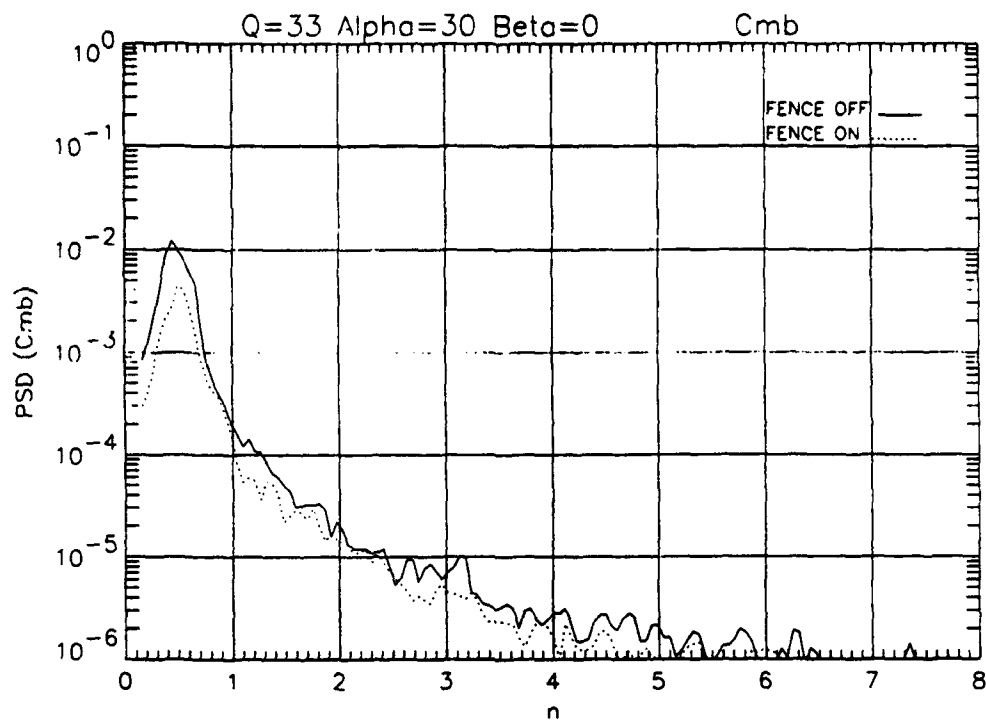
References

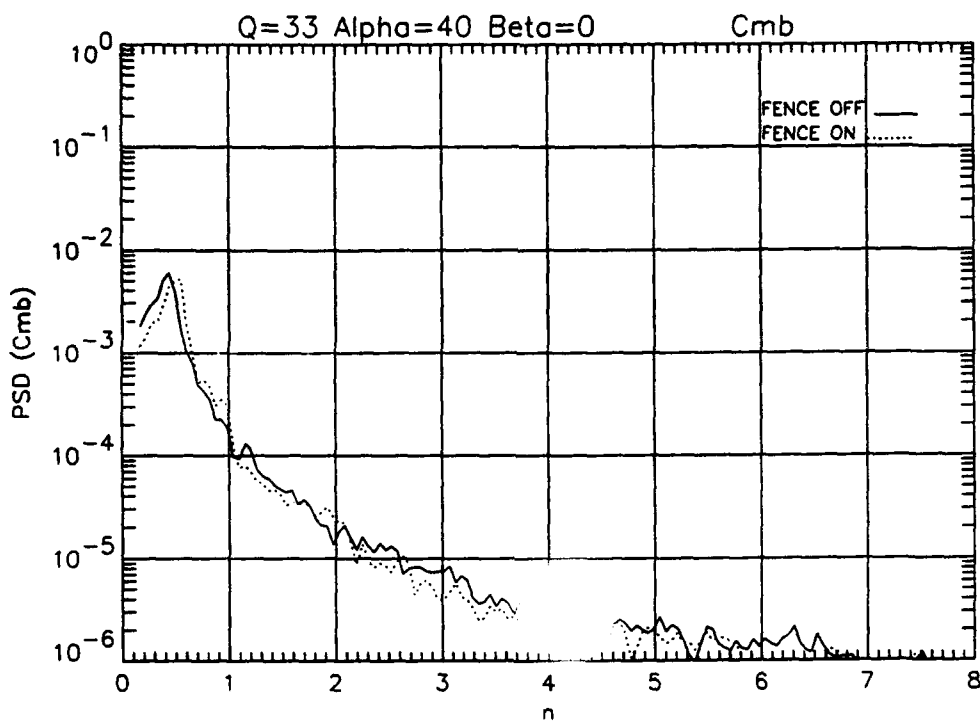
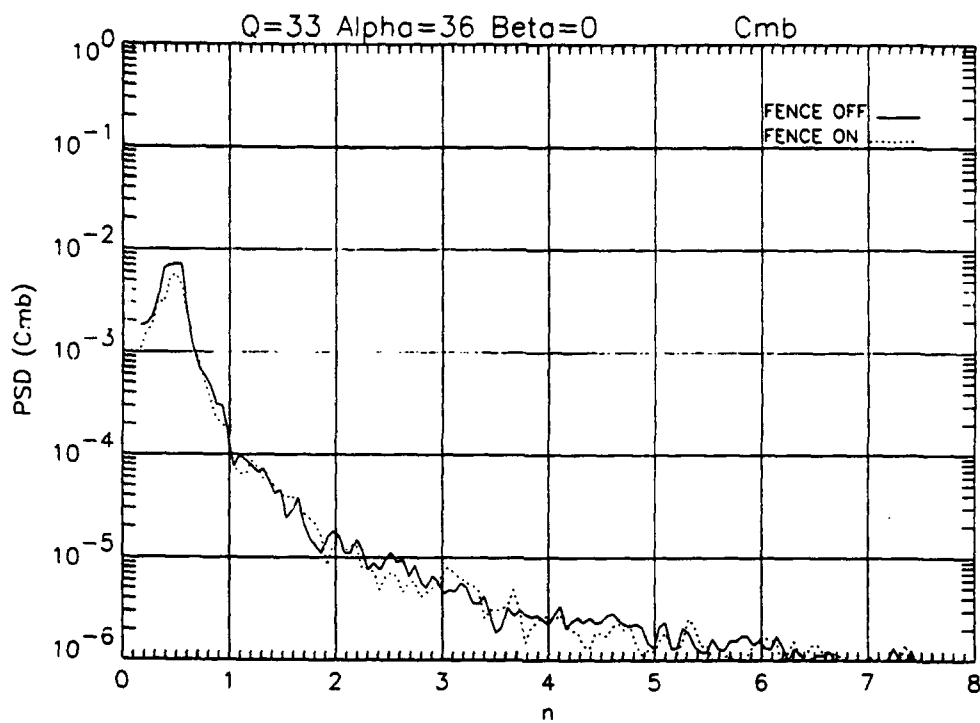
1. Ashley, H., Rock, S.M., Digumarthi, R., Chaney, K., and Eggers Jr., A.J., "Active Control for Fin Buffet Alleviation," WL-TR-93-3099, January 1994.
2. Bendat, J.S. and Piersol, A.G., Random Data, Wiley-Interscience, New York, 1986.
3. Coe, C.F. and Cunningham, A.M., Jr., "Prediction of F-111 TACT Aircraft Buffet Response and Correlations of Fluctuating Pressures Measured on Aluminum and Steel Models and the Aircraft," NASA Contractor Report 4069.
4. Ferman, M.A., Patel, S.R., Zimmerman, N.H., and Gersternkorn, G., "A Unified Approach to Buffet Response of Fighter Aircraft Empennage from Aircraft Dynamic Loads due to Flow Separation," AGARD-CP-483, 1990.
5. Jones, J.G., "A Survey of the Dynamic Analysis of Buffeting and Related Phenomena," RAE TR 72197, 1973.
6. Landahl, M. and Mollo-Christensen, E., Turbulence and Random Processes in Fluid Mechanics, Cambridge University Press, New York, 1992.
7. Levraea, V., Henderson, D., Pacia, A., and Banford, M., "Modal Survey of a Full-Scale F-18 Wind Tunnel Model," WL-TM-92-350-FIBG, September 1992.
8. Lee, B.H.K., Brown, D., Zgela, M., and Poirel, D., "Wind Tunnel and Flight Tests of Tail Buffet on the F/A-18 Aircraft", from Aircraft Dynamic Loads due to Flow Separation," AGARD-CP-483, 1990.
9. Lee, B.H.K., Brown, D., Tang, F.C., and Plosneski, M., "Flowfield in the Vicinity of an F/A-18 Vertical Fin at High Angles of Attack", *Journal of Aircraft*, Vol. 30, No. 1, 1993.
10. Mabey, D., "Some Aspects of Aircraft Dynamic Loads Due to Flow Separation," AGARD-R-750, October, 1987.
11. Meyn, L. and James, K., "Full Scale Wind Tunnel Studies of F/A-18 Tail Buffet," AIAA Applied Aerodynamics Conference, Monterey, California, August 1993.
12. Triplert, W., "Pressure Measurements on Twin Vertical Tails in Buffeting Flow," AFWAL-TR-82-3015, Volume 1 and 2, April 1982.

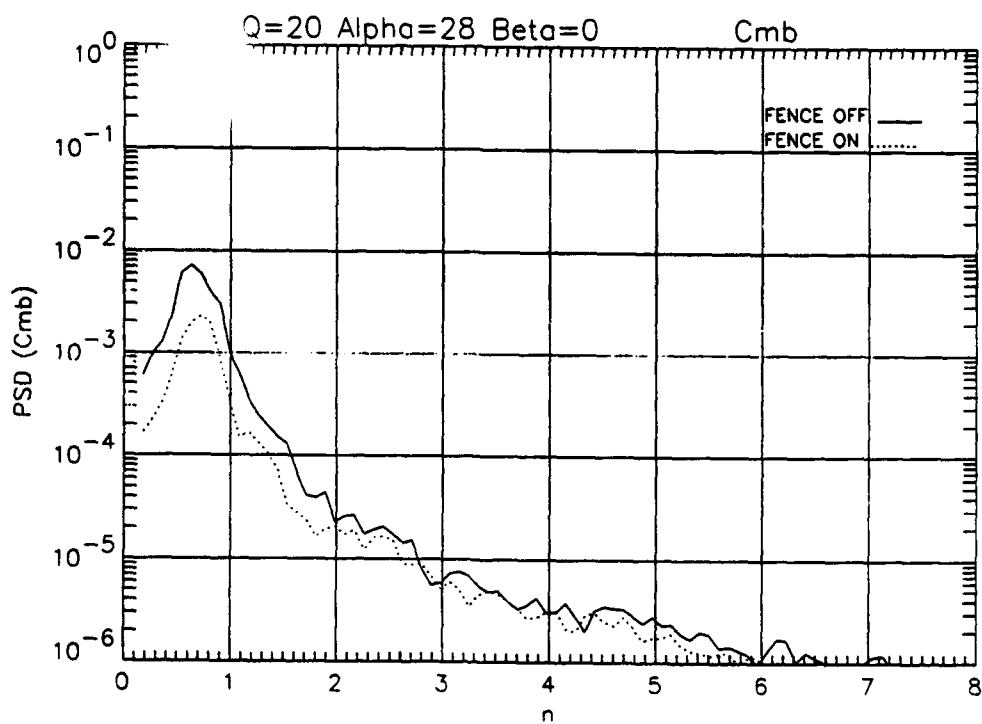
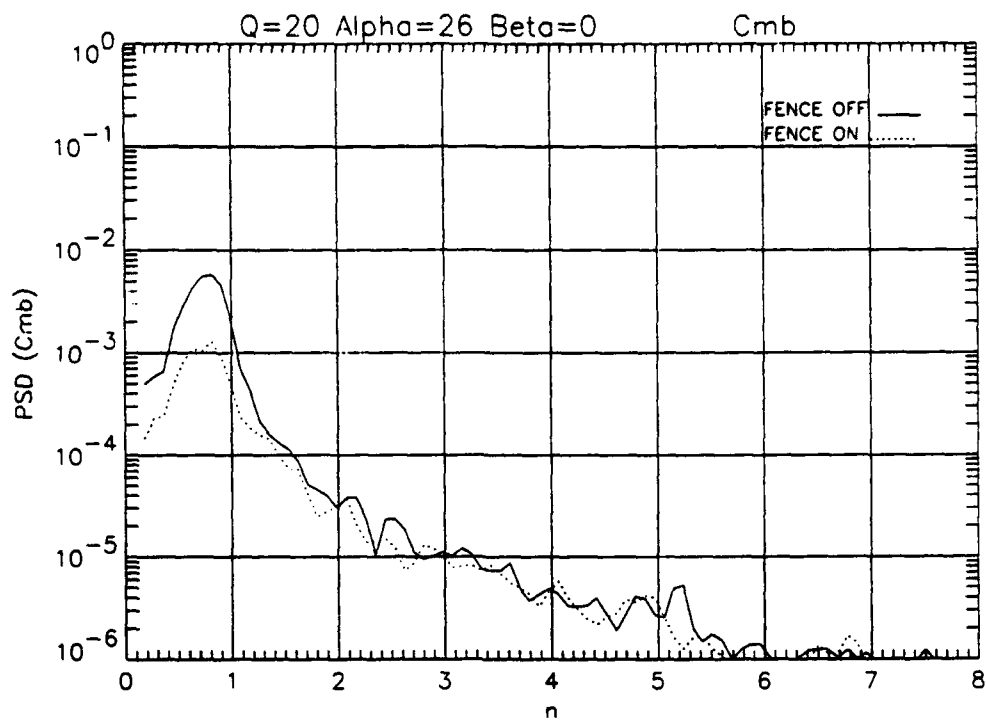
Appendix I
Normal Force and Root Bending Moment
Power Spectral Densities

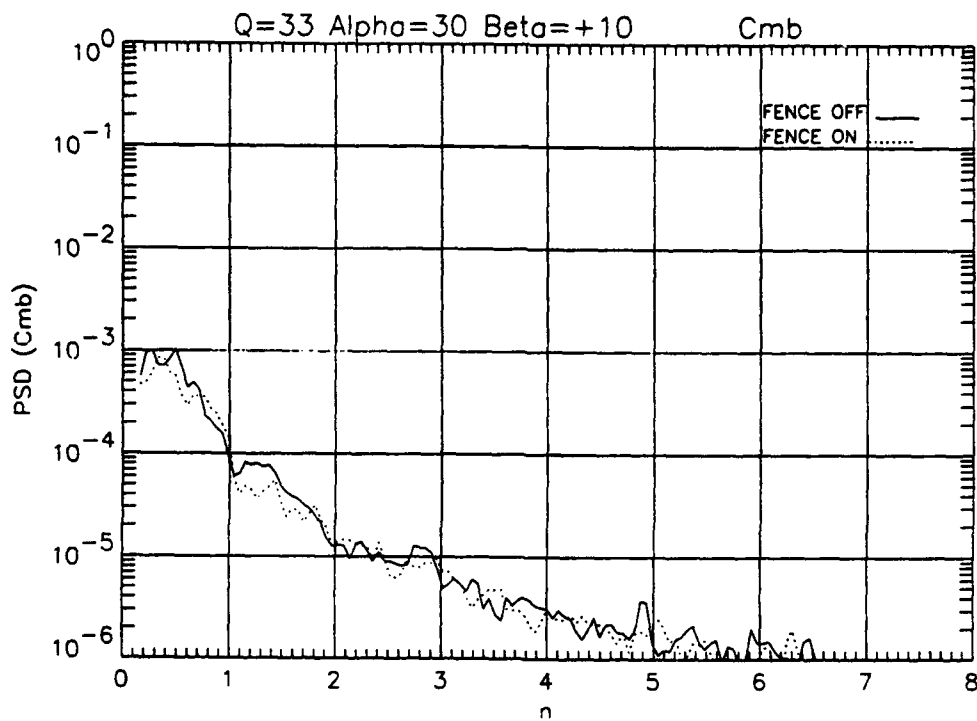
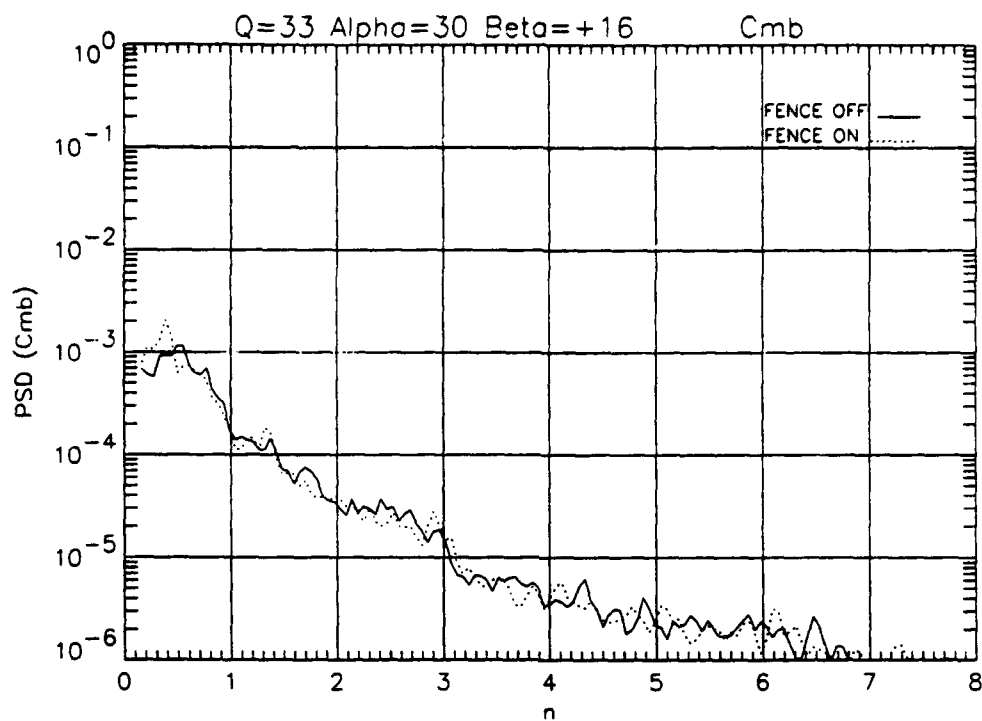


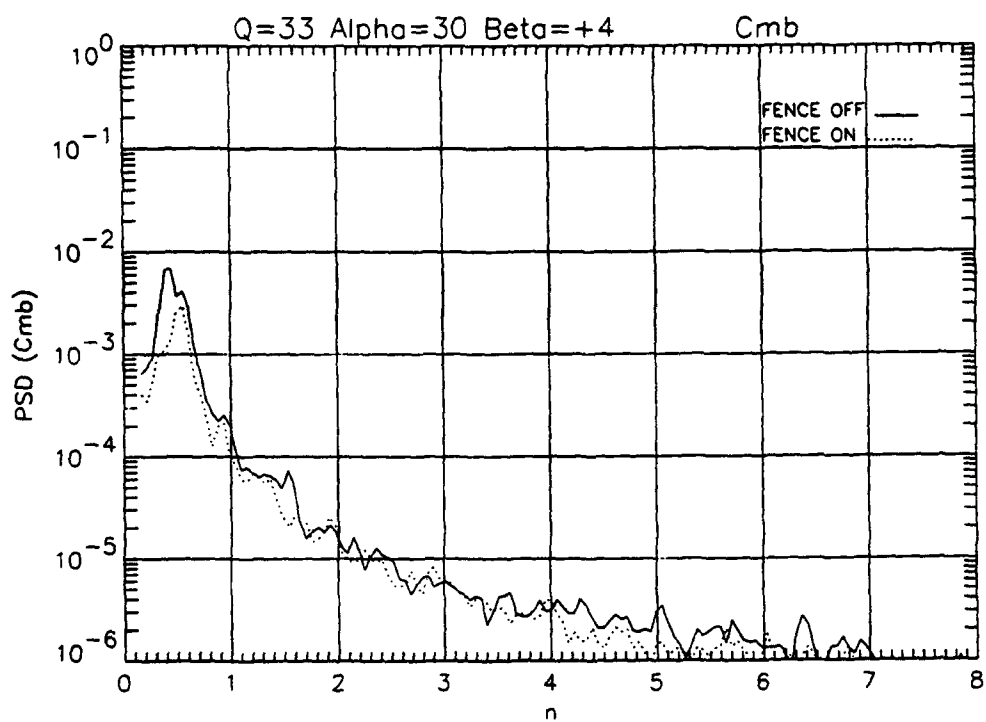
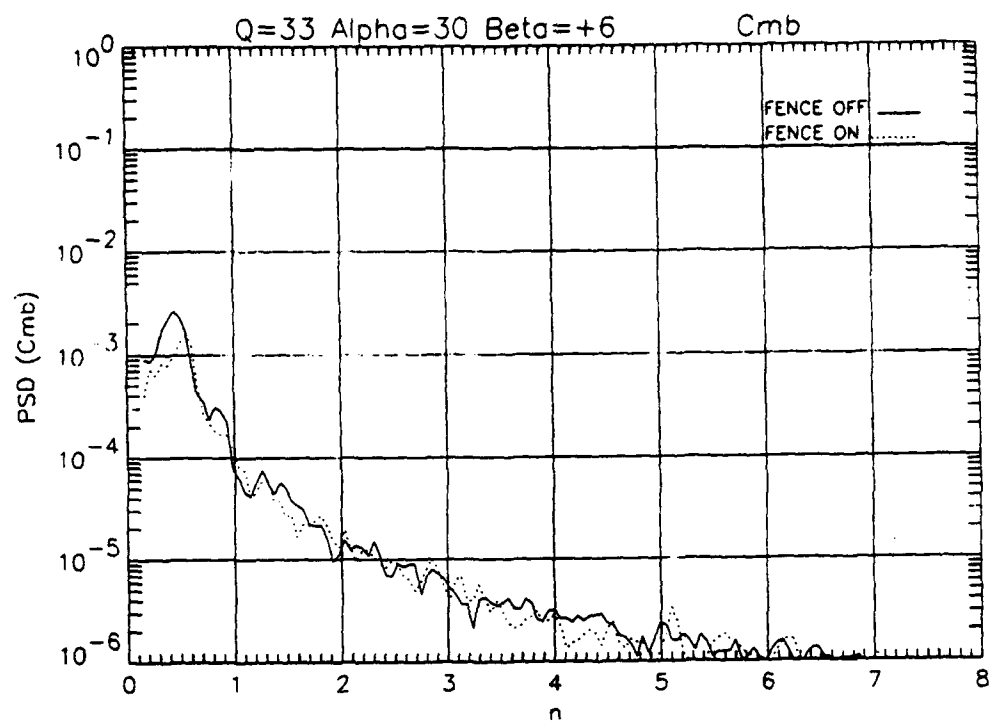


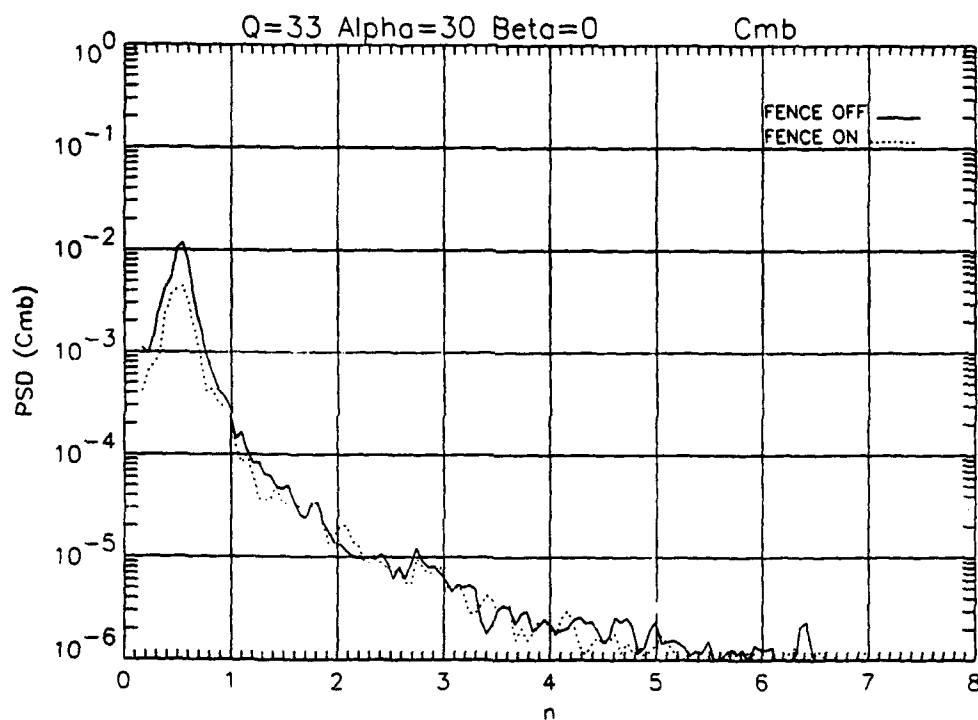
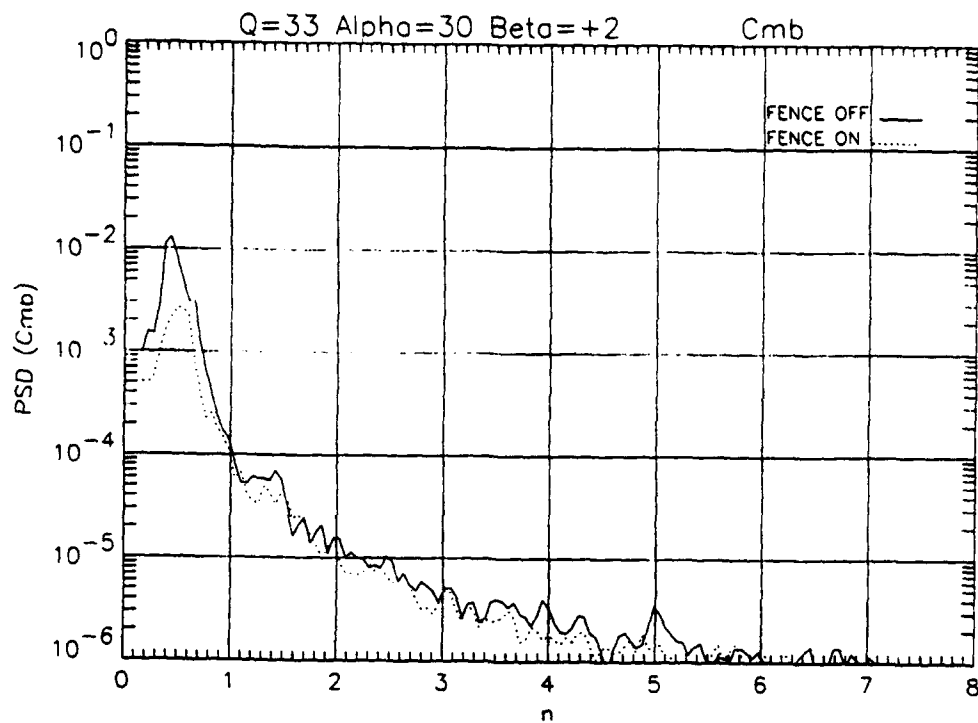


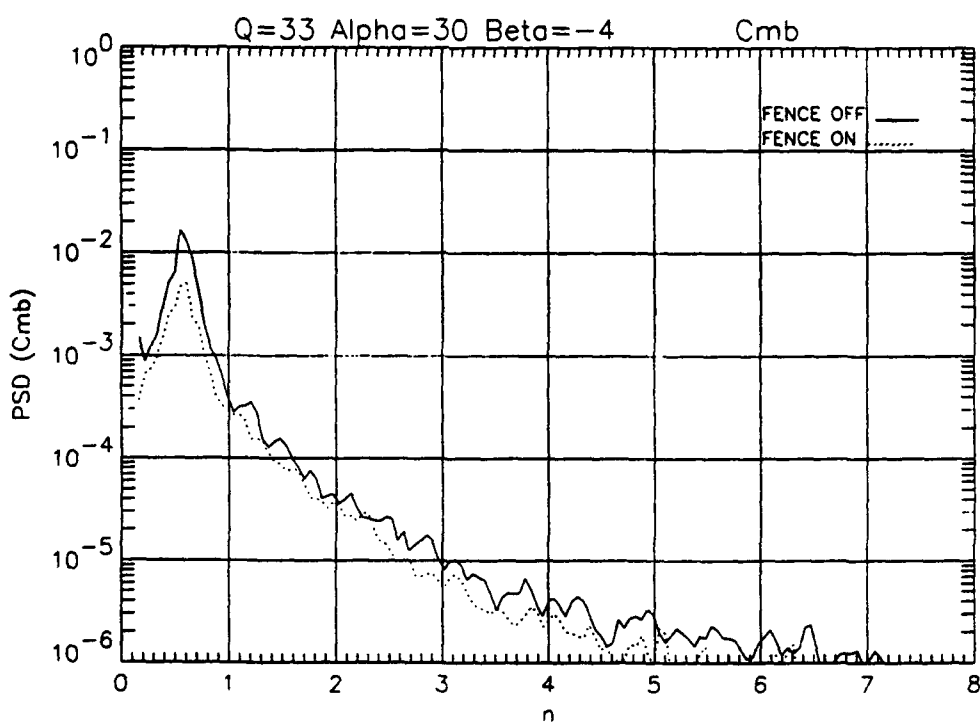
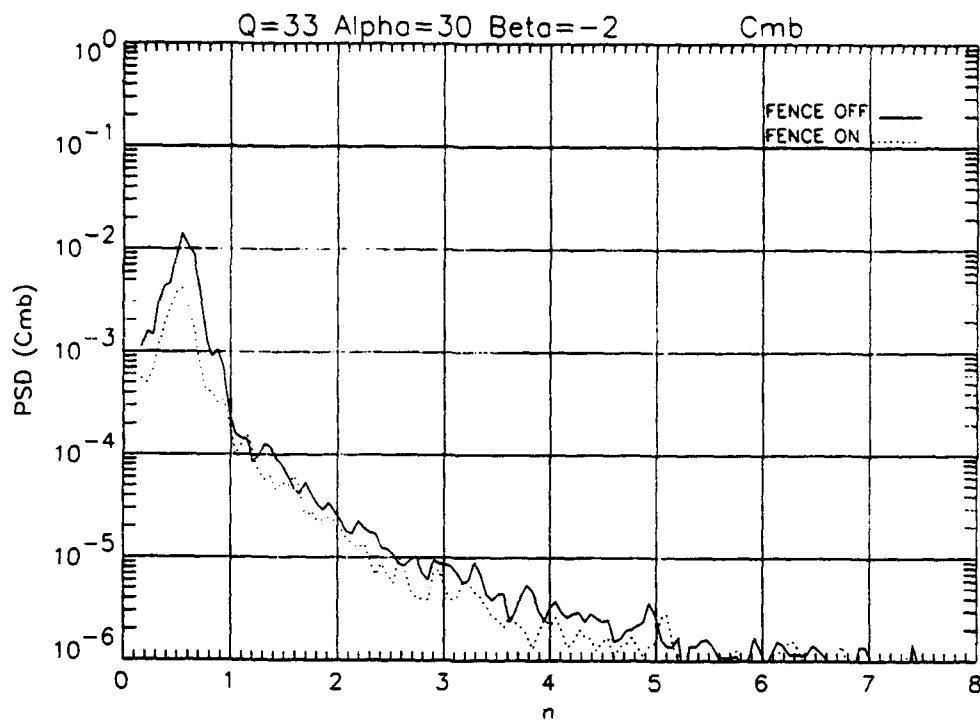


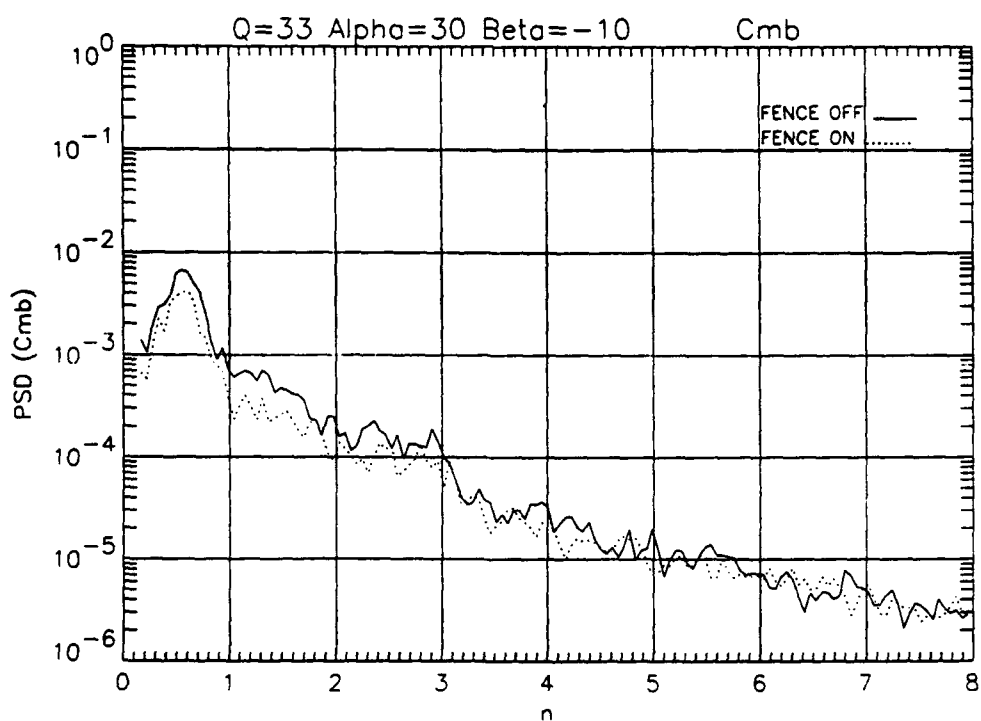
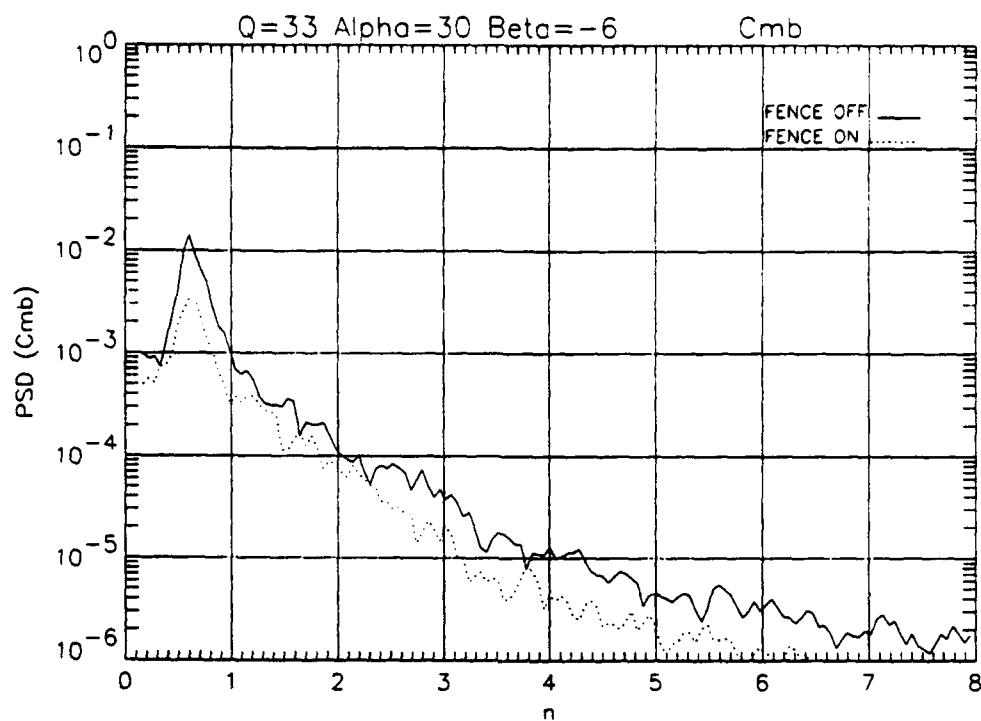


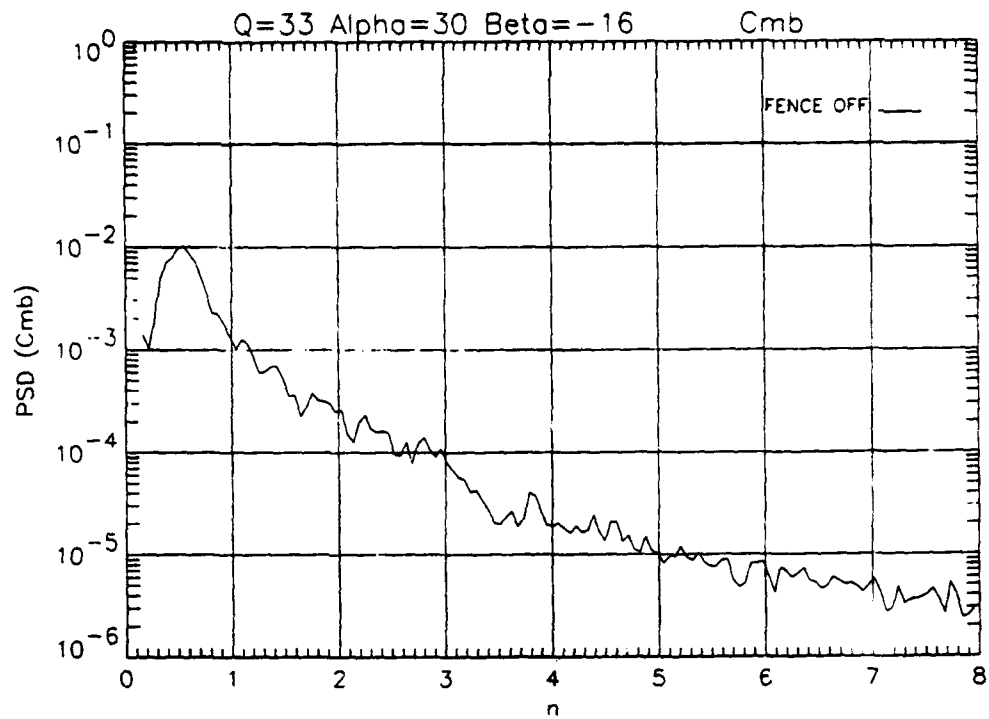


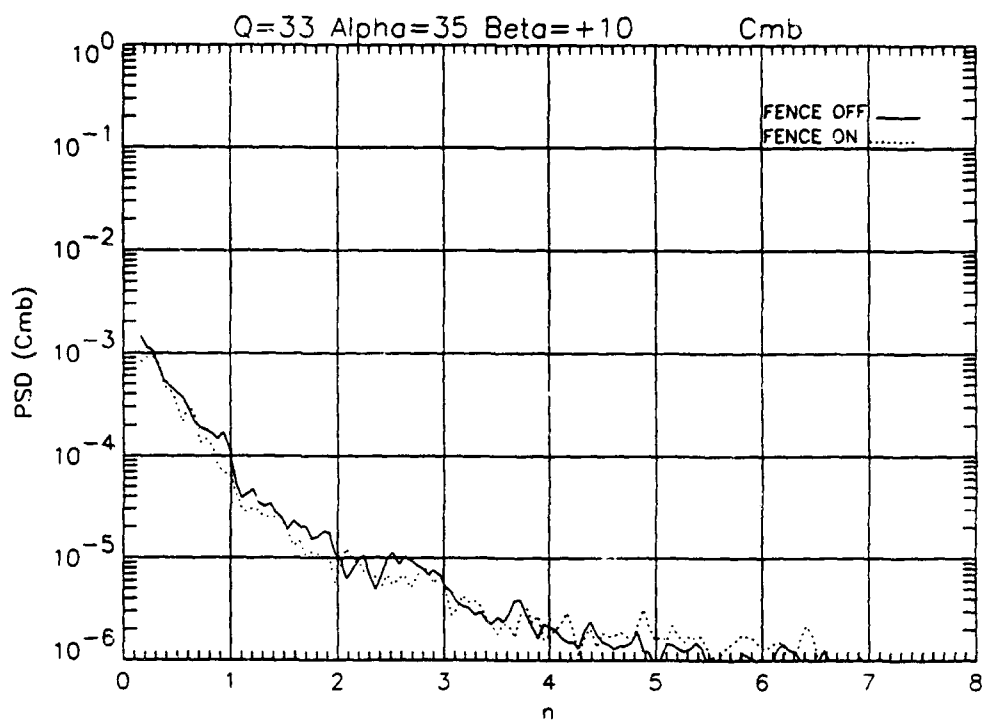
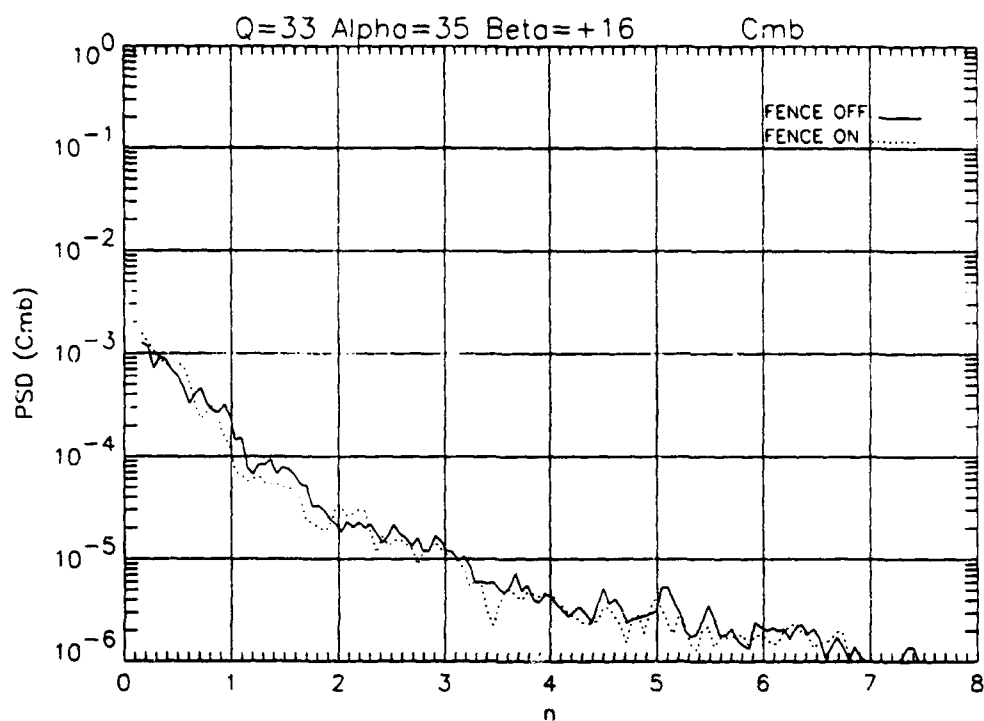


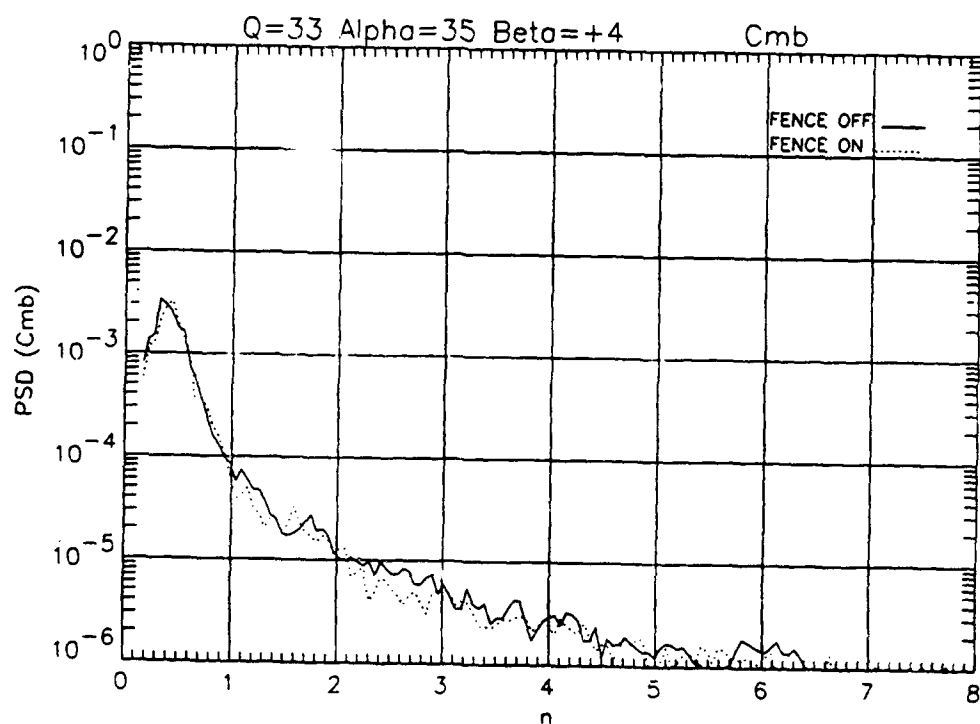
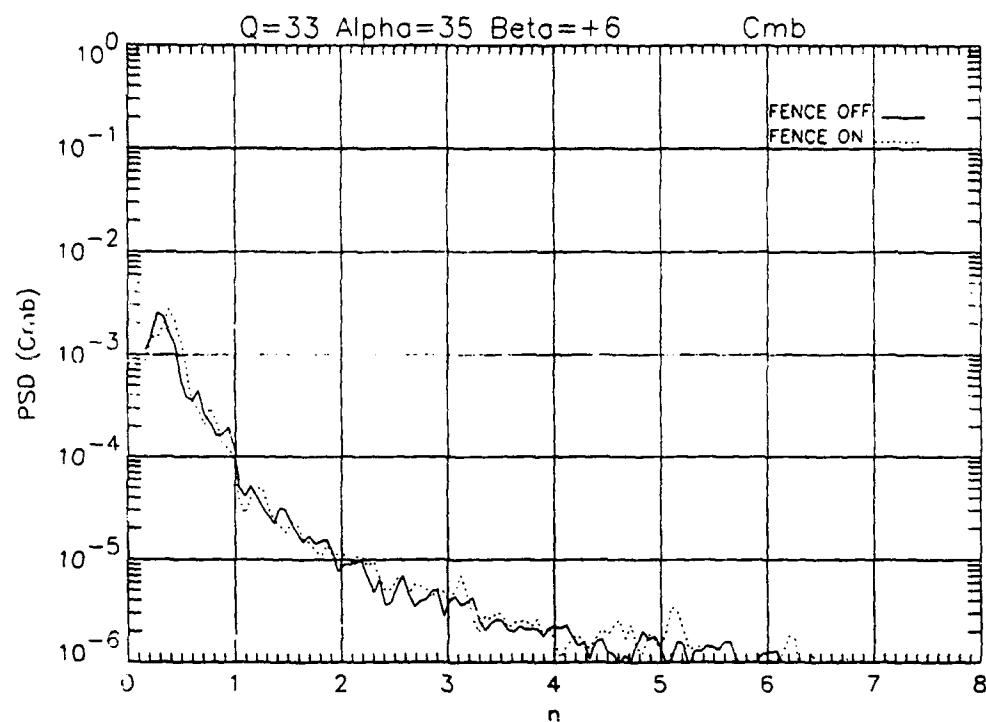


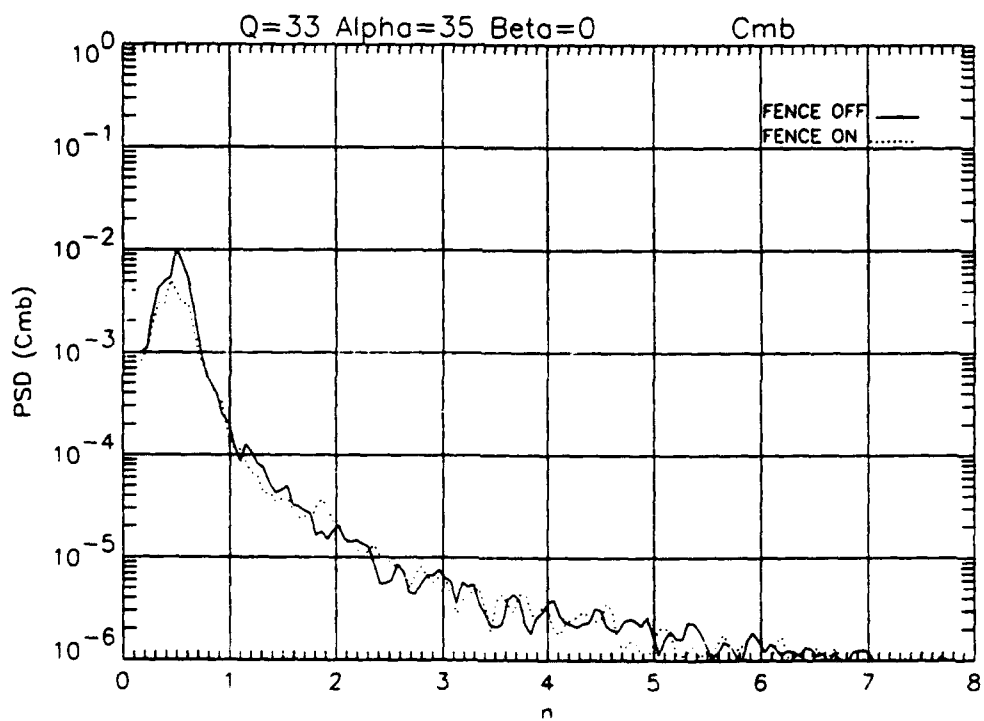
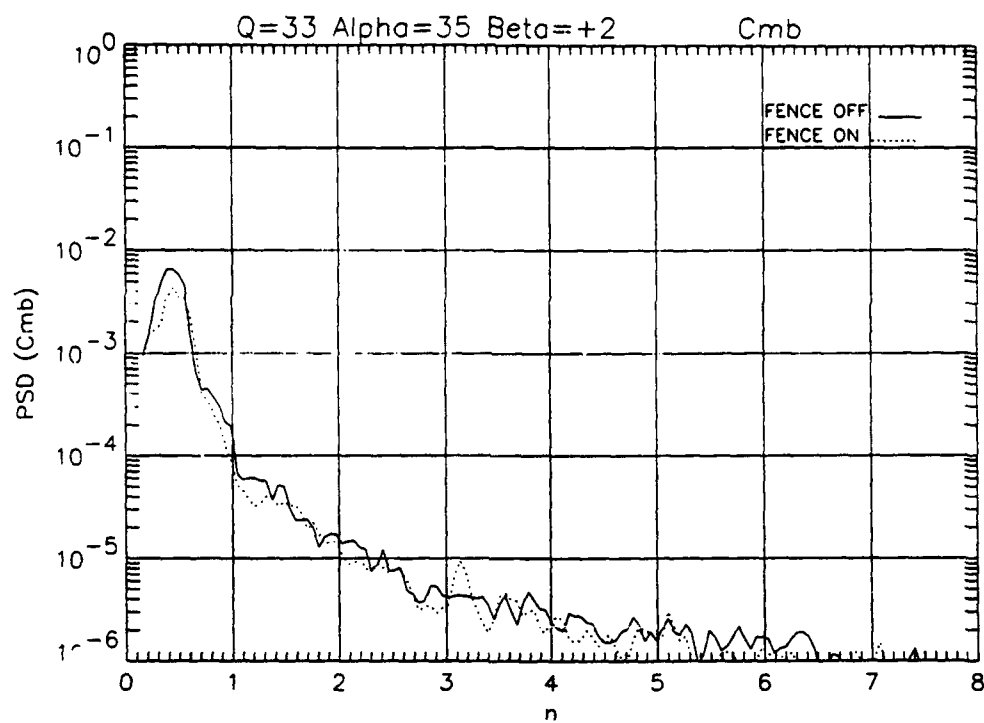


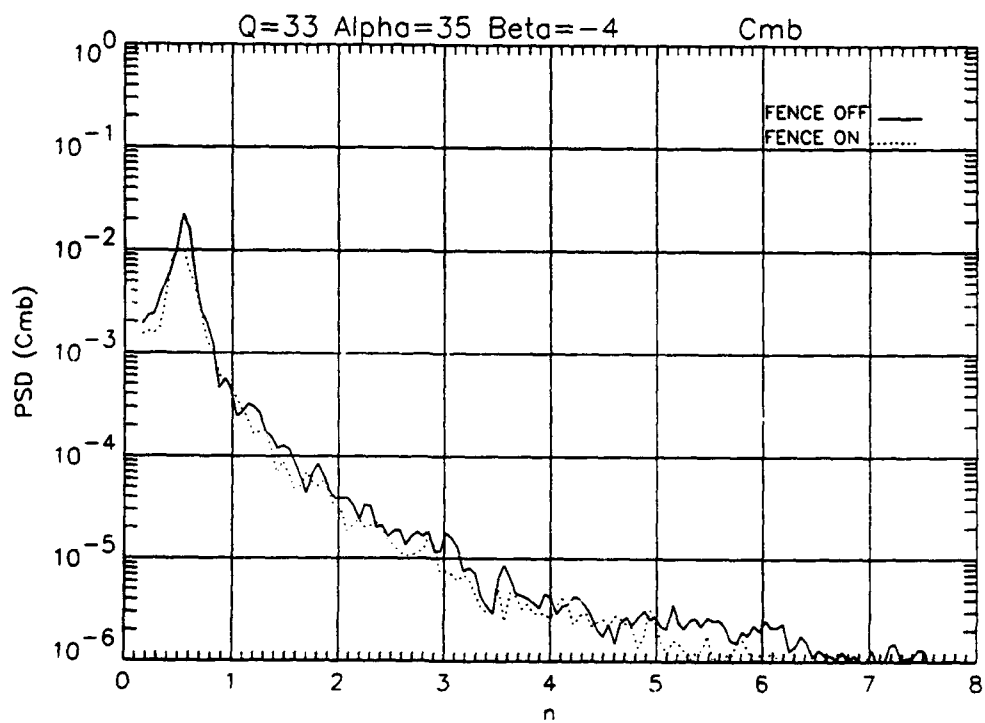
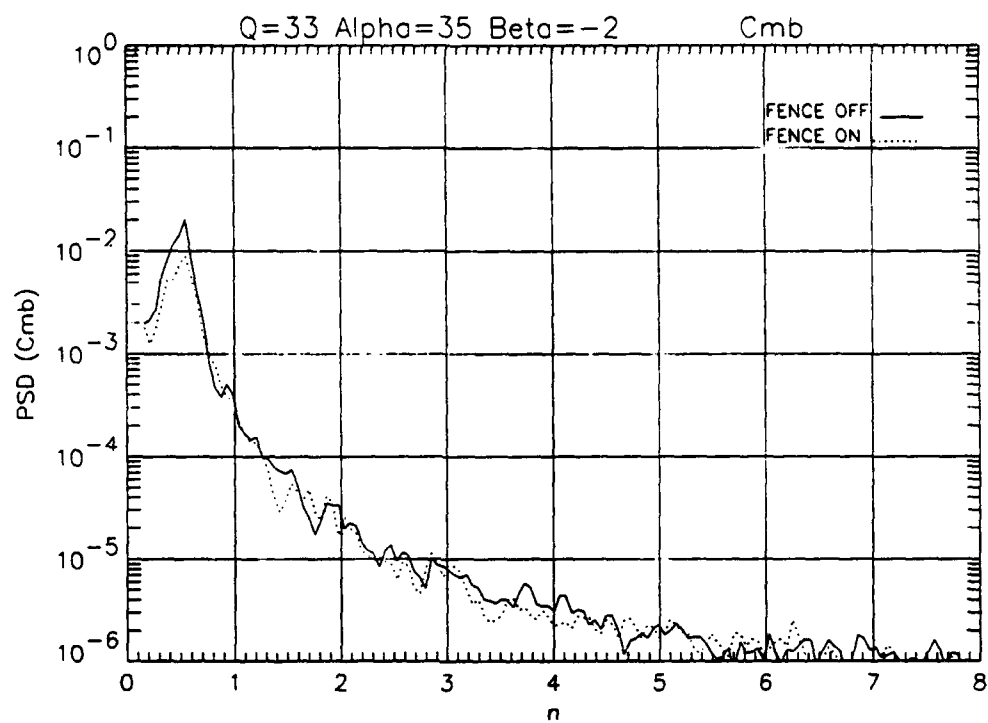


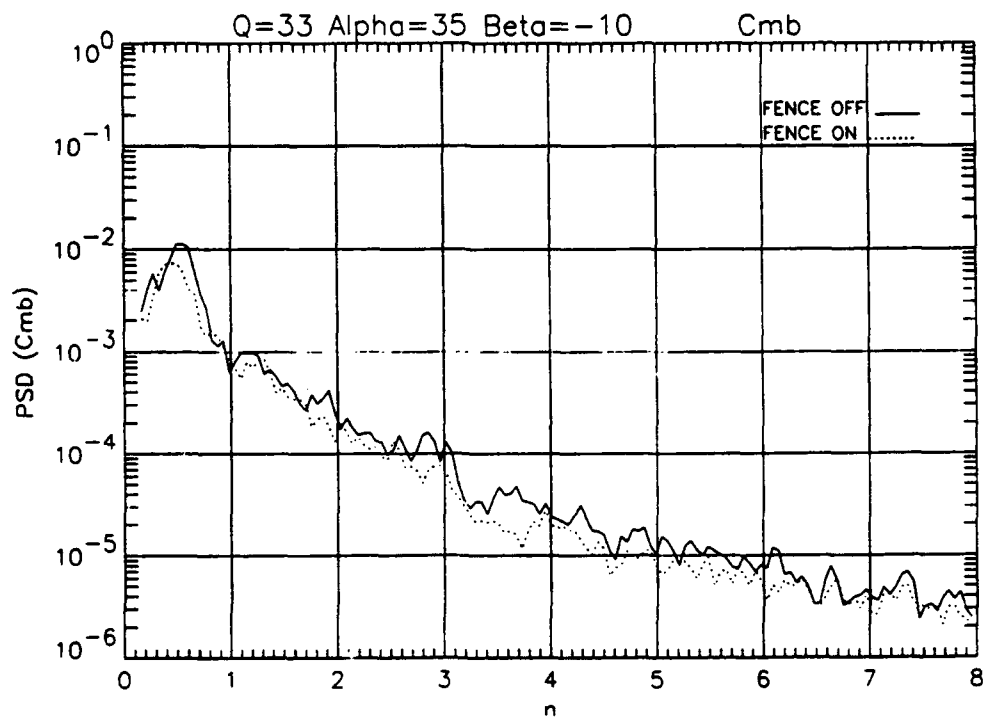
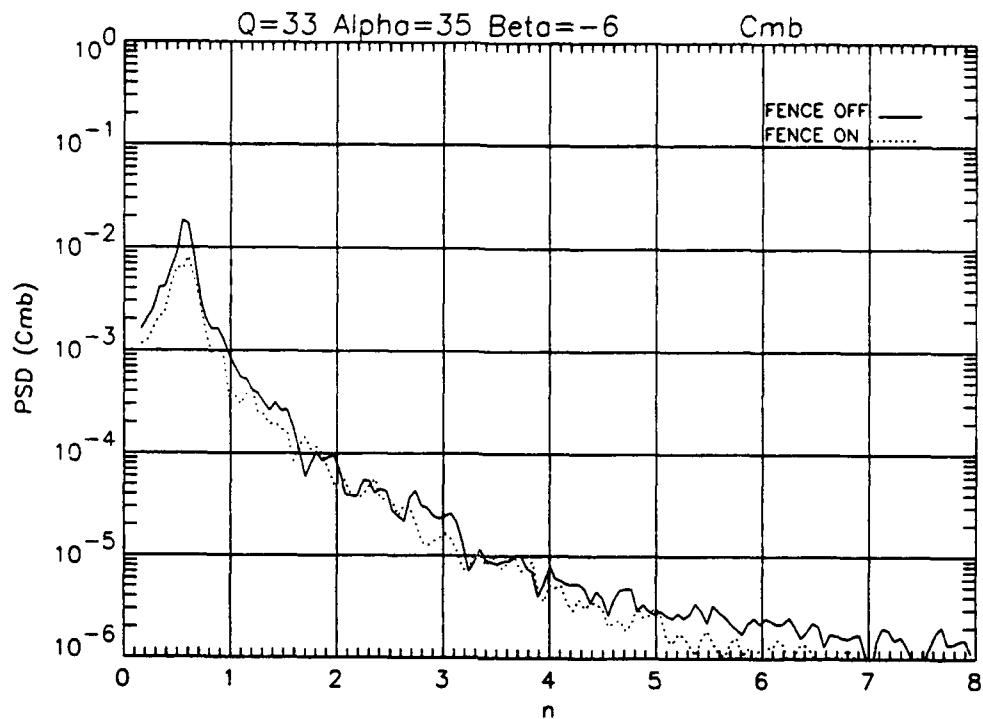


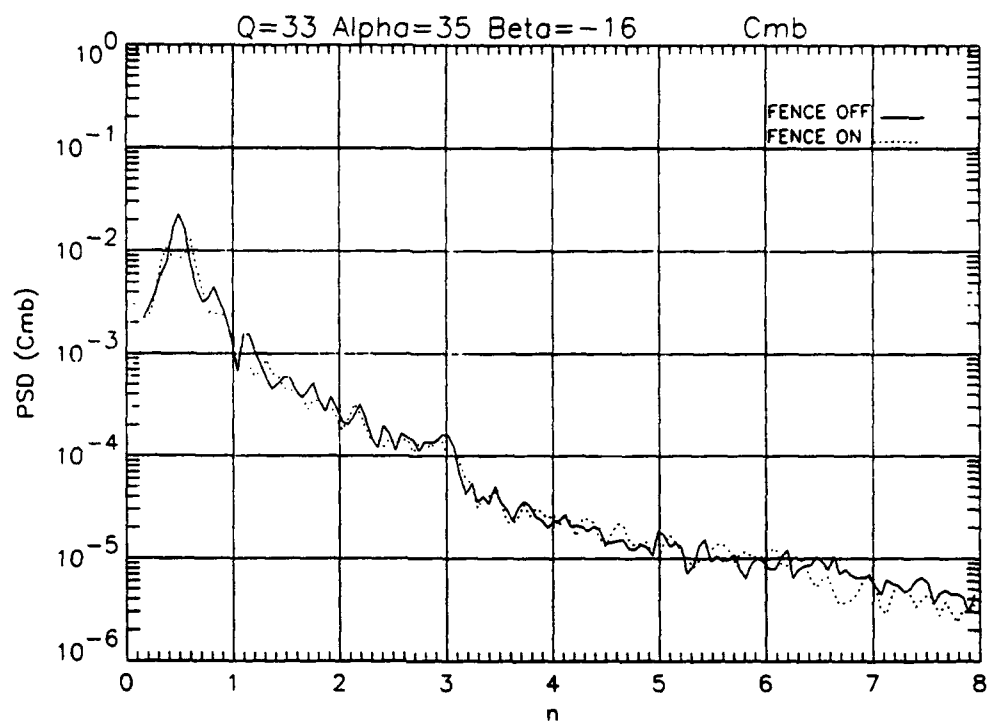


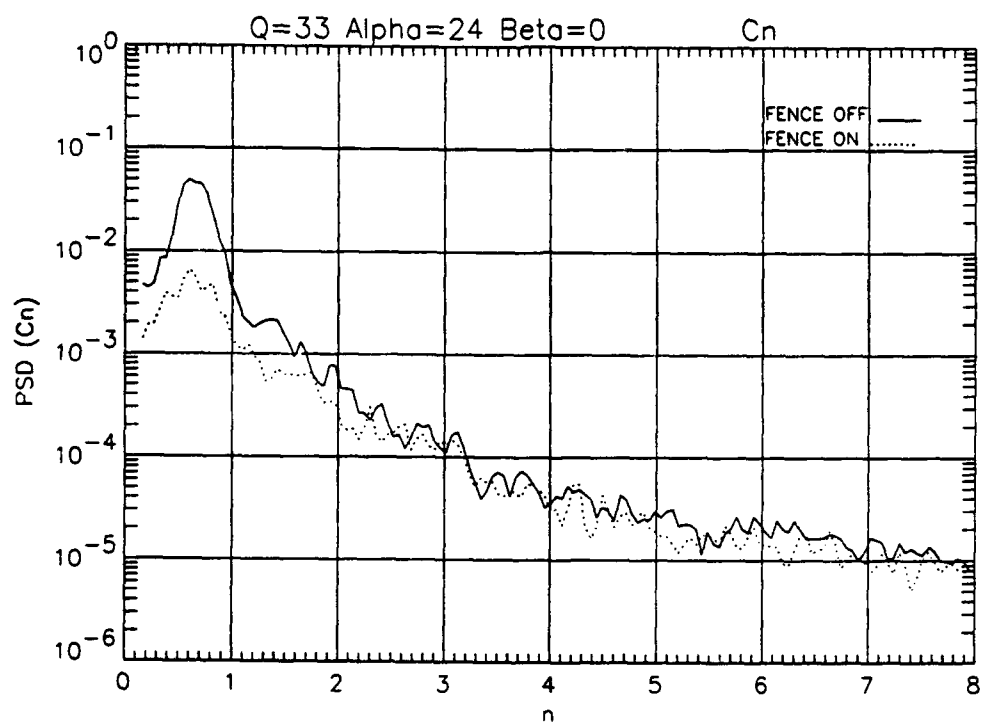
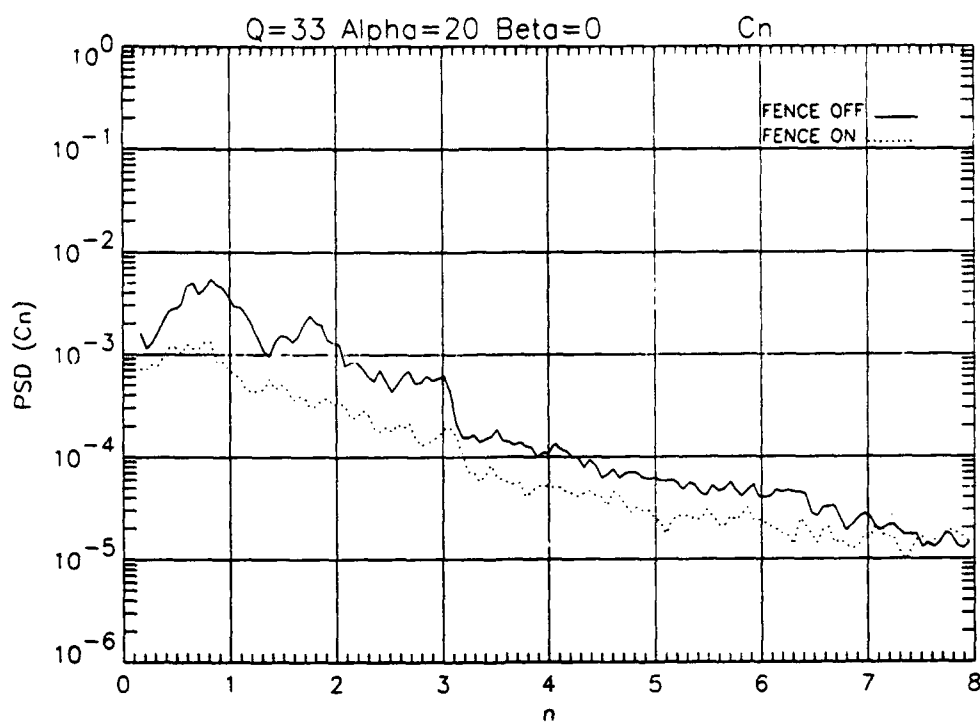


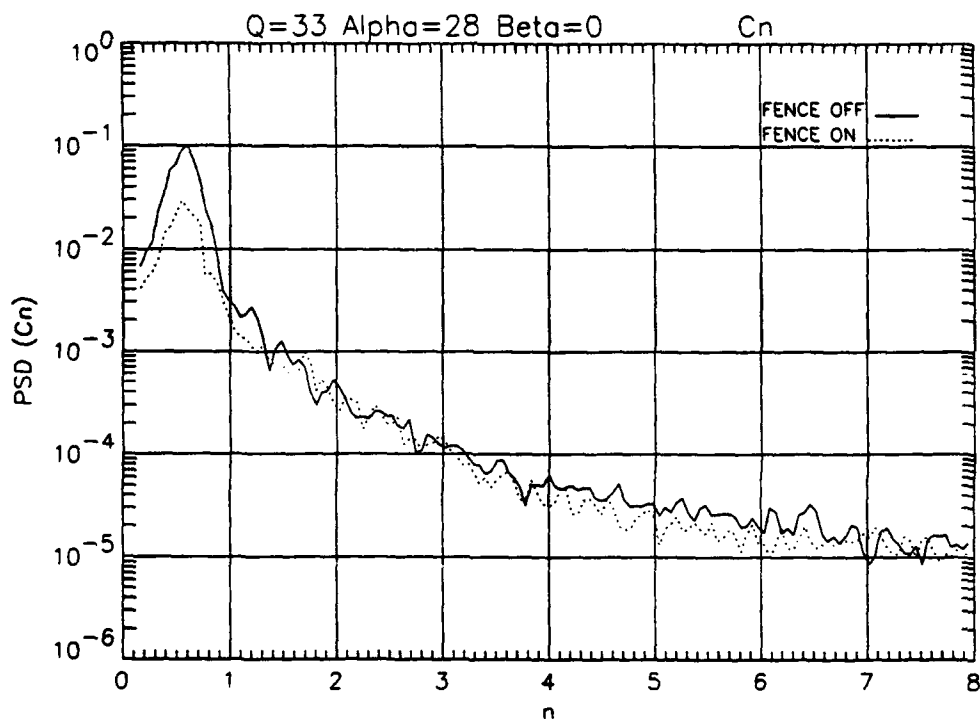
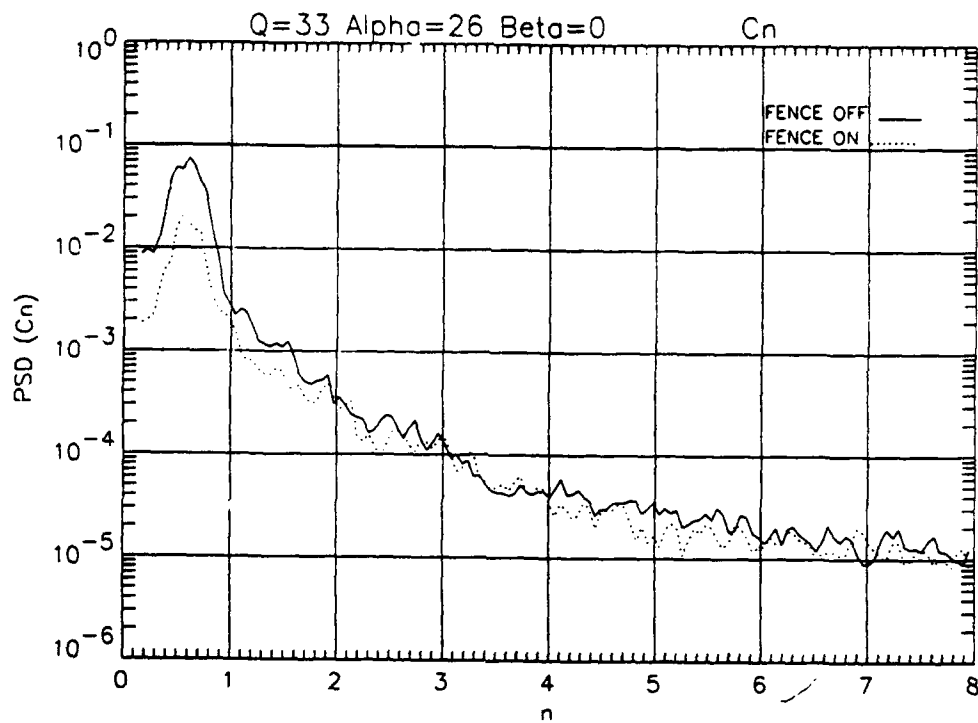


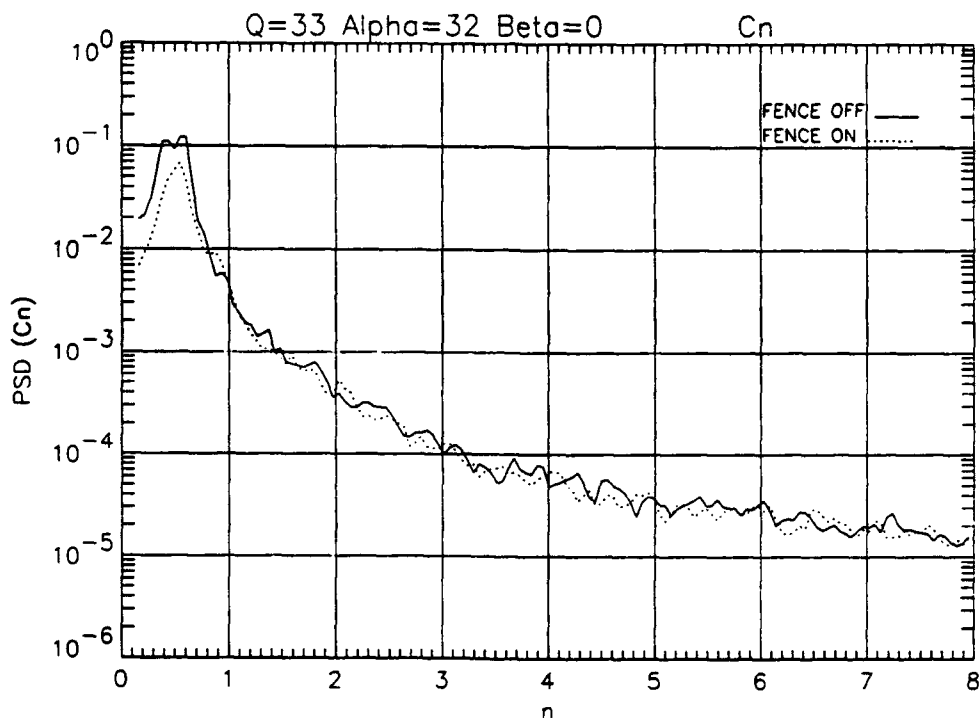
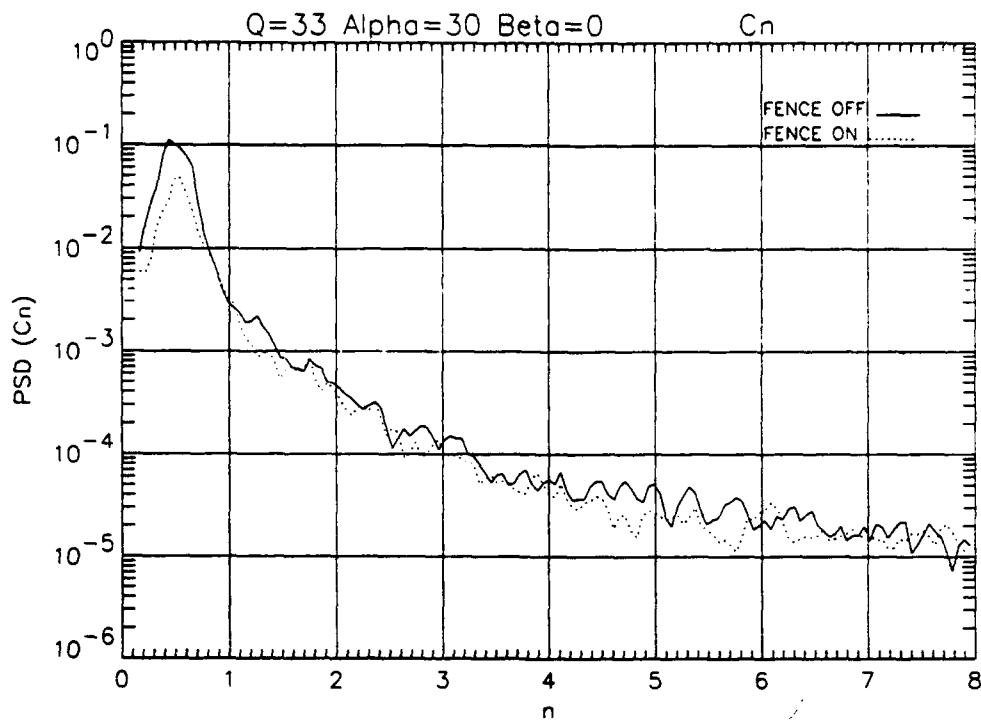


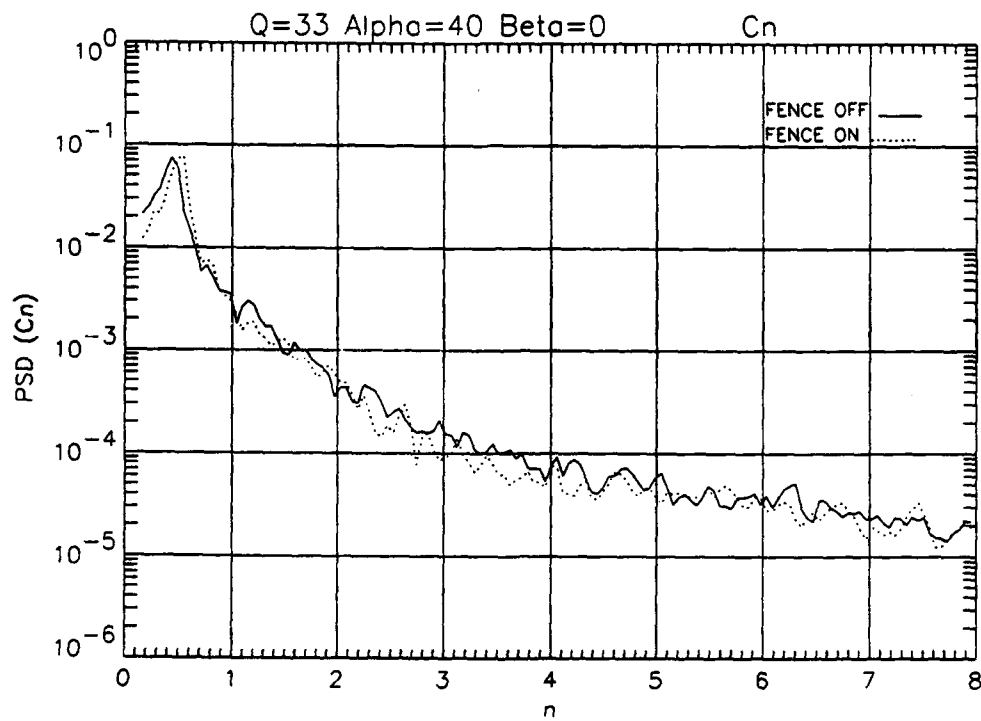
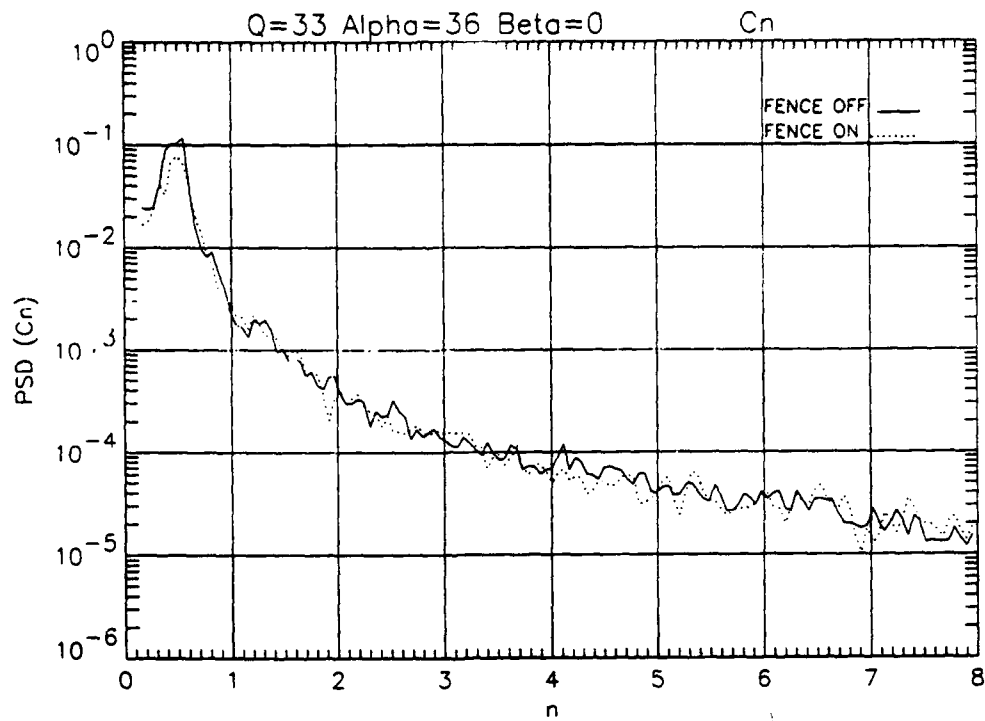


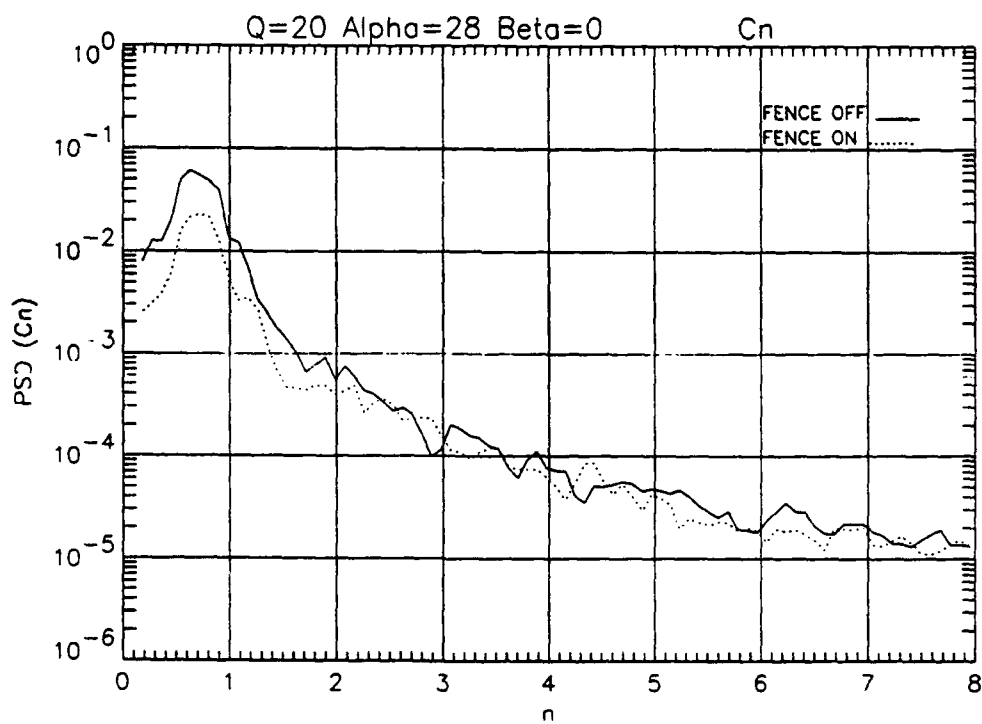
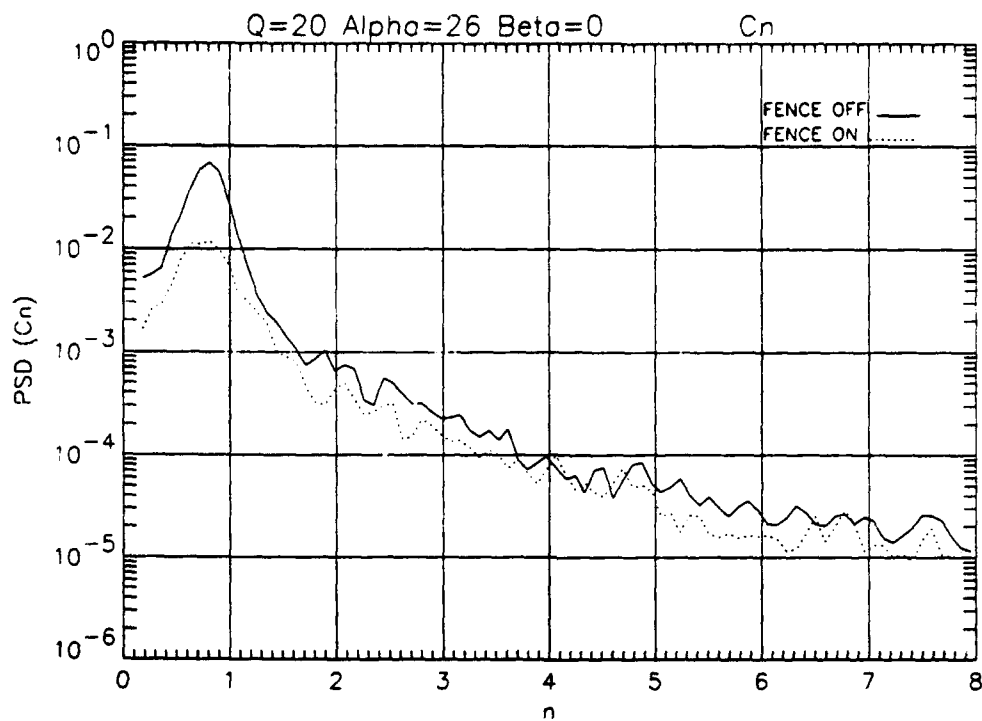


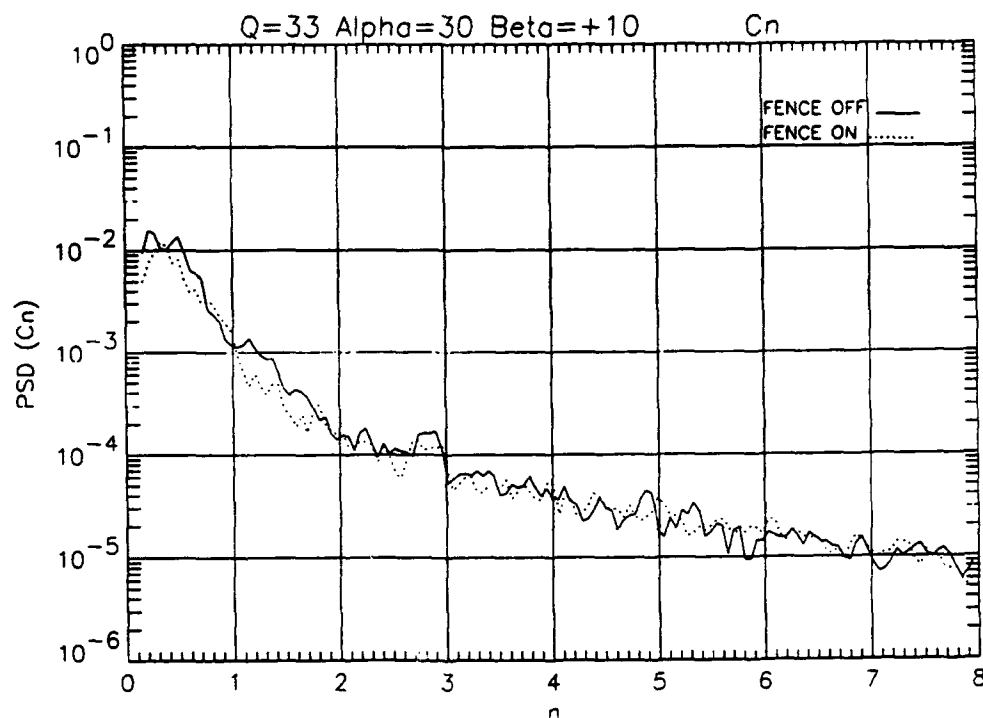
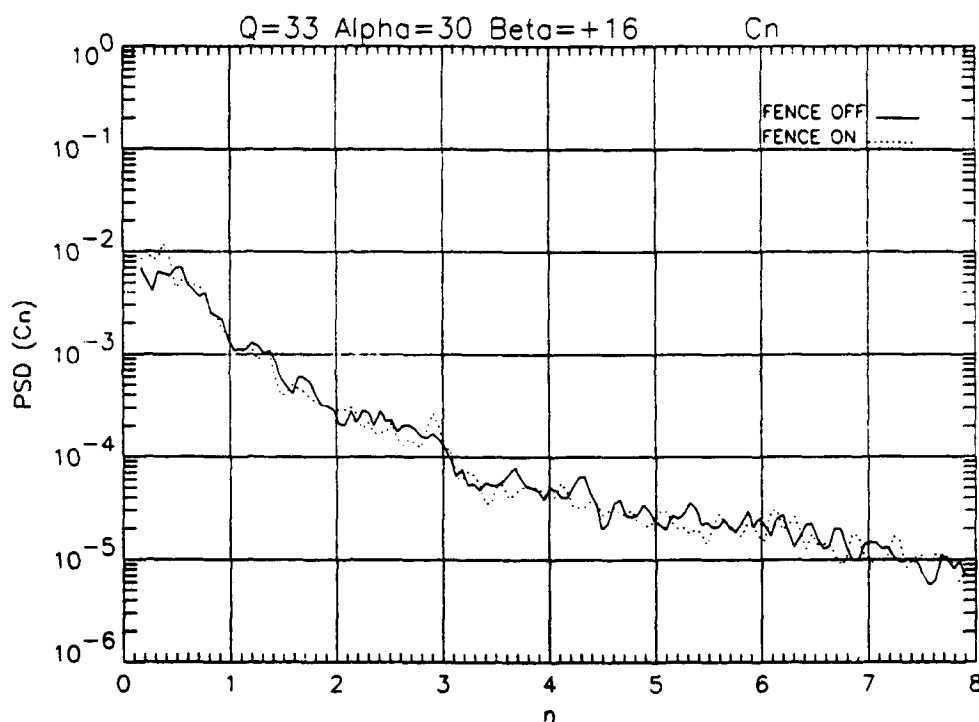


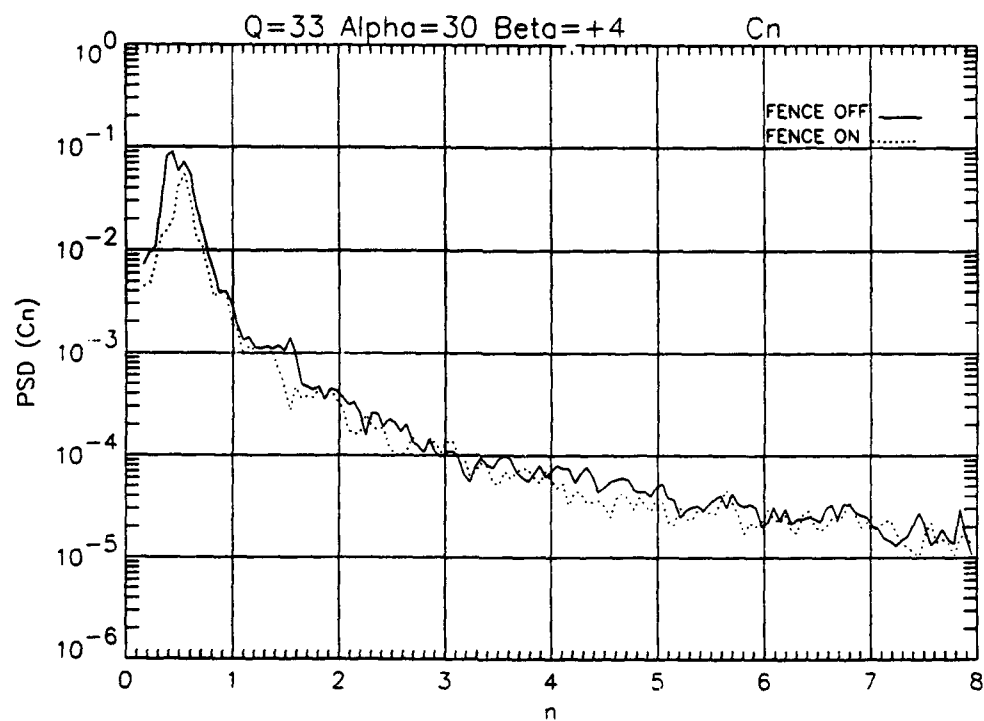
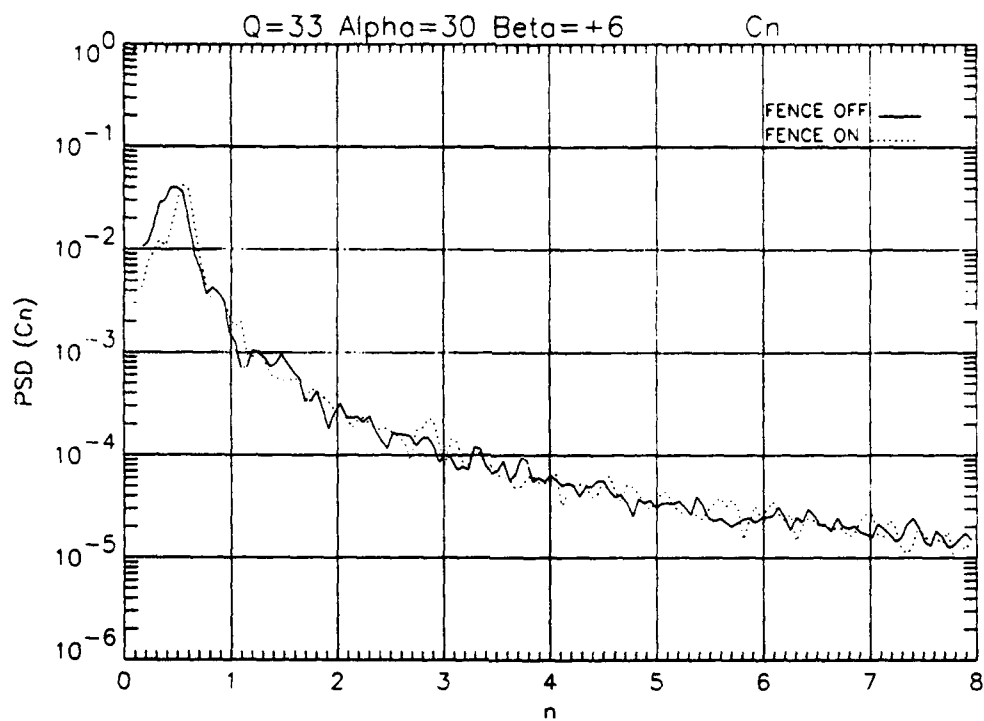


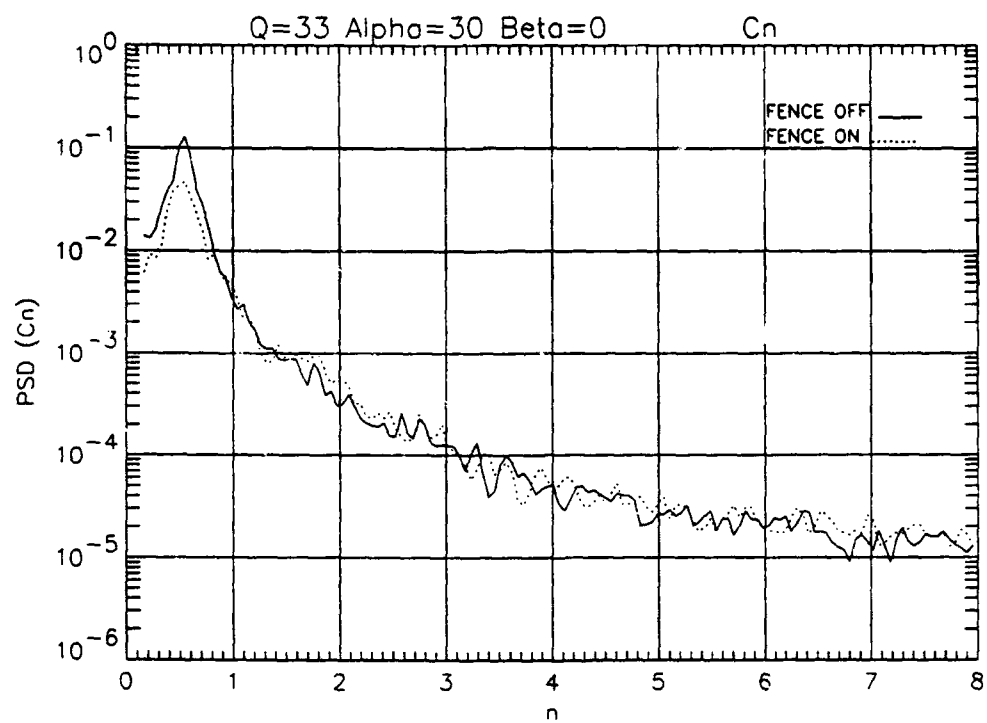
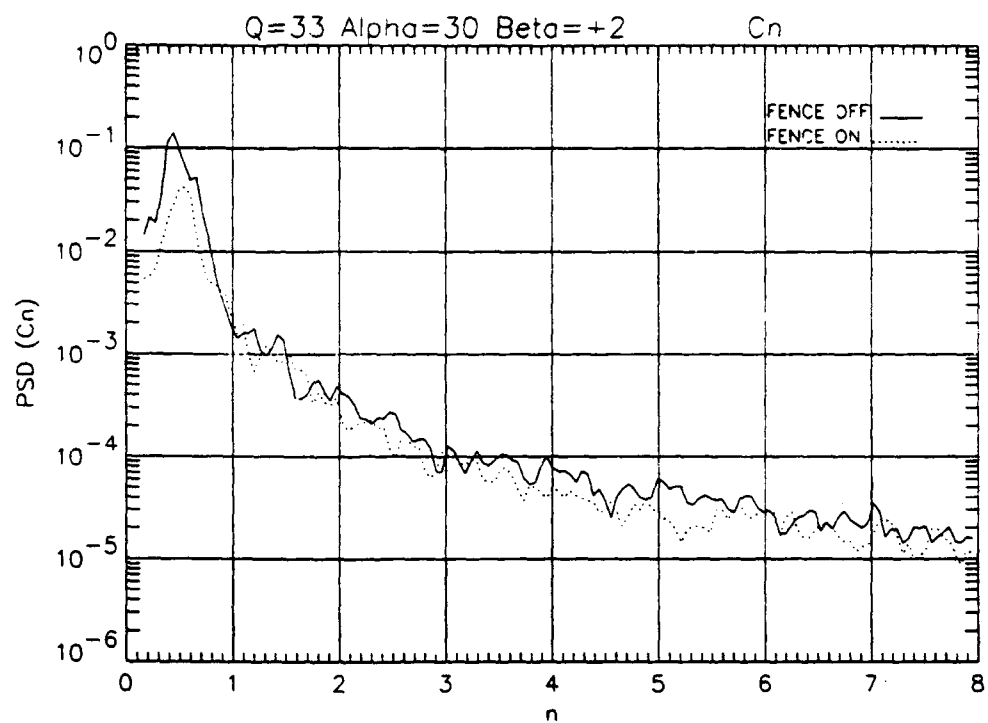


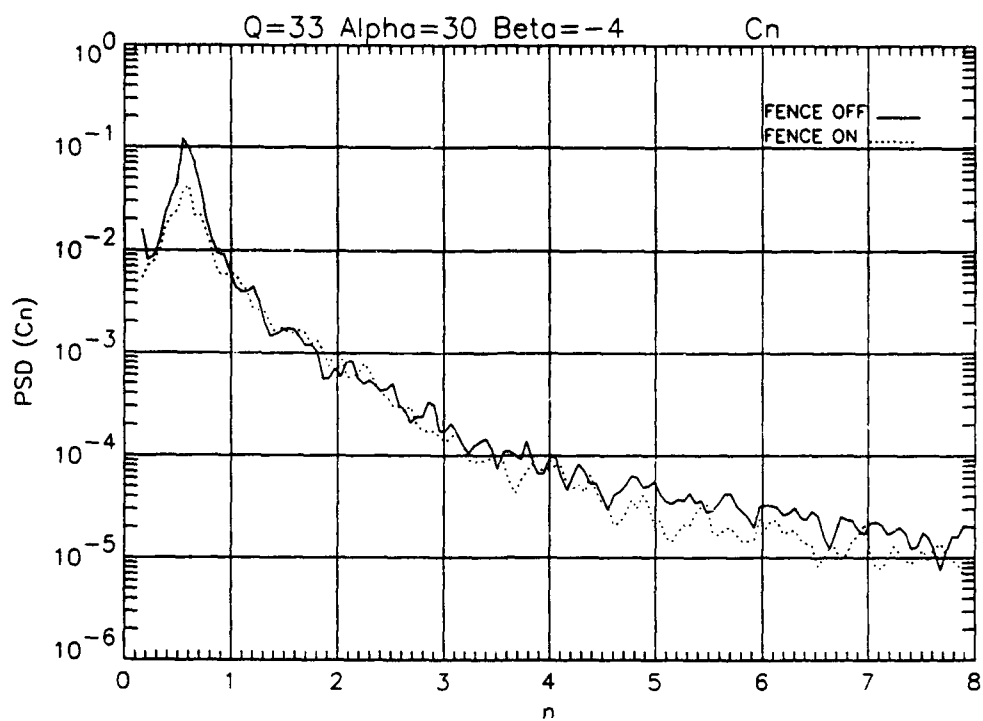
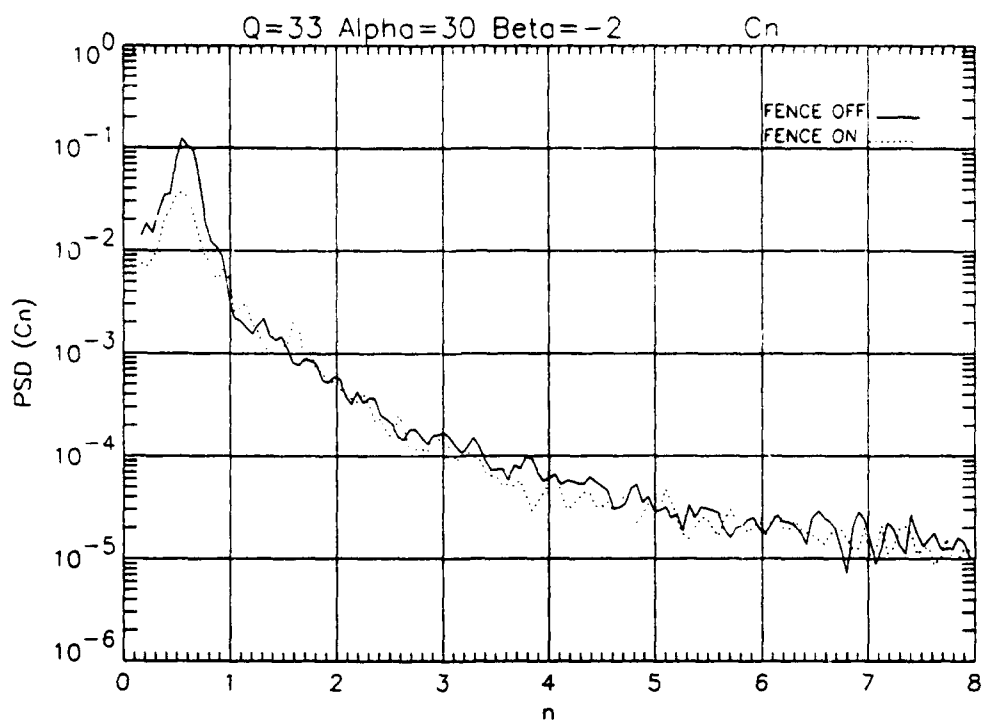


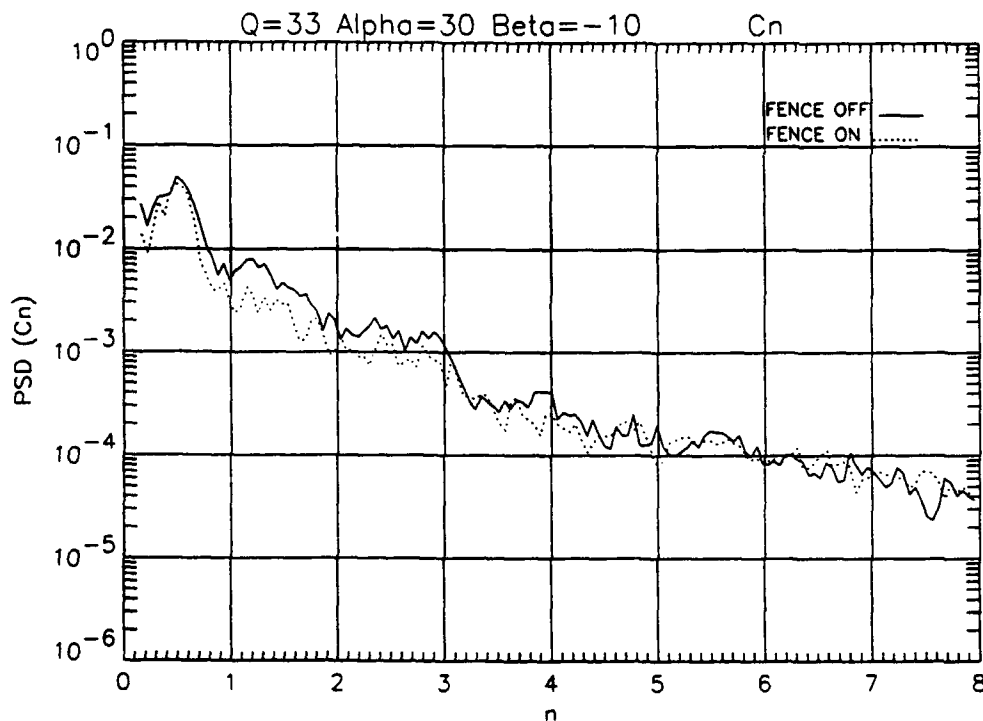
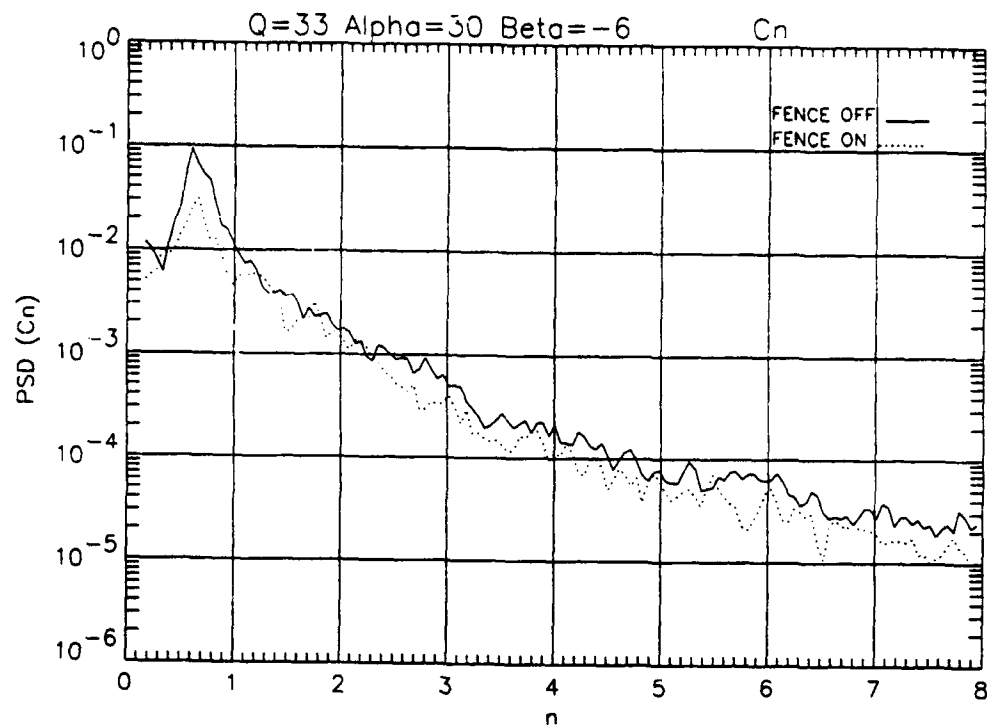


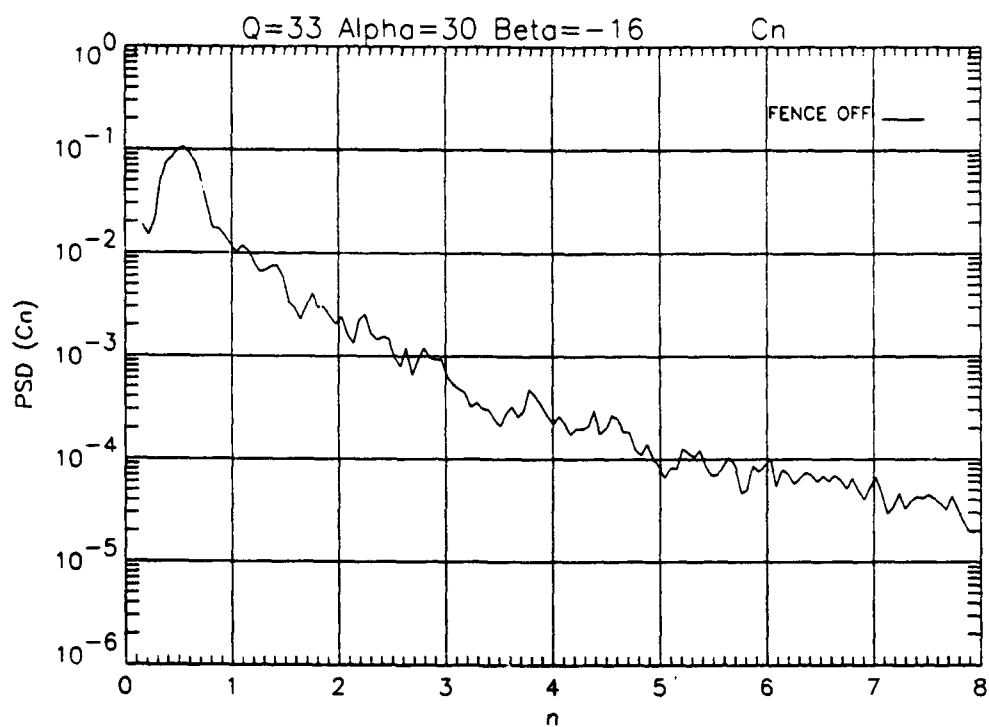


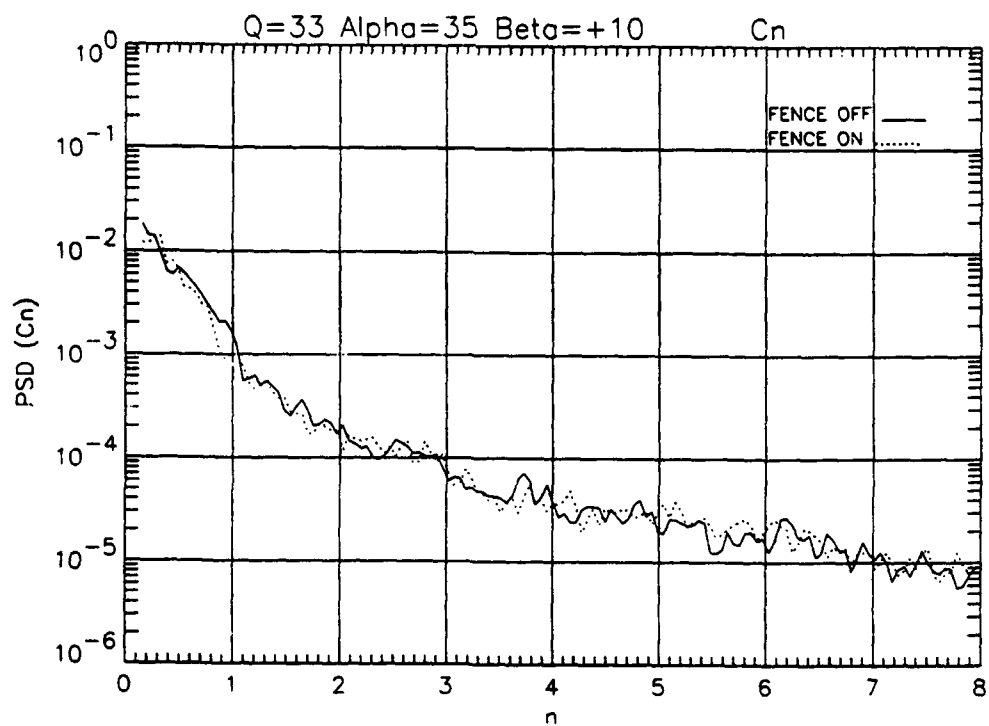
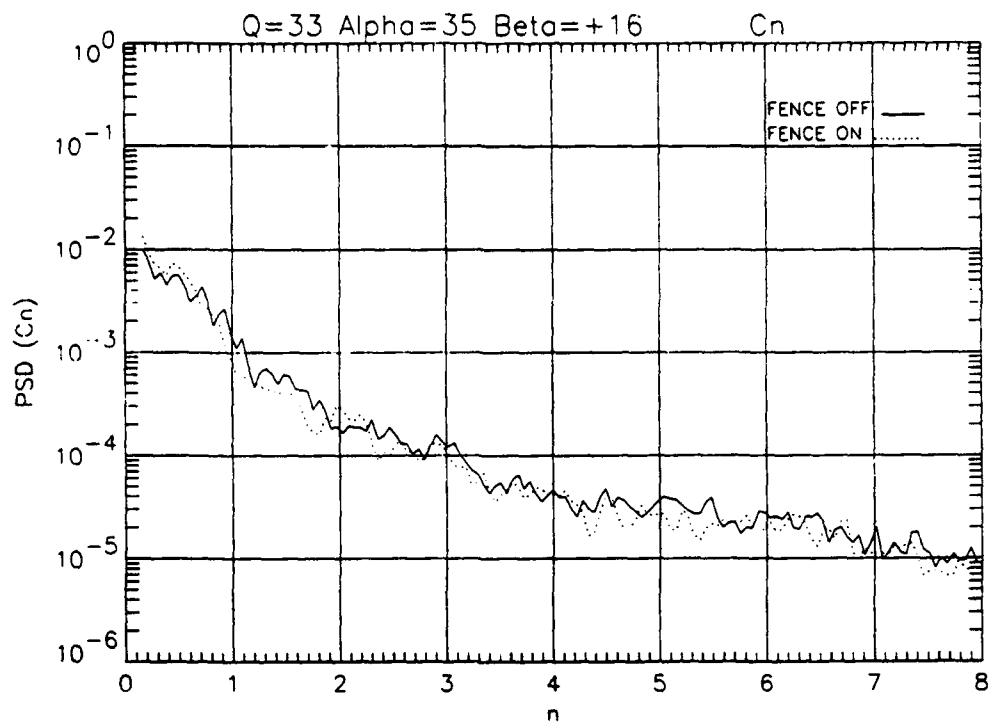


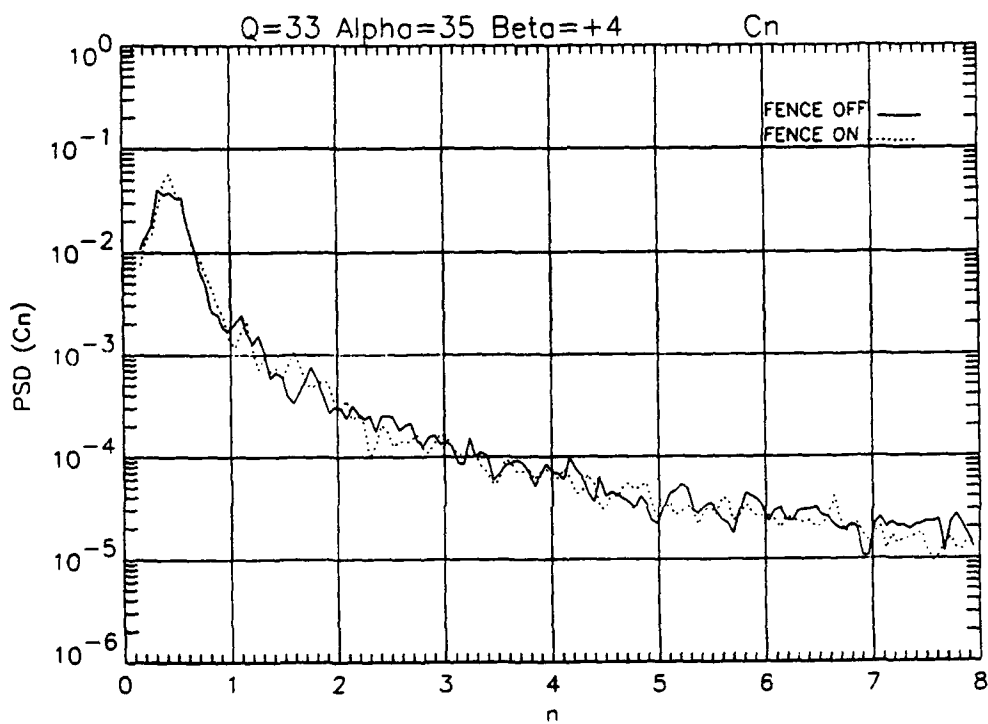
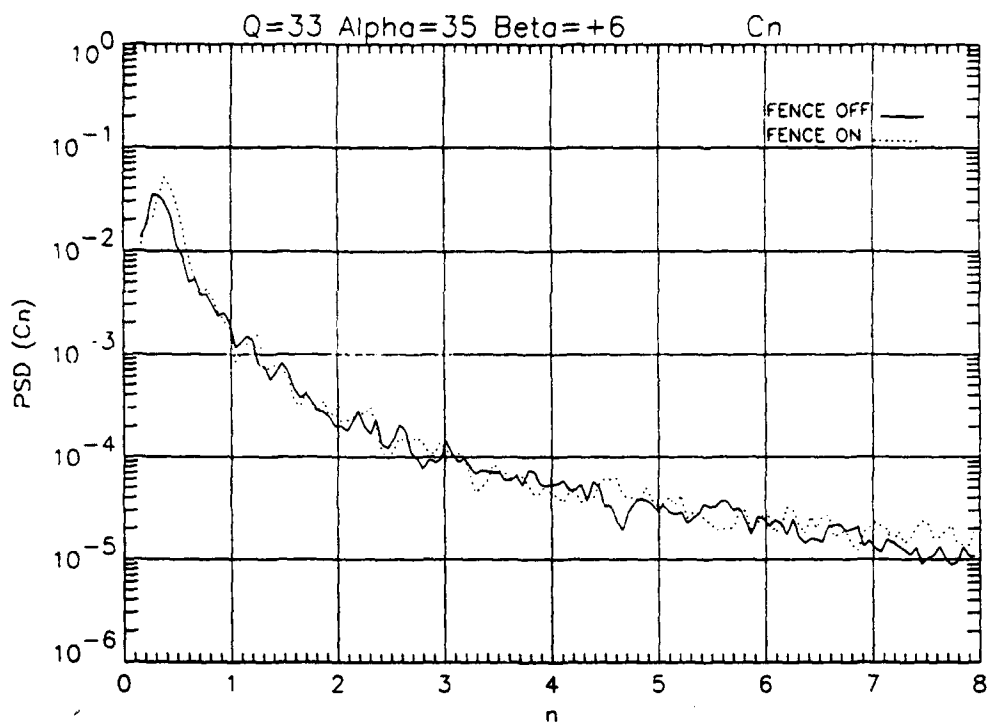


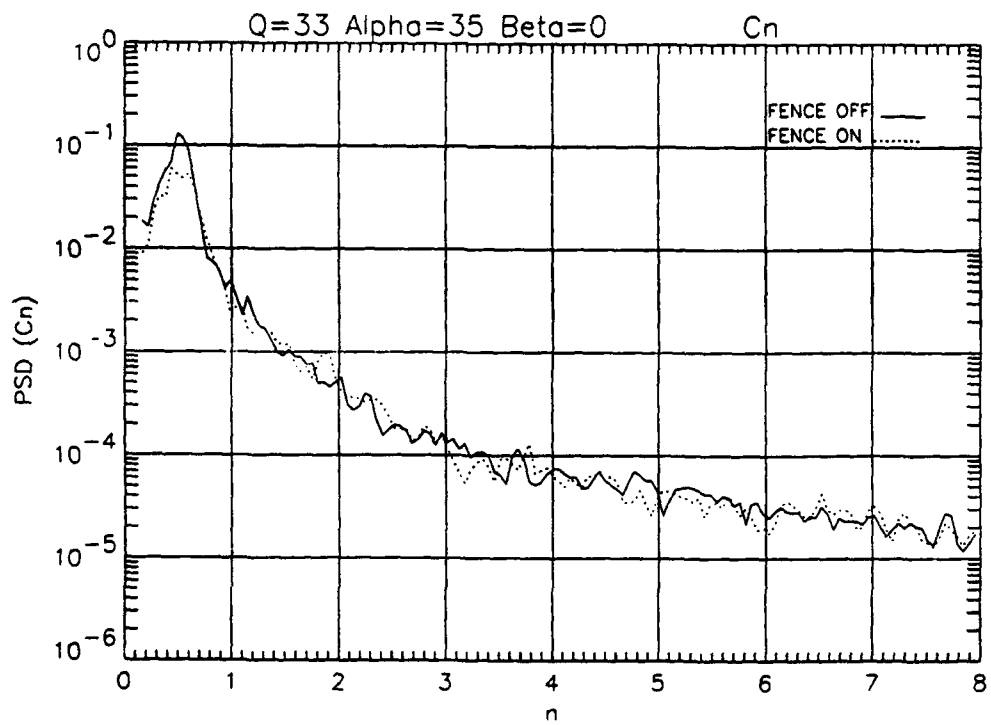
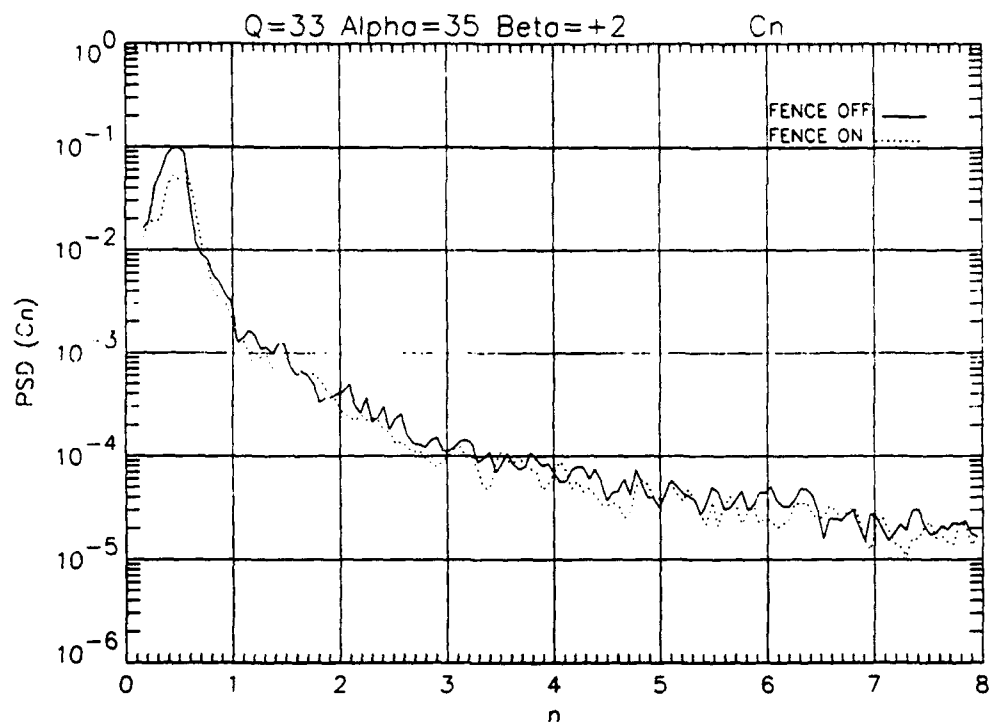


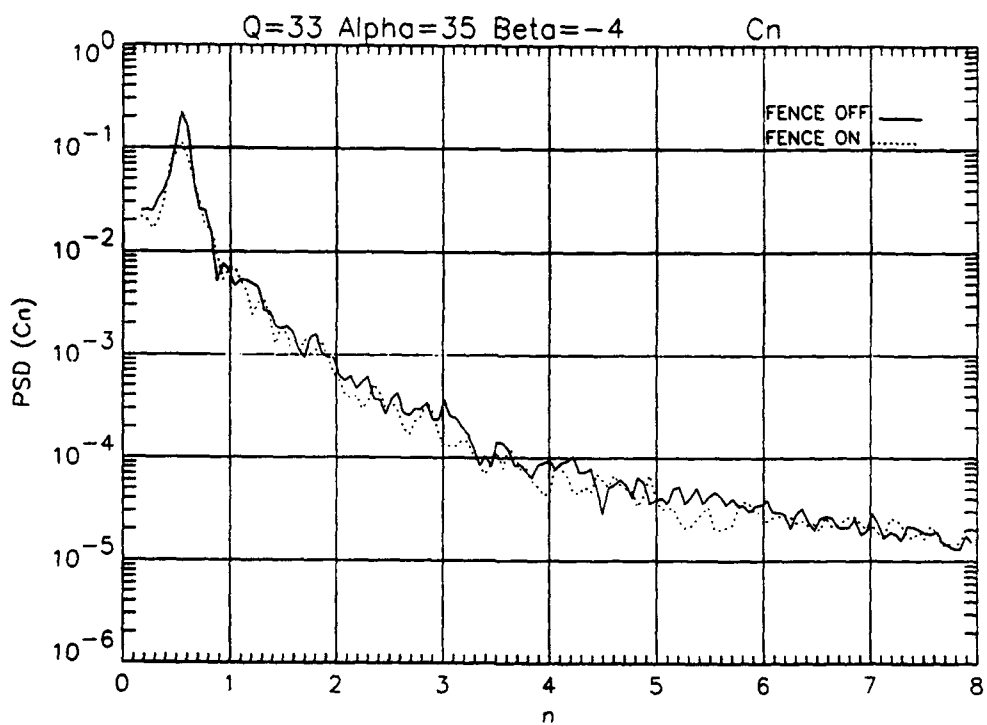
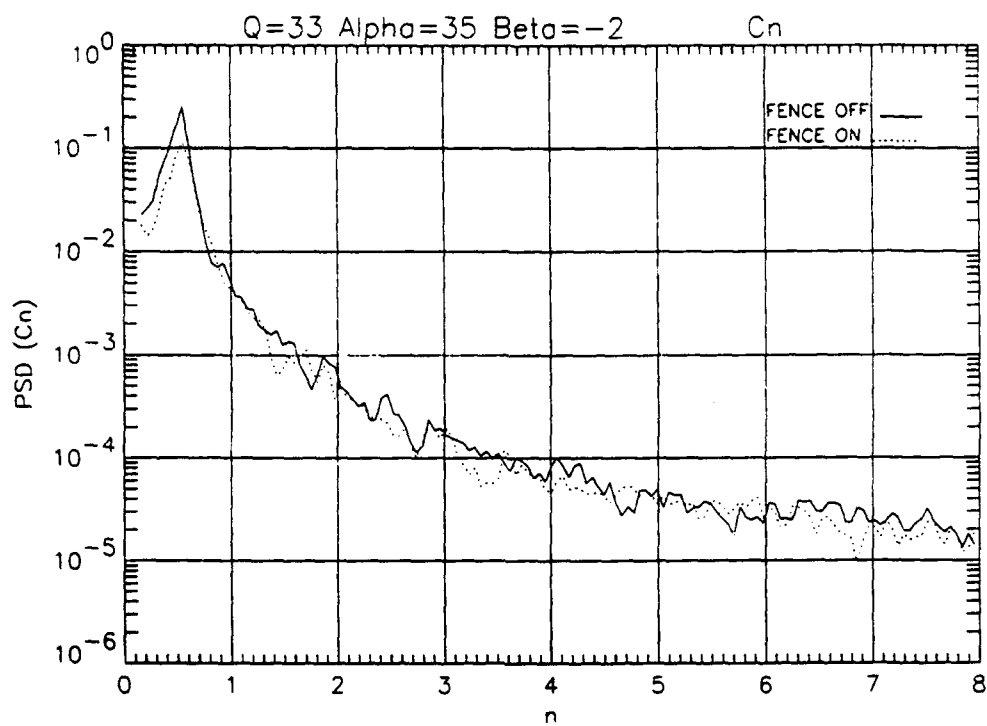


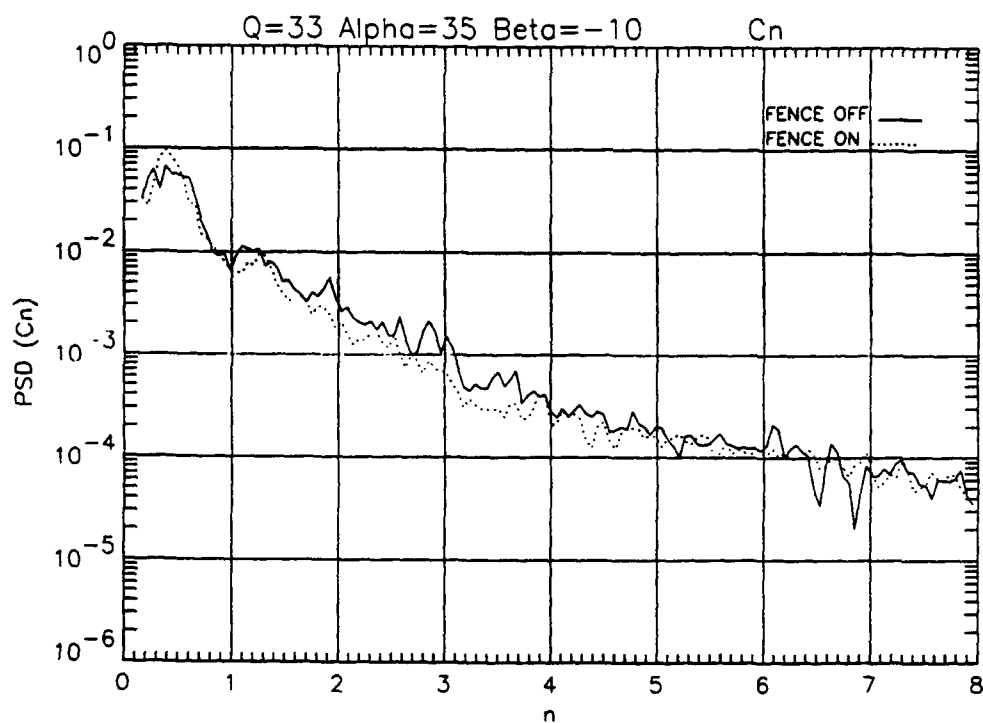
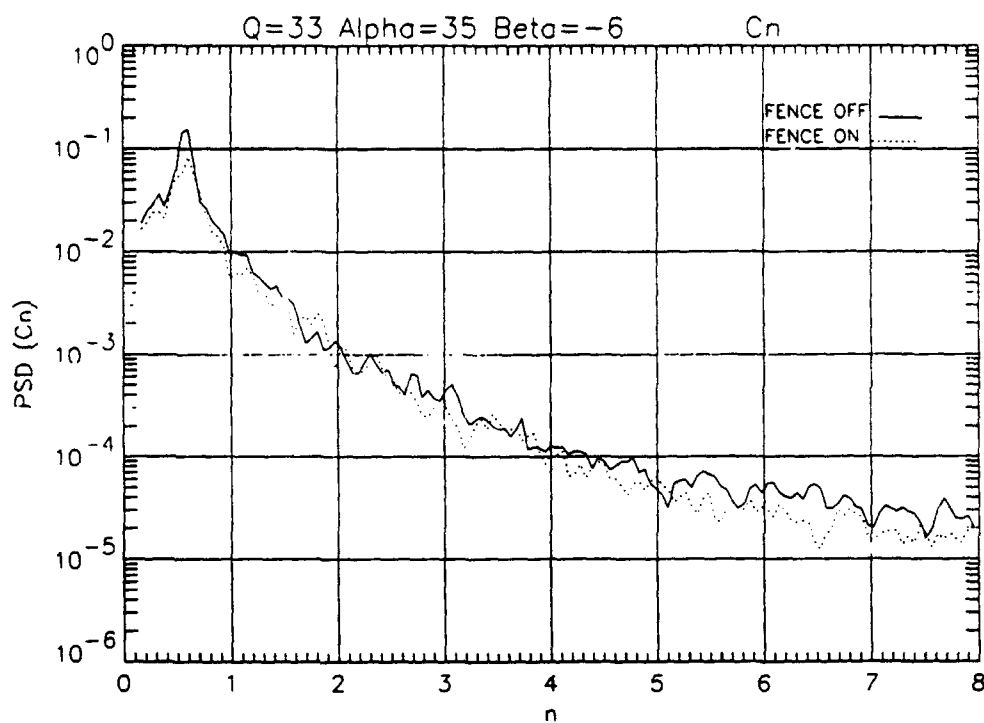


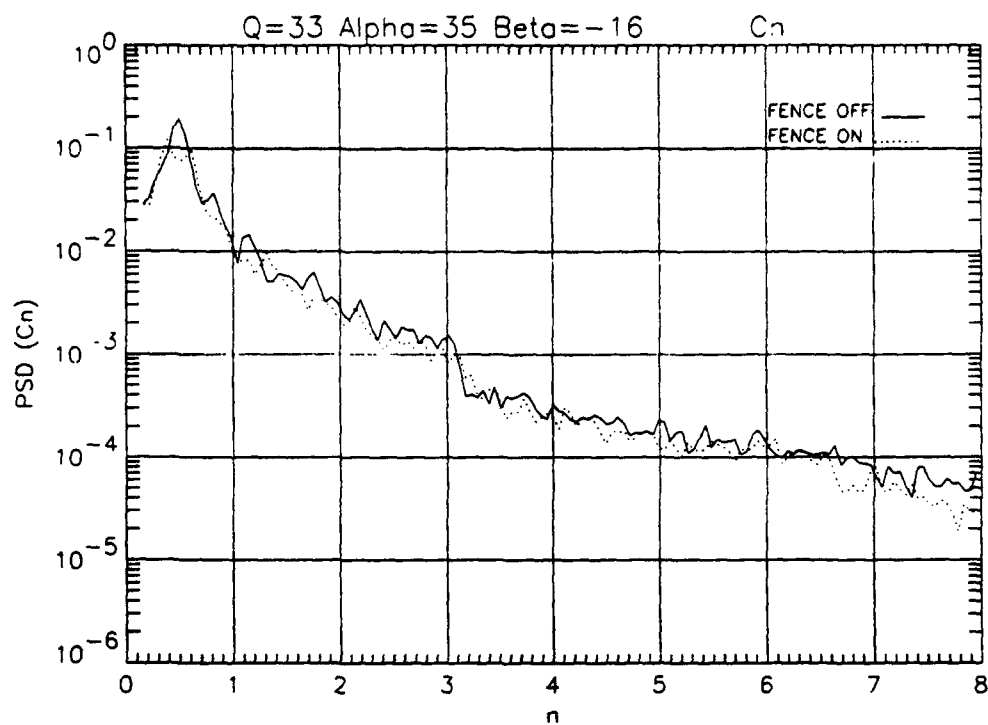












Appendix II

A Note Regarding Interpretation of Fin-Tip Accelerations Using Model Scaling Criteria

An important, elementary model scaling issue should be reviewed with regard to the discussion of the accelerations measured in the wind tunnel. Test conditions in the tunnel should, ideally, be chosen so that the scaled dynamic pressure simulates the true dynamic pressure at the required flight conditions. As noted by Ferman, et al. (1990), this requirement is based on the need to scale the buffet pressure PSDs to the flight conditions being simulated in the tunnel. Thus, if a model is scaled aeroelastically, then the flow conditions in the tunnel need to be selected such that the frequency content of the resulting buffet spectrum is a scaled equivalent of that in actual flight.

Wind tunnel tests of a full-scale model such as the current test article present a unique twist on this concept. Aeroelastic models are designed to be tested in a specific tunnel and are designed so that the proper length, mass, and time or frequency scales are satisfied. If the present F/A-18 model is assumed the structural equivalent of a flight-ready F/A-18, then the only remaining controllable parameter is the tunnel freestream dynamic pressure. Since the 80-by-120 Ft. Wind Tunnel at NASA Ames is limited in dynamic pressure to approximately 33 psf and maximum tail buffeting in actual flight is exhibited at dynamic pressures ranging from 300 to 400 psf (Ferman, et al., 1990), the wind tunnel buffet tests were incapable of simulating the extreme buffet pressures experienced in flight.